



**NTNU – Trondheim**  
Norwegian University of  
Science and Technology

# Technical Aspects of Ion Milling and Electron Imaging of Epoxy Embedded Samples for FIB/SEM Tomography

**Marianne Sandvold**

Nanotechnology

Submission date: Januar 2013

Supervisor: Pawel Tadeusz Sikorski, IFY

Norwegian University of Science and Technology  
Department of Physics



# Technical aspects of ion milling and electron imaging of epoxy embedded samples for FIB/SEM tomography

Marianne Sandvold  
Supervisor: Pawel Sikorski

January 25, 2013

## **Abstract**

FIB/SEM tomography is a relatively new imaging technique for 3D investigation of biological tissue. It uses a dualbeam FIB/SEM instrument to alternately image a sample surface with an electron beam and mill off successive slices with an ion beam, collecting a series of images representing the investigated volume. This technique was employed to study alumina nanoparticles, brain tissue and tissue engineered cartilage embedded in epoxy. Hydrocarbon deposition of contamination layers as well as suboptimal sample geometry, were shown to be issues for imaging experiments. It was important to ensure that sample blocks were cut smoothly, and that the material of interest was concentrated at an edge. The alumina nanoparticle sample was used as a model specimen to investigate the volume of origin of signals detected for image formation at different acceleration voltages. This was shown to have a reasonable correspondance with Monte Carlo simulation results. Imaging and Slice and View experiments on the biological samples showed that FIB/SEM tomography can resolve structures below 10nm in size, and that detailed 3D models from properly stained tissue are obtainable. In summary FIB/SEM tomography constitutes a valuable 3D imaging technique for biological samples.

## Preface

I would like to thank Professor Pawel Sikorski for helpful guidance throughout a whole year, and for introducing me to valuable collaborators. I am grateful for having had the possibility to work at NTNU Nanolab at a fascinating instrument for so many hours. I would also like to thank Menno Witter, Jørgen Sugar and Bruno Monterotti for a very interesting cooperation, rewarding discussions, lab tours and general encouragement by showing interest in my work. I would like to thank Magnus Østgård Olderøy for providing interesting samples and contributing with the biological interpretation of my results. Finally I would like to thank Kai Muller Beckwith for general support throughout a period of hard work.

# Contents

<b>1</b>	<b>Introduction</b>	<b>5</b>
<b>2</b>	<b>Background</b>	<b>7</b>
2.1	Other volume rendering techniques . . . . .	7
2.2	FIB/SEM tomography . . . . .	10
<b>3</b>	<b>Theory</b>	<b>13</b>
3.1	SEM theory . . . . .	13
3.1.1	About the instrument . . . . .	13
3.1.2	Signal production . . . . .	16
3.1.3	Electron beam induced deposition of hydrocarbons . . . . .	19
3.1.4	Monte Carlo simulations . . . . .	21
3.2	FIB theory . . . . .	21
3.2.1	About the instrument . . . . .	23
3.2.2	Ion-sample interactions . . . . .	24
3.3	The DualBeam FIB/SEM . . . . .	26
3.3.1	About the instrument . . . . .	26
3.3.2	Slice and View . . . . .	29
3.4	Sample fixation and staining for biological materials . . . . .	30
<b>4</b>	<b>Materials and methods</b>	<b>36</b>
4.1	Instrument and software specifications . . . . .	36
4.2	Samples . . . . .	36
4.3	Experiments . . . . .	39
4.3.1	General procedures before imaging and S&V experiments . . . . .	39
4.3.2	Interaction volume-investigations on model specimen . . . . .	39
4.3.3	MC simulations . . . . .	40
4.3.4	Imaging . . . . .	40
4.3.5	S&V experiment on artificial cartilage . . . . .	41
4.3.6	Data processing and 3D rendering . . . . .	42
<b>5</b>	<b>Results</b>	<b>44</b>
5.1	Acceleration voltage-dependent interaction volume . . . . .	44
5.2	Imaging . . . . .	47
5.2.1	Hydrocarbon deposition . . . . .	48
5.2.2	Immersion mode vs. regular mode . . . . .	48
5.2.3	Bouton search in brain samples . . . . .	50
5.3	Sample requirements for FIB/SEM tomography . . . . .	52
5.3.1	Abundance of interesting material . . . . .	52
5.3.2	Sample geometry . . . . .	52
5.3.3	Fixation and staining . . . . .	55
5.4	Resolution . . . . .	58

5.5 S&V results . . . . .	62
<b>6 Discussion</b>	<b>65</b>
<b>7 Conclusion</b>	<b>75</b>

# 1 Introduction

Beginning with the first optical microscope created by Robert Hooke in 1665 [1], microscopy techniques have continuously been developed towards ever higher resolving power to enable investigations of life at a microscopic level. However, already over a hundred years ago the ultimate limit to the resolution of a light microscope imposed by the wave nature of light was discovered [2]. Although modern developments within light microscopy have sought to overcome this limit, the real revolution came with the advent of the electron microscope around 1940 [3]. Electrons also have a wave nature, but their wavelength is so small that the resolution in electron microscopy is not limited by diffraction. The transmission electron microscope (TEM) has allowed biologists to discover tissue organization at nanometer scale, but researchers also understood the possibility of false interpretations from mere 2D image observation. To fully appreciate the three dimensional organization of biological matter, the search towards 3D imaging techniques began in the 1950's [4]. Some of these techniques will be described in the background section of this report. FIB/SEM tomography is a modern development based on the alternate use of an electron beam for imaging and an ion beam for milling off consecutive slices of material, to collect a stack of images representing the initial sample volume. The technique became available with the introduction of dualbeam FIB/SEM instruments around year 2000<sup>1</sup>, and offers exciting possibilities. Micrometer volumes can be visualized at nanometer resolution, and the interplay between various tissue components can be fully appreciated.

In order to understand the possibilities enabled by such an instrument, it is important to be familiar with the functionality behind both of these instruments. This report therefore includes a thorough theory section describing the basics of the SEM and the FIB separately. The theory behind signal production mechanisms of SEM imaging signals will be explained, as well as the ion-sample interactions leading to applications like milling and material deposition. A description of the DualBeam instrument will then be given, before sample preparation protocols for biological samples will be reviewed. Some parts of the theory is reproduced from previous work done by the candidate [5].

The FIB/SEM instrument is quite unique in its ability to image a surface and later use the ion beam to reveal what is actually behind the imaged surface. This opens up for technical descriptions of the signal produced by the electron beam, considerations that have earlier only been accessible through simulation methods. The experimental part of this work therefore begins with an attempt to compare the depth of signal origin for electron beams of different acceleration voltages. Monte Carlo simulations are carried out to support the interpretation of the experimental findings.

In further experiments, biological samples composed of brain tissue and tissue engineered cartilage embedded in epoxy are investigated. The effect of different fixation and staining procedures on tissue appearance are explored, along with the requirements on sample geometry. Imaging challenges will be discussed, and optimal imaging parameters

---

<sup>1</sup><http://www.fei.com/company/about-fei/company-history.aspx>

for collection of high resolution images are described. Finally the use of FIB/SEM tomography for acquiring high resolution 3D information about a biological sample will be demonstrated.

## 2 Background

There exists a range of techniques that can be used to obtain 3D information about a sample at hand. Some of these are confocal microscopy, serial section TEM, electron tomography and serial block-face SEM. They are based on different microscopy techniques, and have their advantages and disadvantages. In this background section the above-mentioned techniques will be shortly described, before FIB/SEM tomography will be introduced along with some of the state of the art applications that have been performed as of today.

### 2.1 Other volume rendering techniques

#### Confocal microscopy

Confocal Laser Scanning Microscopy (CLSM) was introduced in 1987, and is probably the most routinely used technique for 3D investigation of biological material [6]. It uses a laser beam to illuminate the sample, and image detection is done through a pinhole to exclude out of focus light. The beam (or the sample) is then scanned in a regular pattern in order to collect an image of the whole specimen. By changing the focus plane, different layers of the sample can be imaged, and these images can be reconstructed to yield a representation of the sample in 3D. What is imaged in CLSM are fluorescent molecules. The samples are stained with fluorescent molecules prior to inspection, the laser excites the fluorophores and the fluorescence is observed by collecting the appropriate wavelength interval. Excitation and detection of different fluorophores can be performed in different channels, and allows the user to distinguish between various components in the sample. Fluorescent dyes exist for a number of proteins, nucleic acids, antibodies and so forth, and this specificity of CLSM is a great advantage of the technique. Another advantage is the noninvasiveness, meaning that CLSM observation does not destroy the sample at hand and can even be used for live cell imaging.

The pinhole configuration in a confocal microscope allows it to overcome conventional widefield microscopes in terms of axial resolution. An increase in lateral resolution is also possible by reducing the size of the pinhole, but this would also reduce the intensity of the in-focus light. Confocal microscopes are therefore normally operated in the same lateral resolution range as conventional widefield microscopes when investigating biological tissue [6, 7]. This resolution is limited by light diffraction to about half the wavelength of the used light, a few hundred nanometers. To observe the organization of fine structures in biological material a higher resolution is required, and the use of a transmission electron microscope is an attractive alternative.

#### Serial section transmission electron microscopy (SSTEM)

The transmission electron microscope (TEM) has been used for biological studies since the 50s, with the first successful observation of a cell being done by Porter and colleagues

in 1945 [8]. Ever since the beginning researchers investigated successive slices in order to get an impression of the three dimensional organisation of the tissue at hand [9, 4, 10, 11]. Investigating series of thin-sections is called serial section TEM (SSTEM) and offers unique lateral resolution for slices of thickness down to about 30nm [12]. Today the technique profits from 50 years of development within sample preparation, in particular good preservation during fixation and embedding and excellent contrast thanks to staining performed on thin sections. Knott et. al. and Ostroff and colleagues recently published neurological studies performed by investigating 600-1000 slices of 60nm thickness and 100 slices of 46nm thickness respectively, with the TEM [13, 14]. The most substantial SSTEM work was performed by White et. al., who reconstructed the whole nervous system of the worm *C. elegans* based on 8000 images from 50nm thin sections [15]. However this required a tremendous amount of manual labour, which is the reason why SSTEM has not been in wide use. Each slice must be cut and investigated separately and in correct order. In addition mechanical slicing can induce artifacts in the sample, and the images must be aligned after imaging.

### **Electron microscopic tomography (ET)**

Electron microscopic tomography uses a TEM for inspection of relatively thin slices, but images the specimen at different tilt angles obtaining a series of images that can be interpreted to yield 3D information of the sample at hand. The principle is shown in Figure 1. The images are not a series of flat 2D images as in SSTEM and this makes the 3D rendering more complicated, but several algorithms (with real space or Fourier space calculations) have been developed and optimized for different kinds of samples. For ET to result in a complete 3D representation of the investigated sample, it must be observed over a tilt range of 180 degrees at sufficiently small degree intervals. The size of the interval depends on the desired resolution  $d$  as expression in Equation 1 [16].

$$N = \frac{\pi D}{d} \quad (1)$$

where  $D$  is the diameter of the object to be observed and  $N$  is the minimum number of equispaced projections needed to obtain the desired resolution  $d$ . As an example 79 projections (one each 2.28 degrees) would be needed to reconstruct an object of 100nm in diameter at a resolution of 4nm. In the beginning such experiments were performed manually and naturally required a lot of manual labor for accurate rotation, focusing and shift correction during imaging. In addition the specimen was exposed to a very high dose of electrons risking deformation of the original structures in the sample. Now there are instruments that perform all image collection automatically once the sample has been placed properly within the sample chamber, and automatic focusing and drift correction is done at lower magnification thus reducing the electron dose [18]. This low-dose operation allows for investigation of unstained biological material embedded in vitreous ice, ensuring that the observed structures originate from the specimen itself and not from staining

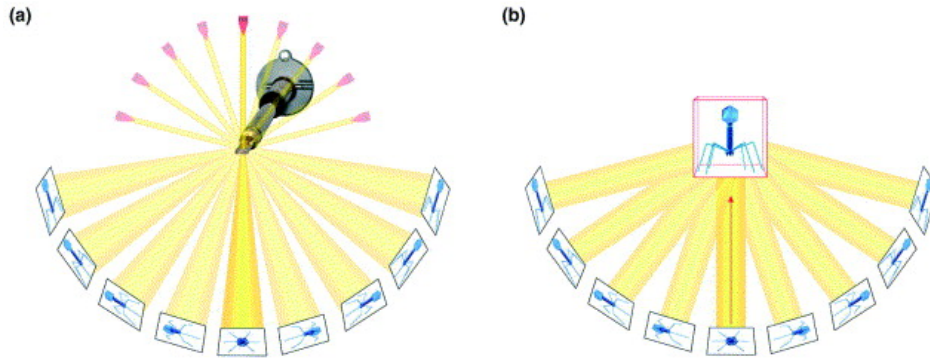


**Figure 1:** Schematic showing the principle behind electron tomography (ET). In this case a bacteriophage is contained in the thin sectioned sample, and imaging from several directions allows to reconstruct the bacteriophage in 3D. Figure from reference [17]

chemicals. However there are still instrumental limitations, in particular the available sample tilt which is usually limited to  $\pm 60^\circ$ , and the incremental rotational change that can be done accurately. Electron dose can still pose a problem, and conflicts with the requirement of a large number of projections for the best possible resolution.

An electron has a limited mean free path when passing through a solid, meaning that it will undergo several collisions within the sample if its thickness is too large. The occurrence of several scattering events upon transmission through the sample obscures the image resolution, and therefore the thickness of the specimens investigated with ET must be limited. The best theoretical resolution for a specimen of 400nm observed with electrons at 300kV is 5nm [12].

In summary, ET is very good for the study of organelles or molecular structures, but has limited application for the study of larger volumes. One possible way to meet this challenge is to investigate serial sections of plastic embedded samples with ET, similarly as with SSTEM [19]. This is still challenging however, since consecutive sections need to be taken in and out of the microscope. The region of interest must then be found and refocusing and realignment must be performed. It would be substantially easier if the sample to be investigated could stay inside the microscope during the whole experiment. This is rendered possible by serial block-face SEM.

### Serial block-face scanning electron microscopy (SBFSEM)

Serial block-face SEM (SBFSEM) was successfully introduced in 2004 by Denk and Horstmann [20], around the same time as the first FIB/SEM S&V experiments were done by Drobne et. al. on biological samples [21, 22, 23]. In SBFSEM a face from a block of embedded material is imaged in a SEM, before a thin slice of material is removed by a microtome mounted inside the sample chamber of the microscope. Cutting and imaging is performed in succession so that a series of images is obtained that can be used to reconstruct the investigated volume in 3D. Artifacts such as slice folding after mechanical cutting that cause trouble in SSTEM are irrelevant since it is the block-face that is imaged

and not the thin sections. Between each cut the stage is moved in z direction so that refocusing during an experiment is unnecessary, thus allowing for automatization of the process. This is a huge improvement and simplification compared to the serial section techniques described above. The knife is mounted horizontally within the sample chamber so that the whole sample can be imaged with the electron beam at normal incidence, allowing a large area to be within the depth of field. Several images can be taken between each cut, rendering this large area accessible. The SBFSEM is now commercially available through Gatan Inc. under the name 3View<sup>TM</sup>., and the minimum slice thickness for routine experiments is around 50nm. The lateral resolution in SBFSEM is somewhat lower than in SSTEM since a SEM is used for imaging instead of a TEM, and the axial resolution can not compare to the axial resolution obtained in serial section ET. FIB/SEM tomography is another technique where the image acquisition can be automated, but where the obtainable axial resolution largely overcomes that of SBFSEM.

## 2.2 FIB/SEM tomography

FIB/SEM tomography is a technique carried out by Slice and View experiments, and the technique will be described in more detail in theory section 3.3.2. The idea behind FIB/SEM tomography is very similar to the principle of SBFSEM. A SEM is used to image the block face of a plastic embedded sample, before an ion beam is used to remove a thin slice of material from the block. This process is repeated until a stack of 2D images is obtained, and since the slice thickness is constant throughout the experiment a 3D model can be reconstructed from the stack. An ion beam can mill slices of thickness down to about 10nm, while the size of a cross section that can be observed is limited to about 100  $\mu\text{m}$ .

FIB/SEM tomography was performed on biological samples for the first time in 2004-2005 [21, 23, 22], but has already been used to investigate a range of different sample materials. Examples are yeast cells and tumor tissue [24], brain tissue [25, 26], endothelial cells [27], blood vessels [28] and viruses in HIV-infected macrophages [29].

A state of the art study in terms of resolution was done by Wei and his colleagues in 2012 [30]. They investigated yeast cells that were freeze-substituted (with  $\text{OsO}_4$ ) and stained with uranyl- and lead acetate before epoxy embedding. This cryo-preservation protocol is quite unique compared to the standard aldehyde fixation protocols that are used by others in the field, and resulted in excellent tissue contrast in FIB/SEM. The researchers were able to collect image stacks with cubic voxel size of  $3 \times 3 \times 3\text{nm}^3$  by conducting a S&V experiment with a slice thickness of only 3nm. Knott et. al. have also recently obtained cubic voxels  $4 \times 4 \times 4\text{nm}^3$  in size, when imaging brain tissue with FIB/SEM tomography. These are pioneering results, as the smallest slice thickness available in FIB/SEM tomography has previously been stated to be 10nm [27, 31, 28]. The usual choice of slice thickness lies between 20 - 50nm [28, 32, 31, 26, 33, 27]. With this high resolution, Wei et. al. reconstructed a whole yeast cell with all its intracellular

components, and representative 3D results are shown in Figure 2. The 3D model created from isotropic voxels show more smooth and realistic shapes than the model based on anisotropic voxels. In order to obtain such high resolution imaging results, Wei and Knott both applied a low acceleration voltage electron beam (typically 1.5kV) together with an in-lens energy-selective backscatter detector (EsB) for backscattered electron (BSE) detection. The energy filtering repels low energy BSEs that have lost energy from scattering events deep in the sample, and thus allows for detection of a BSE signal originating from a thin surface layer of the sample.

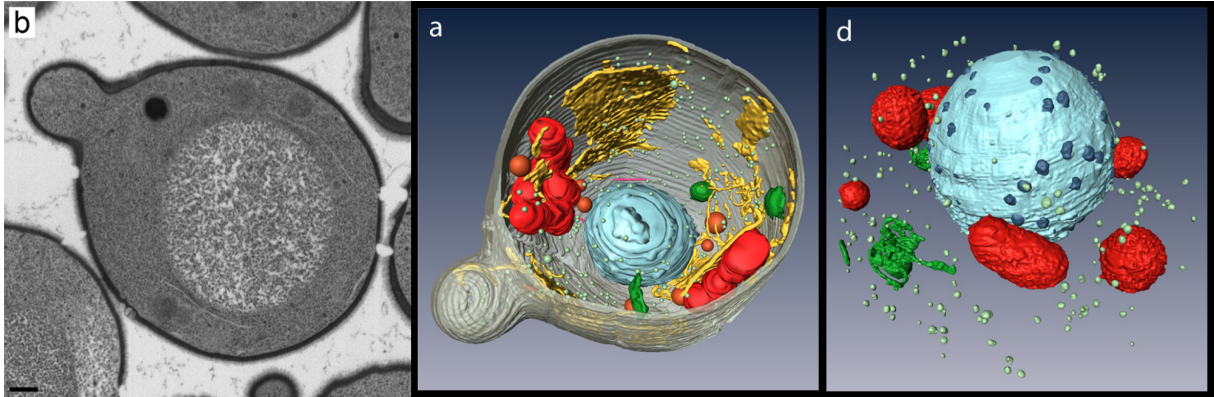


**Figure 2:** One secondary electron micrograph and two images of 3D reconstructions of a yeast cell, from work done by Wei and colleagues [30]. The scale bar on the left micrograph is 500nm, and the cell on the 3D reconstructions measures 3.2  $\mu\text{m}$ . Reconstruction a is based on a stack of images with anisotropic voxels ( $3.27 \times 3.72 \times 15\text{nm}^3$ ), while reconstruction d is based on a stack with isotropic voxels ( $3 \times 3 \times 3\text{nm}^3$ ). The color legends are: grey: cell wall, light blue: nucleus, dark blue: nuclear pores, green: cisternae, yellow: ER, red: mitochondria, pink: microtubules, orange: lipid droplets.

Armer and his colleagues performed an interesting study on developing blood vessels of zebrafish in 2009, combining both confocal microscopy, SBFSEM and FIB/SEM tomography [28]. They conducted live cell imaging in the confocal microscope, along with specific identification of blood vessel fusion points from the presence of fluorescent proteins. To learn more about the structure of the surrounding tissue that was not stained with fluorescent proteins, they located a region of interest (ROI) in the confocal microscope before plastic embedding the tissue and preparing it for FIB/SEM investigation. The ROI was found based on previous measurements, and SEM images were collected from a volume by FIB/SEM tomography. For larger blood vessels in a later stage of development, the volume of interest was too large to analyze with FIB/SEM tomography. The researchers therefore used SBFSEM as an alternative, a technique that can access larger volumes and spends less time cutting successive slices. This at the expense of a reduced axial resolution. This study nicely demonstrates the benefits from combining the use of various 3D imaging techniques to profit from the different advantages they possess. FIB/SEM tomography along with SBFSEM has the advantage of being automatable, and Wei and Knott have demonstrated that the technique can be pushed to resolutions comparable to

TEM resolution in both lateral and axial direction.

## 3 Theory

A dualbeam FIB/SEM is composed of both a FIB and SEM put together in a single instrument. In order to understand the functionality and possibilities of such an instrument it is important to know the theory behind SEM and FIB separately. This section will therefore explore SEM and FIB theory, before explaining the setup of a dualbeam instrument. Different methods used to prepare biological tissue for FIB/SEM investigation will then be described.

### 3.1 SEM theory

The idea behind a scanning electron microscope is to create a large number of electrons from a source, accelerate them and focus them into a precise beam that hits only a small spot of the sample at a time. When the beam hits the sample, signals (like secondary electrons (SEs), backscattered electrons (BSEs) and characteristic X-rays) are created that can be detected by a suitable detector. The beam is scanned over the sample surface following a raster scanning pattern. When the software knows the pattern the beam follows and the time it spends on each spot (called dwell time), it can correlate the signals from the detector to areas of the sample and hence create an image representation of the whole sample surface.

#### 3.1.1 About the instrument

This section will examine the electron source and the lenses used to focus the electron beam.

The electron source in the dualbeam FIB/SEM used here is a Cold Field Emission Gun (CFEG). It is composed of a very sharp needle (diameter less than  $1\ \mu\text{m}$  [34]) of tungsten subject to a high electric field. The electric field is created between the tungsten tip, which serves as the cathode, and a pair of anodes placed below the tip [35]. The construction is illustrated in Figure 3. The voltage difference between the tip and the second anode is what is referred to as the acceleration voltage of the beam column [36]. When the electric field makes the electrons at the tip overcome their work function, they will be forced to tunnel out of the surface and leave the tip. Once in vacuum, the electrons are further accelerated away from the source by the same strong electric field. The anodes are shaped as circular apertures, blocking electrons that have velocity vectors in another direction than the direction of the beam.

Once the electrons have been emitted by the electron gun, they enter a beam column with a series of lenses and apertures. A schematic representation of a SEM column is shown in Figure 4. The goal is to achieve a nicely focused beam with a small beam diameter and a small energy spread but with a satisfactory current density.

The lenses in a SEM column are magnetic lenses, meaning they set up a magnetic field used to focus the energetic electrons. There is no net work exerted on an electron in

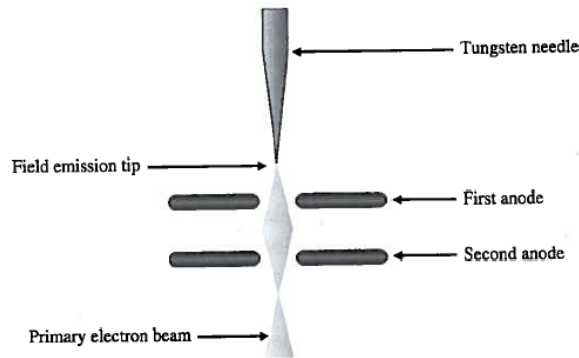


**Figure 3:** Illustration of the setup of a cold field emission gun (CFEG). A sharp tungsten needle is subject to a strong electric field set up by a pair of anodes. The source is operated at room temperature so it is only the strong electric field present at the sharp tip that makes electrons escape from it. Figure from reference [35]

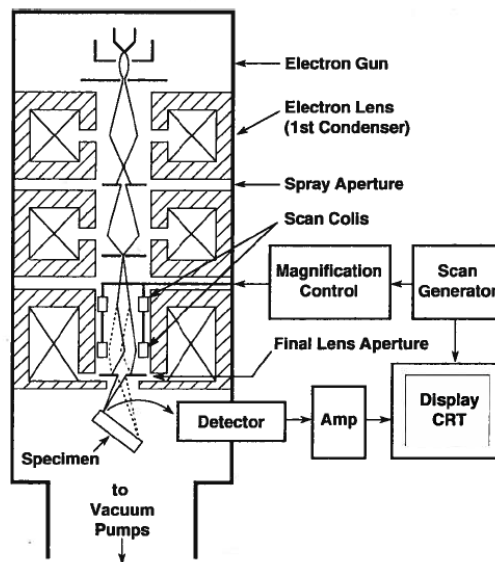


**Figure 4:** Schematic representation of a SEM column and its components. The electron source is a cold field emission gun, several magnetic lenses focus the electron beam and apertures limit aberrations and control the final electron current arriving at the sample surface. In the final lens there are scanning coils and a stigmator (not shown) that corrects for beam astigmatism. Figure from reference [36]

a magnetic field, so the kinetic energy of the electrons remain unchanged upon passage through a magnetic lens [35]. An electron in a purely magnetic field  $B$ , will experience a force  $F$  expressed by the Lorentz force law:

$$F = q(E + v \times B) \Rightarrow F = -e(v \times B) \quad (2)$$

where  $q$  is the charge of the particle,  $E$  is the electric field and  $v$  is the velocity of the particle.  $-e$  is the charge of an electron., which is the particle considered here.

A particle of charge  $q$  accelerated by a voltage  $\Delta V$  will gain a velocity  $v$  which can be expressed by:

$$v = \sqrt{\frac{2q\Delta V}{m}} \quad (3)$$

where  $m$  is the mass of the particle. Since the force on an electron in a magnetic lens depends on its velocity, and the velocity depends on the initial energy of the electron ( $q\Delta V$ ), it is important to have a narrow energy spread of the initial electron beam to focus well.

The magnetic lenses are usually composed of a cylinder of small copper coils, as shown in Figure 5. The magnetic field is such that the deflection of the beam is proportional to the distance from the central axis of the lens [35], so that ideally all electrons originating from a transverse plane before the lens should be focused to the same spot after the lens. Chromatic aberration, spherical aberration and astigmatism will however make the focusing diverge from the ideal case. The magnetic lens is thus analogous in function to a glass lens in a light microscope, with a certain focal length and aberrations. An important difference is that the focal length of a magnetic lens can be controlled by changing the current in the coils composing it.

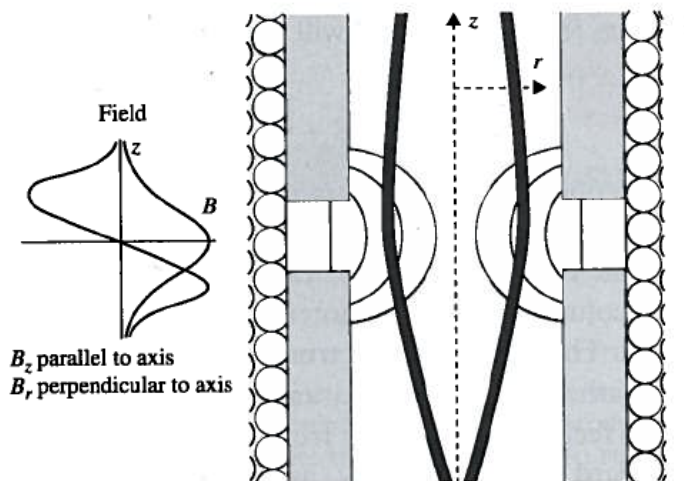


**Figure 5:** Cross section of a cylindrical magnetic lens used to focus the electron beam in a SEM, reprinted from [35].

Within the last lens in the column (the objective lens), are two pairs of deflection coils. The deflection coils are magnets having fields perpendicular to the long axis of the

column. By changing the current in the coils the electron beam can be deflected in x and y direction. These scanning coils are used to raster scan the electron beam, a central functionality of the scanning electron microscope.

### 3.1.2 Signal production

When a focused beam of accelerated electrons impinges on the surface of a solid sample, several elastic and inelastic scattering events happen between the electrons and the atoms in the sample. Considering that electrons are charged, have spin and a particle wave duality, it is not surprising that the physics behind these scattering events is very complicated, and the reader is referred to [37] for a more thorough description. It will be seen that elastic scattering creates backscattered electrons (BSEs) and that inelastic scattering creates a range of other signals including secondary electrons (SEs) and characteristic X-rays. The various signals created are summarized in Figure 6. These signals are exploited to obtain different kinds of information about the sample at hand, using appropriate detectors. This section will introduce the concept of interaction volume, before focusing on the production of BSEs and different types of SEs.

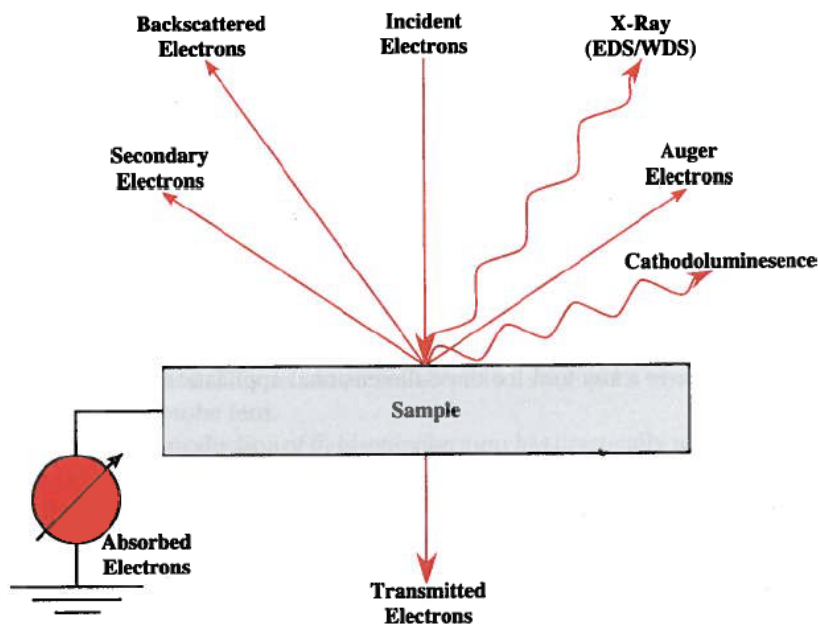


**Figure 6:** Signals resulting from the impact of accelerated electrons with a sample surface. Transmitted electrons are only present for thin specimens such as those investigated in Transmission electron microscopes. Figure from reference [34]

**Interaction Volume** The scattering events that happen between the beam electrons and the atoms in the sample cause the beam electrons to change direction and loose energy. They will follow a randomized path down into the sample, and stop their travel when their energy is reduced to the surrounding energy  $kT$  [34]. The electrons will hence penetrate into a certain volume of the sample, with a depth and a width depending on

the nature of the sample and the energy and angle of the incoming beam. This volume is called the interaction volume of the electron beam.

**BSEs** When electrons hit a sample, the scattering events between electrons and sample happen with a certain probability. This probability is described as an area, a cross section. For elastic scattering at angles higher than a certain angle  $\phi_0$ , the expression for this cross section can be written [36]:

$$Q = 1.62 \times 10^{-20} \left( \frac{Z^2}{E^2} \right) \cot^2 \left( \frac{\phi_0}{2} \right) \quad (4)$$

where  $Z$  is the atomic number of the atoms in the sample and  $E$  is the energy of the incoming electrons. As noted this expression is not correct for all angles, but will be used here for a qualitative description of signals created in a SEM. Elastic scattering can be thought of as a collision between the incoming electrons and the atomic nuclei of the sample [38]. The electrons change direction but lose little energy, and so continue their travel through the sample before they are scattered again. The mean distance travelled between two successive scattering events is called the mean free path of the electron in the solid,  $\lambda$ , and is expressed by [36]:

$$\lambda = \frac{A}{N_0 \rho Q} \quad (5)$$

where  $A$  is the atomic weight of the atoms in the sample in g/mol,  $\rho$  is the sample density in g/cm<sup>3</sup>,  $N_0$  is Avogadro's number and  $Q$  is the elastic scattering cross section described above. Through several scattering events, the electrons can accumulate enough deviation to reexit the sample surface and are then called backscattered electron (BSE). This is illustrated in Figure 7. Backscattered electrons have experienced relatively low energy loss and are one important class of signals that can be detected for SEM imaging. As BSE production is governed by elastic scattering, Equation 4 gives an indication on the kind of information carried by these electrons. The equation shows that the cross section  $Q$  increases with  $Z^2$ , and experimental results confirm that the amount of BSEs created increases monotonically with increasing atomic number. Atomic number contrast is thus the most important contrast obtained from BSE imaging.

The quantity used to describe the relative amount of BSEs created by an electron beam is called the backscatter coefficient,  $\eta$ .  $\eta$  is defined as the number of BSEs ( $n_{BSE}$ ) resulting per number of incoming beam electrons ( $n_B$ ) [36]:

$$\eta = \frac{n_{BSE}}{n_B} \quad (6)$$

At constant beam energy, the backscatter coefficient depends on  $Z$  as shown, but also on the tilt angle  $\theta$  of the sample investigated. The tilt angle can vary between 0 and 90 degrees, corresponding to normal and grazing incidence respectively. Because of the complexity of the physics behind, only empirical formulas exist to describe this dependency, one of wide use being Equation 7 which is valid for energies  $\geq 5$ keV [39, 37].

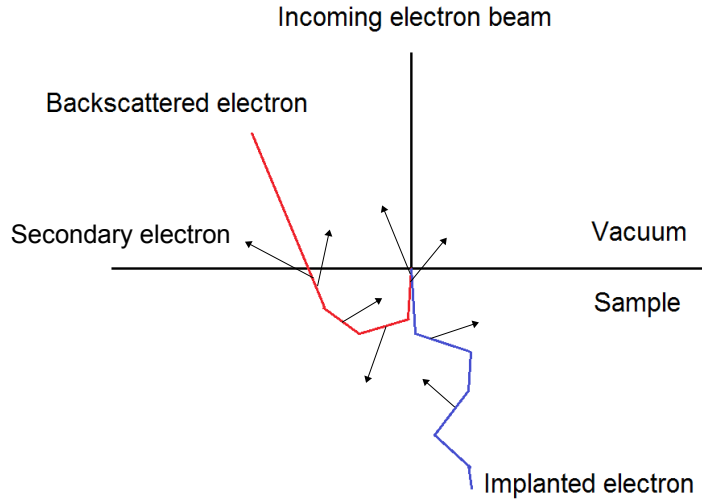


**Figure 7:** A schematic of the fates of the electrons from a focused electron beam. The electrons can either elastically scatter out from the sample and return as backscattered electrons, or lose all their energy through inelastic scattering and become implanted in the sample. All along their paths secondary electrons are created that can escape from the sample if they are created close enough to the surface.

$$\eta = (1 + \cos\theta)^{\frac{-9}{\sqrt{Z}}} \quad (7)$$

Since  $\cos\theta$  goes from 1 to 0 when  $\theta$  goes from 0 to 90,  $\eta$  increases as the tilt angle of the sample increases. This is logic for two reasons: the incoming electrons need to acquire less total deviation to be able to escape back through the sample surface, and elastic scattering has a higher probability of happening at small angles, in the order of 5 degrees [36]. At high tilt angles the primary electrons thus escape as BSEs at a higher frequency compared to at 0 degrees tilt where their most probable path would go somewhere down into the sample.

**SEs** BSEs are primary electrons because they originate from the incoming electron beam, and they result from elastic scattering events. The other type of scattering that can occur when a focused beam of accelerated electrons hits a sample is inelastic scattering. Inelastic scattering occurs between the primary electrons and the electrons of the atoms in the sample [38]. During such a collision the primary electrons lose energy and an atomic electron becomes excited or ejected. Inelastic scattering is thus at the base of all the other signals (except BSEs) shown in Figure 6. If an electron becomes ejected from an outer shell of an atom in the sample, it is called a secondary electron (SE). These ejected electrons usually have an energy between 10-50 eV and are called secondary electrons because they originate from the sample and not from the primary electron beam. SEs are created all along the path of an incoming electron as illustrated in Figure 7, meaning that

secondary electron generation is proportional to the path length travelled by the incoming electrons. Due to their low energy however, SEs can only escape from a region very close to the sample surface (1-20nm) [34]. The depth that SEs can escape from will be called the escape depth in further sections. The escape depth of SEs is larger in insulators than in conductors because the inelastic scattering events leading to their creation mostly happens with conduction electrons [36].

As for BSEs, the amount of SEs produced per incoming beam electron is defined as the secondary electron coefficient,  $\delta$  [36]:

$$\delta = \frac{n_{SE}}{n_B} \quad (8)$$

where  $n_{SE}$  is the number of secondary electrons and  $n_B$  is the number of incoming beam electrons. This coefficient decreases when the energy of the incoming beam increases, which means that more SEs are emitted at low acceleration voltages. Knowing that SE generation is proportional to path length, this can be understood by considering the expression for the mean free path of an electron (Equation 5) together with the cross section for elastic scattering (Equation 4). When the energy of the incoming beam decreases, the cross section for elastic scattering increases and the mean free path gets similarly shorter. This means that at low acceleration voltages the paths of the incoming electrons are for a large part located within a region close enough to the surface for SEs to escape, while at higher acceleration voltages the primary electrons follow paths deeper into the sample from where SEs cannot escape because of their low energy.

Secondary electrons can be created from three sources: the primary electrons from the incoming beam, BSEs or BSEs that collide with the walls of the sample chamber and create SEs upon impact. These three classes of SEs are called  $SE_1$ ,  $SE_2$  and  $SE_3$ , respectively. For a light element the ratio  $\frac{SE_2}{SE_1}$  is small (0.18 for Carbon [36]), meaning that most of the SEs are created by primary electrons. Aluminum is intermediate with a ratio of 0.48, while the ratio increases to values above unity for heavy elements.

As for BSEs, the SE coefficient  $\delta$  changes as the tilt angle of the sample changes. A simple expression of this dependence is found by geometrical considerations, knowing that the SE coefficient is proportional to the distance of an electron travelled within the SE escape depth, as described above. This calculation is shown in Figure 8. In addition to this expression comes the increased contribution of  $SE_2$ , caused by the increase in  $\eta_{BSE}$  with tilt angle.

### 3.1.3 Electron beam induced deposition of hydrocarbons

Hydrocarbon molecules from the vacuum system of the instrument (e.g. vacuum grease and O-ring seals), from fingerprints or from the air are always adsorbed to some extent on a sample surface to be investigated with electron microscopy. The exact amount of adsorbed molecules is difficult to predict, and depends on the total history of the sample including preparation and handling. When a beam of energetic electrons is used to observe

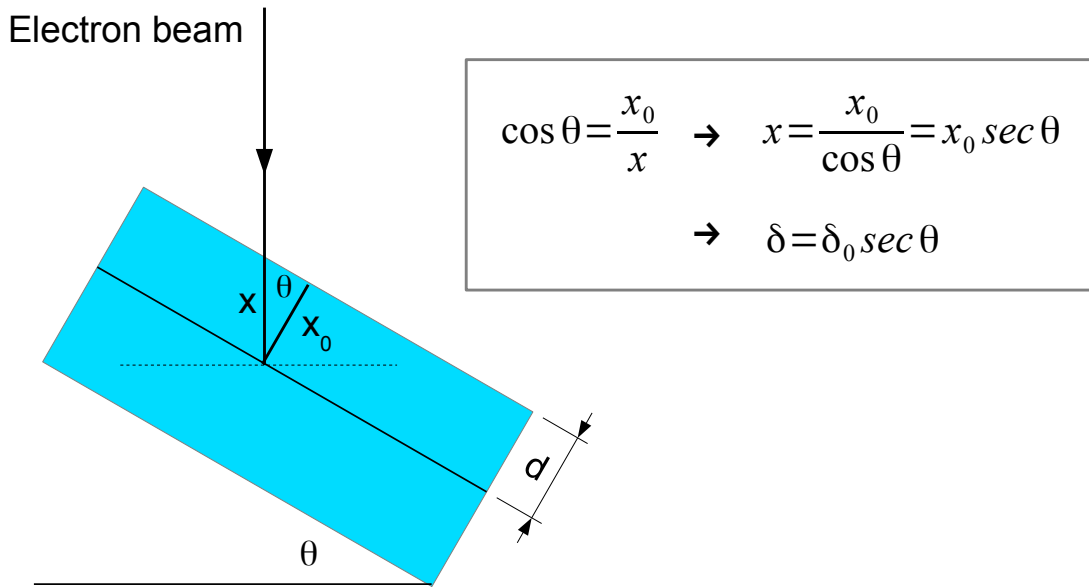


**Figure 8:** Drawing showing the geometric considerations leading to the expression of the SE coefficient  $\delta$  as a function of sample tilt  $\theta$ . The assumption that the SE coefficient is proportional to the distance of an electron travelled within the SE escape depth,  $d$ , is at the basis of this construction.

the surface of a sample, collisions can lead to cross linking of these molecules and hence the deposition of a polymerized carbonaceous layer on top of the observed surface [40]. This contamination layer obscures the electron signal for later imaging, and increases the apparent size of features on a surface that is not flat. At temperatures above 0 degrees, adsorbed hydrocarbon molecules will migrate on the sample surface because of diffusion, and as long as this supply holds up the contamination layer will become increasingly thicker with increased exposure times of the electron beam. This effect has been exploited as a lithography technique for creating nanosized structures [41], but is strictly unwanted when realistic imaging of the sample surface is the goal. Several methods have therefore been proposed in order to limit the deposition of contamination layers during electron microscopy imaging. These include heating or cooling the sample to be investigated, thus either evaporating the adsorbed surface molecules or limiting their diffusion along the surface [40, 42]. A cold trap containing liquid nitrogen (LN2) can also be used, and is standard equipment on most electron microscopes today. All molecules arriving at the cold trap by diffusion will stay there because further diffusion is prevented by the low temperature of the trap. They become trapped and the concentration of hydrocarbon molecules in the rest of the chamber is reduced over time. When it comes to imaging parameters, a lower electron beam current will cause less electrons to impinge on the sample per unit time, and the deposition of contamination layers will be reduced. The higher amount of collisions and SEs created near the surface during low-acceleration voltage imaging causes more contamination to deposit at lower than higher acceleration

voltages.

### 3.1.4 Monte Carlo simulations

It was seen in theory section 3.1.2 above, that the path of electrons in a solid is governed by the series of scattering events they undergo after impinging on the solid sample surface with a certain energy. In order to predict the paths of the electrons from a focused electron beam in a SEM, it would be necessary to be able to predict all these scattering events in detail. Instead of finding an exact answer to a specific situation, Monte Carlo methods aim to give a statistically accurate solution to a problem, here by simulating the path of a large number of electrons based on the use of correct physical models and random numbers [43]. Since all the signals exploited in SEM investigations originate from scattering phenomena, simulating these would also allow to estimate statistics such as the SE and BSE yield, the interaction volume of a beam in a certain material and so forth. Such MC simulations can be explained in a simplified manner by considering the sketch of an electron scattering process, shown in Figure 9. This model assumes that after entering the solid and between each scattering event, the electron travels a certain path length  $S_i$ . Between these paths it is scattered either by elastic or inelastic scattering at a certain angle  $\theta_i$  with a corresponding azimuth angle  $\phi_i$ . If accurate probability distributions (from physical models) exist for these variables, an MC simulation would use these models together with a good random number generator to simulate the stepwise path of many electrons, and hence create a statistically correct outcome of the situation. Important assumptions for this simulation are homogeneity in chemical composition and amorphous crystal structure of the sample [44]. MC simulations give results that can be used to describe and understand physical events, even though the exact solution is not going to be reproduced in an actual physical experiment.

In order to perform MC simulations the free program CASINO (from Monte **C**ARLO **S**Imulation of electro**N** trajectory in s**O**lid) can be used. The program offers a simple user interface to create complex simulations, and is described in detail including the physical models used in [45, 46, 47]. It is worth noting that the model used in CASINO for elastic scattering differs from the one described in Equation 4, because Mott cross sections [48] are used instead of Rutherford cross sections [49].

## 3.2 FIB theory

The Focused Ion Beam (FIB) instrument is in principle very similar to a SEM, only an ion beam is created and scanned over a sample surface instead of an electron beam. The design principles of the source and the lenses are different due to the physical differences of electrons and ions, and will be examined in the following. A drawing showing the most important elements of a FIB column is shown in Figure 10.

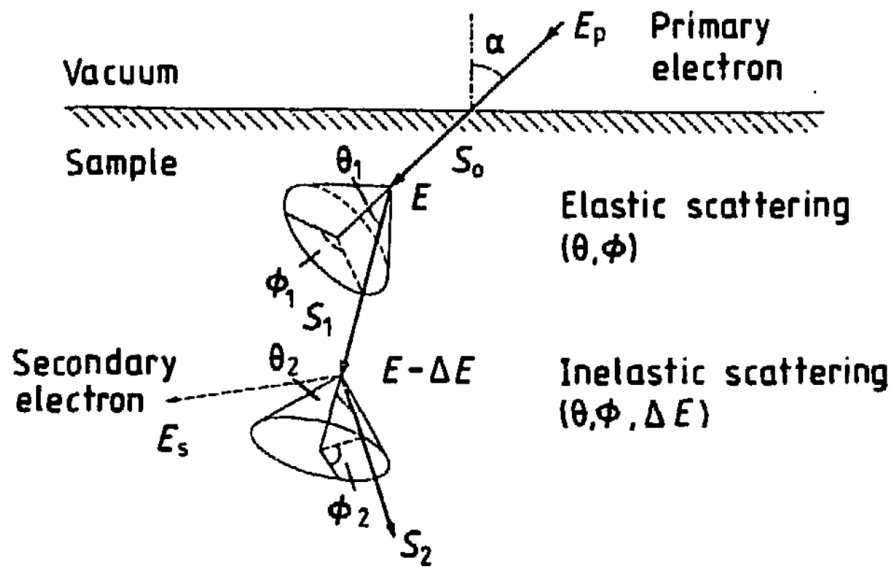


**Figure 9:** A schematic of the scattering events following the entrance of an electron into a solid, taken from [44].

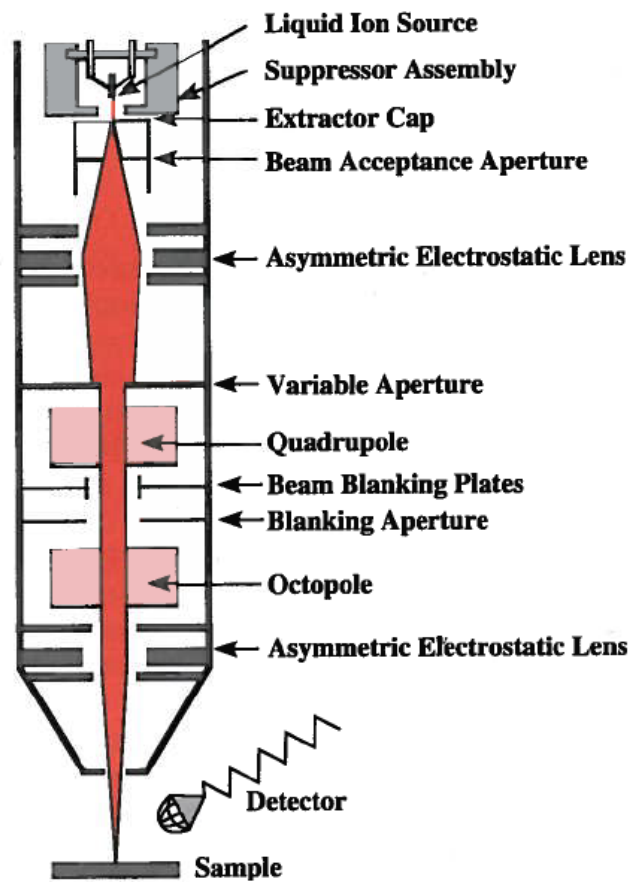


**Figure 10:** Drawing from reference [34], showing the main elements in a FIB column.

### 3.2.1 About the instrument

The ion source in the dualbeam FIB/SEM used here is a liquid metal ion source (LMIS). The typical set-up of a LMIS is shown in Figure 11. It is composed of a heat resistant tungsten needle beneath a gallium metal reservoir. The gallium reservoir is heated to near evaporation with a coil heater [50, 35], which makes it flow and wet the tungsten needle. The tip of the tungsten needle has a diameter of 4-10  $\mu\text{m}$  [35] which gives a much better emission current than a sharper tip [51]. Just below the tip is an extraction electrode with a negative voltage, which draws the gallium molecules into an even sharper tip in the shape of a Taylor cone. The apex of the liquid gallium cone is only about 5nm in diameter, and the electric field at that point becomes strong enough to make gallium atoms undergo field evaporation (through which they become ionized) and escape from the ion source. These ions are then accelerated further down the column. The complex physics behind this emission process is reviewed elsewhere, see for example [51, 50]. The suppressor electrode shown in Figure 11 is there to help the extractor maintain a constant beam current, without the need of changing the voltage on the extraction electrode. Changing the voltage on the extraction electrode would also change the shape of the liquid gallium Taylor cone, causing an unwanted drift of the beam.

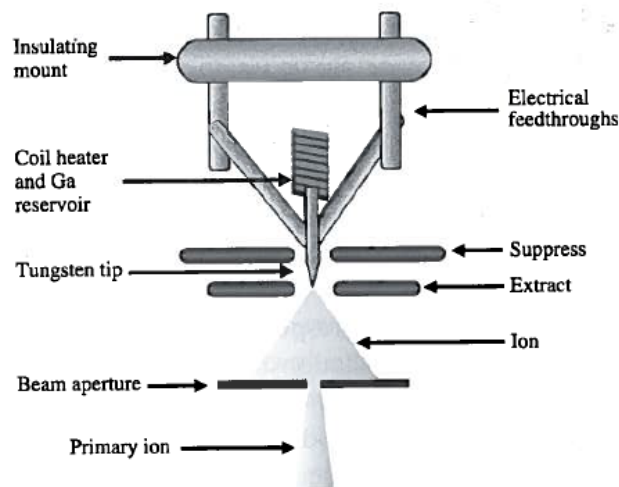


**Figure 11:** A schematic from reference [35], showing the typical set-up of a liquid metal ion source.

While the emission current at the source is kept constant during operation, the effective current arriving at the sample surface can be altered by changing the opening of a variable aperture placed about halfway down the column, as shown in Figure 10. The variable aperture can usually not be changed to an arbitrary size, but has instead a certain number of predefined size choices giving certain currents at the sample surface which are known to the user. In the FEI Helios Nanolab DualBeam the choices of currents range from 1.5pA to 20nA.

The lenses in a FIB column are electrostatic lenses. The reason why magnetic lenses cannot be used comes from Equation 3 and the expression for the Lorentz force exerted on

a charged particle in a magnetic field. The velocity of an accelerated particle is inversely proportional to the square root of its mass. An ion typically has a mass five orders of magnitude higher than an electron, from which follows that its velocity is typically 350 times lower than that of an electron accelerated at the same acceleration voltage. Since the force exerted on a charged particle in a magnetic field is proportional to its velocity (Equation 2), the magnetic field would need to be impractically strong for the lens to have enough focusing power to focus the ion beam. Therefore electrostatic lenses setting up electric fields are used instead of magnetic lenses. The force experienced by a positively charged ion (bearing a single charge) in an electric field is expressed by the Lorentz force law (Equation 2) and becomes:

$$F = eE \quad (9)$$

which is independent of the velocity of the particle. A cross section of a typical electrostatic lens used in FIB instruments is shown in Figure 12. Three electrode cylinders are placed in succession down the column. The cylinders are coupled to different voltages, and between them are gaps giving rise to electric fields which are shown in Figure 12 as dotted lines. The electric fields set up are such that the ions will exit the lens and meet at a point of focus after a certain distance beyond the lens. The ions will be both accelerated and decelerated by the electric fields within the lens, so that their velocity in total remains practically unchanged.

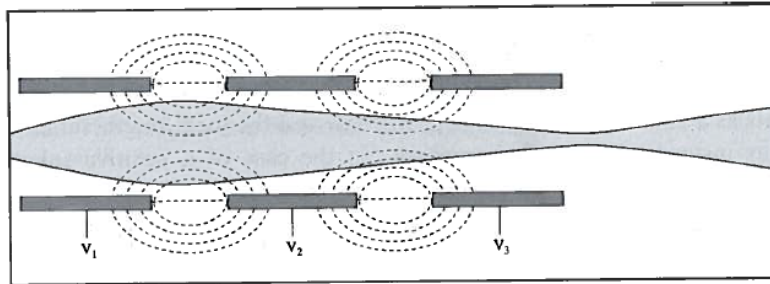


**Figure 12:** A schematic showing the cross section of a cylindrical three-electrode electrostatic lens. Such lenses are used to focus an ion beam in FIB instruments. Figure from reference [35].

The FIB instrument is also a scanning probe instrument. The focused ion beam is raster scanned over the sample surface by the lower octopole lens, shown in Figure 10.

### 3.2.2 Ion-sample interactions

As for electrons, accelerated ions interacting with a sample will undergo a series of elastic and inelastic scattering events. Elastic scattering can cause the emission of secondary electrons, making imaging possible in a FIB, similarly to SE imaging in a SEM as described earlier. Following inelastic scattering atomic defects can be introduced into the sample, atoms can be sputtered away and ions from the incoming beam can become implanted

into the sample. Two of the applications rendered possible by the large mass of ions will be shortly described here, namely milling and deposition.

**Milling** When an ion undergoes nuclear collision with an atom of the sample, the atom can be displaced from its original position and can itself undergo scattering with other atoms in the sample. During this cascade of collision events some of the atoms in the sample will gain enough energy to escape from the sample surface. This effect is called sputtering, and is one of the main effects exploited in FIB applications. Sputtering with an ion beam is also called ion milling. The number of atoms that are sputtered per incident ion is called the sputtering yield. The sputtering yield of an incident ion beam depends on the energy and angle of incidence of the ion beam, and on the composition of the sample it is impinging on. Typical ion trajectories and their dependence on incidence angle and material composition are shown in Figure 13. The corresponding sputtering yield is noted in the bottom right corner. The sputtering yield is an increasing function of the angle of incidence. This can be explained by considering sputtering as a surface effect. The more nuclear collisions taking place near the sample surface, the more atoms will gain sufficient energy to be ejected out from the sample. For the same reason the sputtering yield is an increasing function of atomic number of the atoms in the sample. The higher the atomic number, the higher the rate of nuclear collisions and the higher the sputtering yield. Also to note from Figure 13 is the small size of the interaction volume resulting from a 30kV ion beam, measuring only about 50nm in depth for normal incidence on a silicon target. This is caused by the large mass of an ion, which makes the probability of inelastic scattering much higher for an ion than an electron, and its energy is correspondingly reduced at a higher rate. Thanks to the small interaction volume, milling of a sample can be performed at 30kV allowing for good beam focus and resolution.

**FIB induced deposition of Platinum** Dualbeam FIB/SEM instruments usually contain a gas injection system (GIS) which can be used to introduce an organometallic precursor gas near the surface of the sample. The precursor gas used here for deposition of platinum (Pt) is Methylcyclopentadienyl(trimethyl)platinum(IV),  $C_9H_{16}Pt$  [53]. The precursor gas adsorbs onto the sample surface, and when the ion beam is switched on and focused at this point, the gas molecules decompose into volatile and non-volatile components upon collision with the incoming ions. The volatile components evaporate and are removed from the sample chamber by the vacuum system, while the non-volatile components (Pt in this case) stick to the surface and are thereby deposited. The ion beam current per unit area is a crucial parameter in obtaining good deposition conditions. At low current densities all the gas molecules are not fully exploited, while at high current densities the milling properties of the ion beam become dominant. The ideal current density for Pt deposition in a FIB/SEM lies around 3-7 pA/ $\mu m^2$ , but varies depending of the size of area to be covered as shown in Figure 14 [35]. The gas flow from the injection system is constant, so the density of gas molecules is lower for larger patterns than for

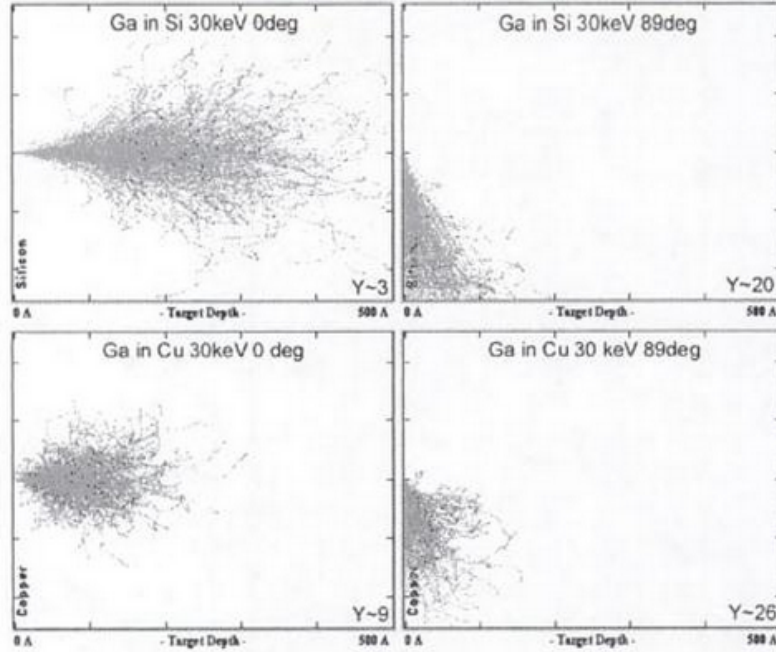


**Figure 13:** Monte Carlo simulations of ion trajectories in silicon and copper at incidence angles of zero degrees and 89 degrees. In the bottom right corner of each figure the sputtering yield  $Y$  is noted. From reference [52].

smaller patterns. For this reason the current density must be low for large patterns ( $3\text{--}4\text{pA}/\mu\text{m}^2$ ) in order to avoid milling, while the current density can be higher for smaller patterns for optimal utilization of the gas molecules. The choice of current for the ion beam is limited by the variations available for the variable aperture present in the beam column, so it might be necessary to adjust the area to be deposited in order to obtain a suitable current density.  $30\text{kV}$  is used as an acceleration voltage for the ion beam, since good focus is important to obtain localized deposition. This technique is exploited in Slice and View experiments, where a layer of Pt is deposited over the region of interest prior to milling of slices to avoid an artifact called curtaining.

### 3.3 The DualBeam FIB/SEM

To put to instruments together in one imposes some requirements on the physical geometry of the instrument. This section will explain how a dualbeam instrument is composed, and describe the detectors used for image collection. The technique behind FIB/SEM tomography will then be reviewed.

#### 3.3.1 About the instrument

In a dualbeam instrument there is both an ion column and an electron column pointed towards a single sample stage, allowing the user to take advantage of all the applications of both SEM and FIB in a single instrument. The electron column is usually positioned

### Focused ion beam systems

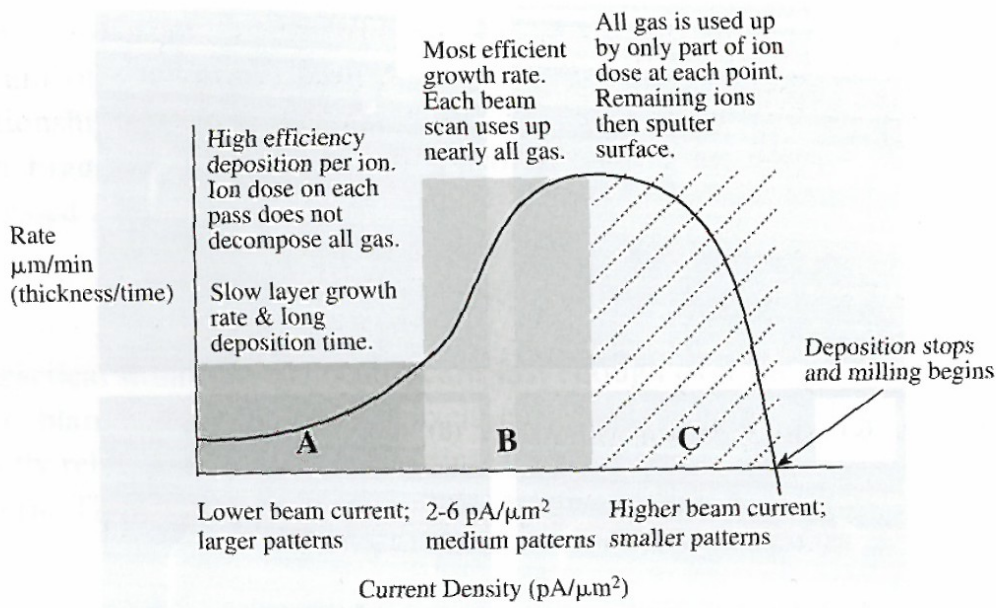


**Figure 14:** Graphic from reference [35], showing how the optimal current density for ion induced deposition of Pt depends on the are of deposition.

vertically above the sample, while the ion column is positioned at an angle ranging from 45 - 52 degrees compared to the electron column [35]. This configuration is shown in Figure 15, where the angle between the columns is 52 degrees. The beam geometry is fixed in a dualbeam instrument.

The sample stage has 5 degrees of freedom: it can be moved independently on x, y and z direction, it can be rotated around the z axis and it can be tilted with respect to the xy plane (corresponding to rotation about the x-axis). Within the sample chamber there is a digital camera through which the movement of the stage can be conveniently monitored. Also integrated in the sample chamber are a certain number of detectors and other additional equipment that varies depending on the demands of the user. It is possible to integrate an EDS detector for X-ray analysis, secondary and backscattered electron detectors, an omniprobe which can be used to manipulate parts of the sample during operation, a gas injection system for FIB induced material deposition and so forth. The sample stage is large, and the Dualbeam FIB/SEM from FEI used here allows for inspection of samples of up to 1.5cm width and 3mm height for the standard sample holder. To have enough space for two particle columns, a range of detectors and gas inlets as well as a large sample stage that can be tilted to angles up to  $60^\circ$ , the sample chamber is correspondingly large

In a dualbeam instrument there is a certain distance below the electron column where the focal points of the electron and the ion beam coincide. This distance is called the

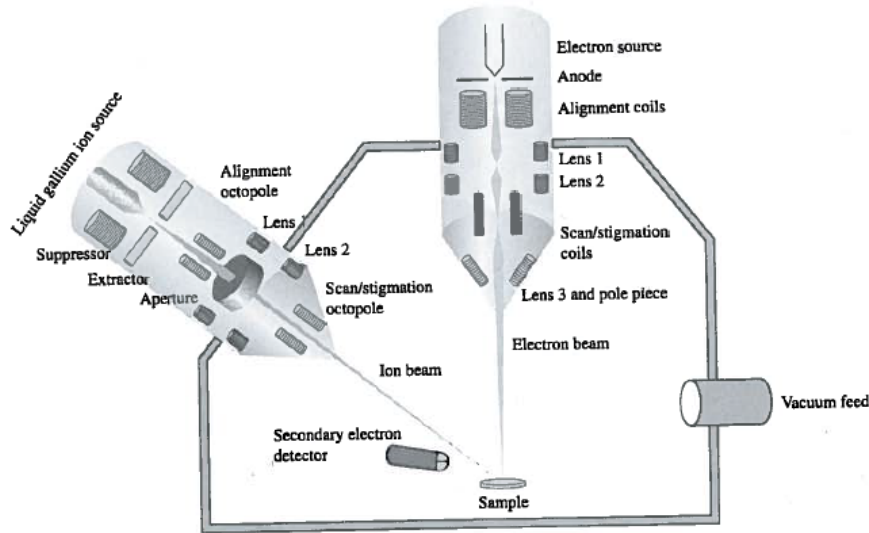


**Figure 15:** Schematic illustration of the main components of a FIB/SEM dualbeam instrument. An electron and an ion beam column are positioned at 52 degrees compared to each other and point to the same sample stage. The sample chamber as well as the columns are under high vacuum, and a number of detectors are included. The sample stage can be moved freely about 5 degrees of freedom. Figure from reference [35].

eucentric height of the sample (and is the same as working distance). If the sample is at eucentric height the electron beam will focus at the same spot even though the sample is tilted. The eucentric height is quite large, 4.1mm in the DualBeam FIB/SEM used here.

There are two detectors in the FIB/SEM applied here that can be used for detection of electrons for imaging, in combination with both the ion beam and the electron beam. These are an Everhart-Thornley detector (ET detector) and a through-lens-detector (TL detector).

The ET detector is well known and used in almost all conventional SEM instruments [36]. It is composed of a copper grid (Faraday cage) which can be positively or negatively biased, a scintillator which transform electrons to photons, and finally a photomultiplier tube (PMT) which transforms photons back to electrons and induces the required signal amplification [54]. The ET detector can be used in two different modes: positively biased at +250V or negatively biased at -50V. At -50V the detector repels the low energy SEs, and collects only BSEs that are emitted from the sample within the solid angle made by the detector and the sample surface at the point of emission. It thus works as a BSE detector at this bias, but the collection is limited because there is no attraction of BSEs that are emitted at an angle not covered by the solid angle of the detector. At +250V, the ET detector is very efficient at collecting low energy SEs (and low energy BSEs, but these are not very abundant). The positive bias attracts electrons that are not emitted within the solid angle of the detector, and the collection is therefore very efficient. At the same time the bias is too low to collect high energy BSEs that are not emitted in the direction of the detector.

The TL detector has the same components as the ET detector and the incoming

signals are actually processed in the same signal tube, but the collector piece is placed inside the final polepiece of the electron column. Under normal imaging conditions this detector does not collect much signal since few electrons will have a path back through the objective lens. Its full potential is reached during imaging in a mode called immersion mode. In immersion mode a magnetic field is set up outside the objective lens, so that electrons emitted at the sample surface will follow this magnetic field, spiral up through the objective lens and get collected by the TL detector. The closer the sample is to the objective lens, the more electrons are emitted within the reach of this magnetic field and the more electrons will get collected by the TL detector. In this configuration it can give very high resolution images and a very good signal to noise ratio. The immersion mode can not be operated in combination with the ion beam.

### 3.3.2 Slice and View

Slice and View (S&V) is a specific application made possible by the construction of dual-beam FIB/SEM instruments. The aim of this technique is to investigate a 3D volume of material with a high lateral and axial resolution. During a S&V experiment, the sample stage is tilted to 52 degrees and the sample is placed at eucentric height so that the focus of the ion and electron beam are coinciding. In this configuration, the ion beam hits the sample edge at grazing incidence, while the electron beam hits the face to be imaged at an angle of 52 degrees. This configuration is shown in Figure 16. At this position, the electron beam is used to take an image of the sample face, before the ion beam is used to accurately mill away a predefined thickness of material. This process of "slicing" with the ion beam and "viewing" with the electron beam is repeated many times, until a desired number of 2D images is obtained. The stack of 2D images can then be reconstructed to represent the initial volume of material in 3D. The slice thickness can be varied between 10 and 200nm, and the lateral resolution is governed by the electron beam which can be set to image at the desired magnification and pixel ratio. In order for the ion beam to mill off a constant thickness at such a small scale, it readjusts according to a fiducial marker (a cross) between each milling sequence. An image of a fiducial marker is shown in Figure 16. In this figure it can also be seen that a layer of platinum (Pt) has been deposited on top of the region to be milled and imaged. The most important function of this Pt-layer is to avoid a common artifact called curtaining. Curtaining is the presence of vertical stripes (thickness variations) on a face that has been milled by an ion beam, and appears because there are variations in the sputtering rate between materials of different composition [55]. There is no perfect theoretical model describing the dependence of sputtering rate on material composition, but the effect has been investigated experimentally as was shown in Figure 13 for example. It has been shown that this artifact can be limited by the deposition of a Pt-layer of thickness around 1  $\mu\text{m}$  prior to milling [56]. The protective metal layer provides a layer of homogenous chemical composition where the ion beam enters the surface to be milled, and the rest of the surface becomes smooth and flat.

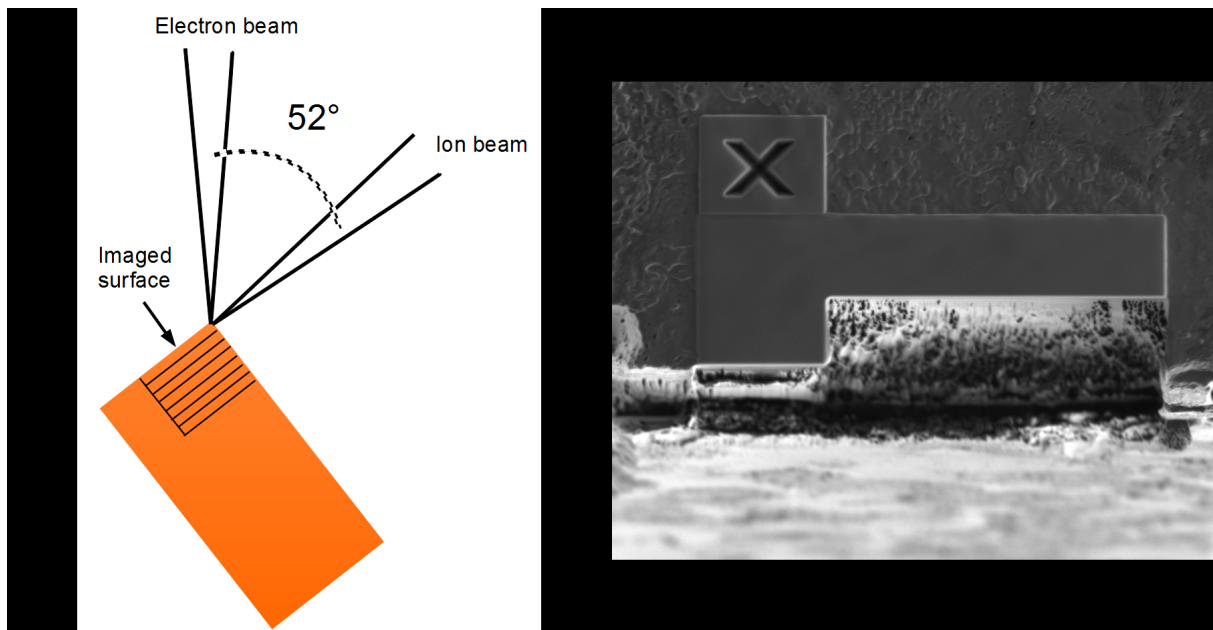


**Figure 16:** Left: Drawing showing the tilt of the sample and the geometry of the two beams when the sample is positioned for a Slice and View experiment. The tilt is at 52 degrees and the height is eucentric. Right: an image taken with the ion beam when the sample is in S&V position as shown to the left. The cross is the fiduciary marker that the ion beam adjusts according to before milling each new slice.

The geometry of the sample is very important for a successful S&V experiment. To avoid the need for excessive milling in order to expose a flat surface of interest, the edge between the surface of interest and the top surface should be 90 degrees. These two surfaces should also be completely flat and smooth. This is important because the focus of the ion beam is adjusted according to the height of the sample, and this height must stay constant throughout a S&V experiment for optimal milling and beam shift between slices. A bumpy surface would make proper platinum deposition difficult, and could make the fiduciary marker distorted so that ion beam shift between slices would become inaccurate, and it could cause curtaining to appear. The material of interest must be positioned at this flat, smooth 90° edge, immediately accessible to the ion and electron beam. The optimal sample geometry is shown in Figure 17.

### 3.4 Sample fixation and staining for biological materials

Electron microscopy is always carried out in vacuum, because the presence of gas molecules would limit the electron mean free path and make proper sample observation impossible. In principle however, vacuum and biological samples are not compatible. Biological material is soft and fragile, and contains water which boils and evaporates under vacuum. Without sample preparation a biological sample would simply collapse when put in the evacuated chamber of an electron microscope. Both fixation and dehydration is therefore a necessity. Fixation is performed with the aim of conserving the original structure of the

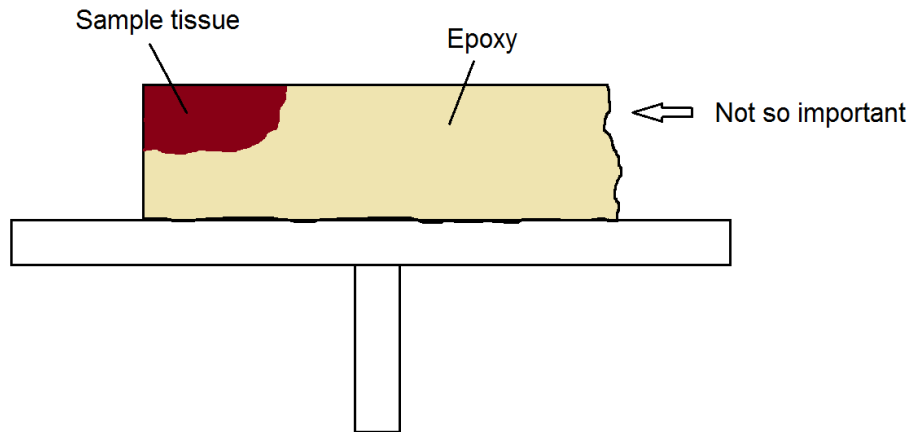


**Figure 17:** Schematic showing the important aspects of the sample geometry of a S&V sample. The edge between the face to be imaged and the top surface must be 90 degrees, and these two faces must also be completely flat and smooth. The material of interest must be positioned on this 90 degree edge.

tissue in the best possible way [57].

Another issue with biological samples is that they are insulating and almost entirely composed of light elements such as carbon, oxygen and hydrogen. If electrons impinge on an insulating sample they have no place to go, so they build up on the sample surface and cause distortions in the incoming electron beam as well as in the outgoing electron signal. The resulting effects are called charge effects, and hinders the observation of realistic sample features. Biological samples therefore need to be coated with a conductive layer prior to imaging. The light element composition becomes a problem when internal structures other than surface topography are to be observed, as in TEM for example. An unstained biological thin section is simply electron transparent, and staining with electron dense elements is necessary to make tissue structures distinguishable from each other. In FIB/SEM tomography, flat surfaces without topography are imaged with the electron beam, and imaging therefore also depends on heavy elemental staining. Since staining chemicals are what creates the contrast, it is important to keep in mind that everything is observed indirectly in biological electron microscopy.

In the following some chemicals used for fixation and staining of biological material will be introduced. The methods were originally developed for TEM inspection of thin sections, but have later been adapted for *en block* sample preparation procedures. *En block* refers to tissue in bulk, as opposed to tissue in thin sections. Staining *en block* is more sensitive to the diffusion rate of various chemicals in the relevant tissue, and is dependent on the staining elements being able to penetrate through the whole sample block. Apart from that the staining principles are the same. The focus of this section will be on the essential chemicals and their functionality, not on the sample preparation procedure per se.

The use of aldehydes for tissue fixation was introduced by Sabatini et. al. in 1963 [58], and has been considered the best form of primary fixative since then. Aldehydes fix tissue structures by chemically crosslinking proteins, following the mechanism shown in Figure 18 [57]. Substances other than proteins are trapped in a matrix of crosslinked proteins and hence become indirectly fixed [59]. Glutaraldehyde is usually the aldehyde of choice, sometimes in combination with a formaldehyde due to formaldehydes increased penetration rate in tissue compared to the former. Formaldehyde penetrates faster because it has a lower molecular weight than glutaraldehyde, but the larger size of the latter allows for crosslinking of proteins further from each other and results in more stably fixed tissue.

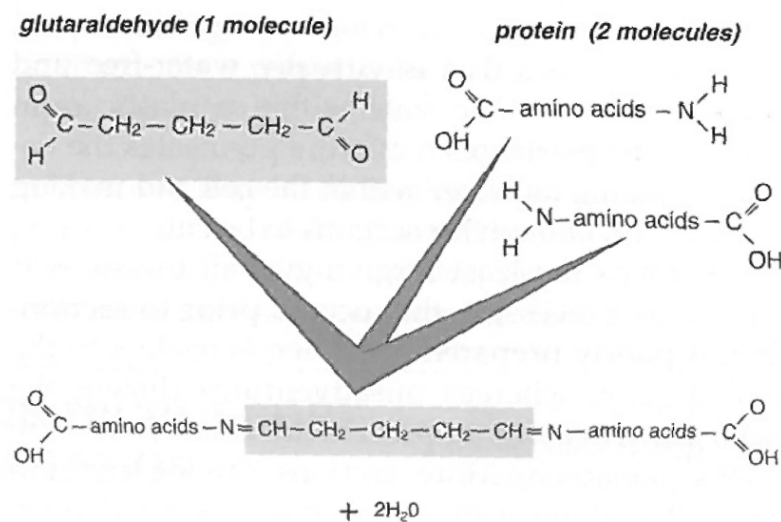


**Figure 18:** Schematic showing how glutaraldehyde crosslinks with proteins to fix tissue. From reference [57].

Osmium tetroxide ( $\text{OsO}_4$ ) was used as a primary fixative before the introduction of aldehydes, and is now used as a very common postfixation chemical, either after or together with glutaraldehyde. This was also described by Sabatini and his colleagues, who proposed that  $\text{OsO}_4$  further stabilises structures conserved by aldehyde fixation, and is necessary to make the tissue withstand further dehydration and plastic embedding [58].  $\text{OsO}_4$  is soluble in both polar and nonpolar media, but will only be retained in nonpolar environments when reduced to lower oxidative states [60]. The reaction mechanisms between  $\text{OsO}_4$  and various cellular components are complex and not well described, but one reaction that occurs with the unsaturated bonds of fatty acids is shown in Figure 19 [57]. As osmium is a heavy metal of atomic number 76, this not only stabilises tissue but also increases tissue contrast, especially in fatty membranes.

A second usual method of postfixation/staining uses a solution containing potassium ferrocyanide ( $\text{K}_4\text{Fe}(\text{CN})_6$ ) and osmium tetroxide. The potassium ferrocyanide reduces  $\text{OsO}_4$  to oxidative states that are more reactive, and the staining effect becomes more

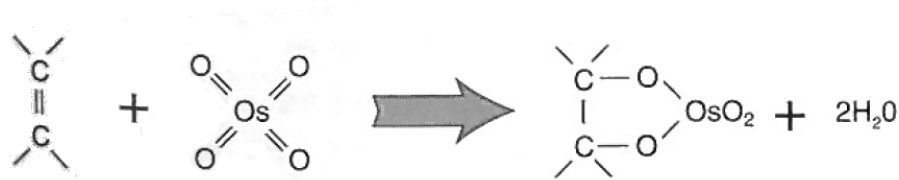


**Figure 19:** The reaction between osmium tetroxide and an unsaturated bond of a fatty acid [57]

pronounced compared to results obtained with  $\text{OsO}_4$  alone [61]. This postfixation method particularly enhances membrane and glycogen contrast, but at the same time it extracts proteins and nucleic acids present in the cytosol and thus reduces the contrast of the cytoplasmic matrix [57, 62]. A TEM image of a sample fixed in  $\text{K}_4\text{Fe}(\text{CN})_6$  and  $\text{OsO}_4$  for 24 hours is shown in Figure 20.



**Figure 20:** TEM image of rat liver tissue fixed in a solution of  $\text{OsO}_4$  and  $\text{K}_4\text{Fe}(\text{CN})_6$  for 24 hours. Image taken by Goldfischer and colleagues [62].

As noted these sample preparation protocols were originally developed for TEM observation of biological tissue, and fixation is not sufficient to make biological tissue strong enough to withstand thin sectioning. An embedding medium is needed for extra support. The use of epoxy resins for this purpose was introduced in 1956 [63], and their use has continued ever since. Epoxies are thermosetting polymeric resins containing the

epoxide chemical group. These groups crosslink with each other through a reaction that is enhanced at increased temperatures and in the presence of a suitable hardener. For embedding water is first gradually exchanged with a solvent (ethanol or acetone) before the solvent is itself gradually exchanged with epoxy. The epoxy and the hardener must be thoroughly mixed before embedding, but without including air bubbles that would appear as artifacts upon inspection. Epoxy is so widely used because it causes minimal damage to the embedded tissue, evenly penetrates and polymerizes without shrinkage. After curing, epoxy embedded tissue is stable for years, and the plastic is hard enough to be cut into thin slices without sample deformation.

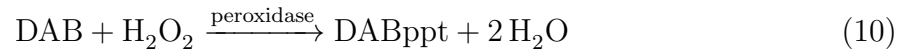
Tissue embedded in epoxy does not usually acquire sufficient contrast from fixation in  $\text{OsO}_4$  because of the relatively high electron density of epoxy [64]. For additional staining heavy metal salts can be added either prior to or post plastic embedding. Uranyl acetate (UA), the acetate salt of uranium, is extensively used for this purpose. UA is a general positive stain, meaning that it attaches to several components in cells and tissue and enhances the density of the structures to be observed [57]. UA is a crystalline powder of high molecular weight, and is dissolved in alcohol solutions for staining of biological tissue [65].

Tannic acid (TA) is an additive sometimes used during fixation/staining procedures, and is believed to act as a mordant for later heavy metal staining chemicals [57, 66]. A mordant is a molecule that reacts with certain structures and later with staining chemicals, so that the contrast of these structures is indirectly enhanced. When used, TA is mostly combined with glutaraldehyde during primary fixation. Postfixation and staining can then be done with  $\text{OsO}_4$  or heavy metal salts such as UA to obtain enhanced contrast compared to tissue prepared with the standard glutaraldehyde- $\text{OsO}_4$  protocol. This method has been successfully applied to enhance membranes [67, 68], extracellular matrix (hyaluronic acid) [69], microtubules [70] and microfilaments [71], amongst other things.

When samples of brain tissue are to be investigated, fixation must be done by perfusion fixation to conserve the structural details in the tissue. To efficiently fix the tissue, formaldehyde is usually included in the fixation solution. The purest form of formaldehyde is obtained from depolymerization of paraformaldehyde, which is usually performed by a heat treatment. To label specific neuronal connections in the brain, anterograde or retrograde tracer molecules are injected at sites of interest. Dextran-amines have been used as carriers for marker molecules since the late 1980's, first in combination with fluorophores and later in combination with the small vitamin biotin [72, 73]. Biotinylated dextran amines (BDA) can function as both anterograde and retrograde tracers depending on their molecular weight (10k for anterograde labelling, 3k for retrograde).

The protein avidin has a very strong affinity for biotin, and the strong and specific binding between these two molecules is at the basis of a range of immunohistochemistry techniques. Avidin has four binding sites for biotin and can be purchased in an avidin-biotin-peroxidase complex (ABC). This complex has the ability to bind additional biotin molecules thanks to the multiple binding sites of avidin. When brain tissue that has

been labelled with biotinylated dextran amine (BDA) is incubated in ABC, the complex persists only in regions where BDA is present. These regions can finally be made visible by reacting diaminobenzidine (DAB) with hydrogen peroxide, a reaction that will only take place in presence of peroxidase (see Equation 10). This reaction results in an osmophilic precipitate (DABppt) that can reduce  $\text{OsO}_4$  to form the electron dense osmium black [60, 74]. In summary, when brain tissue labelled with BDA is treated with ABC and DAB and then postfixed in  $\text{OsO}_4$ , the labelled regions will become visible in electron microscopy through accumulated osmium black.



## 4 Materials and methods

### 4.1 Instrument and software specifications

The instrument used for the experiments performed in this report is a Helios NanoLab<sup>TM</sup> DualBeam<sup>TM</sup> instrument from FEI company. Sputter coating of the samples was done with a Cressington sputter coater model 208 HR. The software used for conducting Slice and View experiments is developed by FEI and is called Auto Slice and View G2. For data processing the open source program Fiji (Fiji.sc) was applied, in addition to the commercial software Amira. Amira is developed by Visage Imaging GmbH, Berlin and the Zuse Institute Berlin. MC simulations were performed using the CASINO software version 3.2.0.1. CASINO is a free software originally developed by Hovington and Drouin at the Sherbrooke University in Quebec, Canada.

### 4.2 Samples

The sample preparation protocols for all the samples investigated in this work will be described in the following. The protocols are summarized in the table in Figure 21.

Name	Sample material	Post-fixation		Staining		
		1% $K_4Fe(CN)_6$ 1% $OsO_4$	1% $K_4Fe(CN)_6$ 2% $OsO_4$	1% $OsO_4$	1% tannic acid	1% uranyl acetate
Alumina sample	<50 nm alumina nanoparticles in epoxy	-	-	-	-	-
Cartilage sample 1	Human chondrocytes in alginate beads, embedded in epoxy	16 h	-	-	1 h	-
Cartilage sample 2		16 h		1 h	-	2 h
Cartilage sample 3		16 h		-	1 h	2 h
Cartilage sample 4		2 h		-	1 h	-
Cartilage sample 5		2 h		1 h	-	2 h
Cartilage sample 6		2 h		-	1 h	2 h
Brain sample 1	Epoxy embedded rat brain with labeled synapses	-	2 h	-	-	1 h
Brain sample 2			2 h	-	-	18 h
Brain sample 3	Flat-embedded rat brain	-	2 h	-	-	-

**Figure 21:** Table summarizing the central steps in the sample preparation protocols of the investigated samples.

#### Alumina nanoparticles

A sample of alumina nanoparticles embedded in epoxy was supplied by Bernt Johnsen from Forsvarets Forskningsinstitut (FFI). The nanoparticles were delivered in powder form from Sigma-Aldrich, with a diameter of <50nm determined by TEM inspection. The nanopowder was first mixed with an anhydride hardener and sonicated for 1 hour at maximum power in a water bath keeping 60 °C. The sonicated solution was then mixed with appropriate ratios of epoxy resin and accelerator, before it was casted in metal moulds. Curing of the composite material was carried out in two steps, one step lasting

for 4 hours at a temperature of 80 °C, and another lasting for 8 hours at a temperature of 140 °C. A sample of thickness around 2 mm was cut off from the molded composite material using a fine saw. It was cylindrical in shape, and no additional trimming of the sample surfaces was performed. The amount of nanoparticles in the composite was given to be 3wt%.

## Brain tissue

Two sections of rat brain tissue embedded in epoxy were supplied by PhD candidate Jørgen Sugar from the Faculty of Medicine, NTNU. The brain samples were collected from female Sprague-Dawley rats (Harlan CPB, Zeist, The Netherlands), as part of a larger ongoing research. The experimental protocol followed the European Communities Council Directive and the Norwegian Experiments on Animal Acts, and was approved by the Animal Welfare Committee of the University. The sample preparation protocol is very similar to the one described in detail by Baks-te Bulte et. al. [75], and will only be summarized here.

In order to tag the relevant neuronal connections, a solution of 5% biotinylated dextran amine (BDA) in phosphate buffer (PB) was injected into the retrosplinal cortex (RSC) of the rat. After 9-14 days of survival the rat was perfusion fixated with a solution of 4% depolymerized paraformaldehyde and 0.1% glutaraldehyde in PB, after which the brain was removed from the skull and postfixed overnight in the same solution. Following fixation the brain was cut in 50 µm thin slices with a vibrating microtome. The thin sections were rinsed in increasing concentration of Dimethyl Sulfoxide (DMSO), before a freeze-thaw procedure was performed twice in order to make the membranes in the tissue permeable for larger molecules. New rounds of rinsing with Tris buffered saline (TBS) was performed, before the sections were incubated with avidinbiotinperoxidase complex (Vectastain ABC kit (Standard), PK-4000) in TBS for 48 h. Following incubation and additional TBS rinsing, the sections were stained in an H<sub>2</sub>O<sub>2</sub>-containing solution of diaminobenzidine tetrahydrochloride (DAB) in buffer. As was seen in theory section 3.4, this forms a DAB precipitate in regions containing AB-complexes and renders the BDA-tagged neuronal connections visible. The reaction was stopped with TBS when labelling was found to be satisfactory upon microscopical inspection. Except for during the freeze-thaw procedure, all solution temperatures were kept at 4 °C.

The region of interest was retrieved and postfixed for 2h in 1.5% Potassium ferrocyanide and 2% OsO<sub>4</sub> in 0.1M PB. After subsequent rinsing, the sections were gradually dehydrated in a series of ethanol in water solutions, ending with a solution of 90% ethanol. From this point, two different samples were prepared, differing only in the duration of the next staining step. Both samples were stained in 2% uranylacetate (UA) in 90% ethanol, but one was stained for 1 hour while the other one was stained over night. Finally the sections were completely dehydrated and gradually embedded in a block of epoxy resin. The epoxy was cured for 4-5 days at 60 °C, before it was trimmed into nicely shaped blocks with the desired geometry using a glass knife mounted on an ultramicrotome.

In addition one flat embedded sample of the same tissue was provided by Bruno Monterotti, also from the Faculty of Medicine, NTNU. This sample was prepared following the same protocol as above, but was flat embedded between two transparent films before any UA staining was performed, and was thus only contrasted from postfixation with  $\text{OsO}_4$ . A region of interest was located using an optical microscope, and an edge was cut with a scalpel. Such flat embedded samples are usually thin sectioned, stained and counterstained in UA and lead citrate for TEM observation. Comparing with the sample as such however, allows for investigation of the effect of further staining steps. It was also of interest to see if the contrast from  $\text{OsO}_4$  postfixation could be sufficient for SEM observation, a fact that would simplify sample preparation and reduce the amount of time required.

### **Artificial cartilage**

Two series of samples composed of tissue engineered cartilage embedded in epoxy were supplied by dr. Olderøy, Rikshospitalet, Oslo. The artificial cartilage was composed of differentiated human mesenchymal stem cells (hMSCs) grown in a matrix of self-gelling alginate. The hMSCs were retrieved from the bone marrow of healthy voluntary donors, as part of a study approved by the Regional Committee for Medical Research Ethics, Southern Norway, Section A. The cells of interest were isolated from the bone marrow by density gradient centrifugation, following the same protocol as the one described in [76]. The MSCs were then mixed with the necessary precursors for creating the alginate gel matrix, and chondrogenic differentiation was induced after gelling was complete. The first series of samples contained  $10 \times 10^6$  cells/mL of alginate-gel, while the second series contained  $50 \times 10^6$  cells/mL. The cells were cultured in the matrix for 6 weeks so that a substantial amount of extracellular matrix (ECM) was allowed to accumulate.

The fixation, staining and embedding procedure was very similar to the one described in more detail in the Nature protocol [77]. A scalpel was used to cut the artificial cartilage into small pieces suitable for further embedding and FIB/SEM inspection. Prefixation was done in a solution of 2.5% glutaraldehyde and 2% paraformaldehyde in 0.1M sodium cacodylate buffer. Postfixation of the samples was performed for 2h or 16h in a solution of 1%  $\text{OsO}_4$  and 1.5% potassium ferrocyanide in 0.1M sodium cacodylate buffer. The rest of the staining steps differed for the various samples, but were a combination of one or more of the following steps: 1h in tannic acid, 1h in UA and 1h in  $\text{OsO}_4$ . See Figure 21 for an overview of the exact fixation and staining steps of the different samples. After staining, the samples were dehydrated in a series of ethanol in water-solutions, the ethanol was gradually exchanged with acetone, and finally the samples were gradually embedded in epoxy. The epoxy was cured at  $60^\circ\text{C}$  over night in block-shaped molds. After curing, two perpendicular faces of the samples were trimmed with a microtome fitted with a glass knife, and manually with a razor blade, respectively, so that the stained cartilage became exposed at the surface. A fine saw was used to cut the other two edges of the epoxy blocks so that they became about 2mm thick and 3mm wide.

## 4.3 Experiments

### 4.3.1 General procedures before imaging and S&V experiments

The artificial cartilage samples were dusty from sawing, and needed to be cleaned in ethanol before further procedures. Otherwise all samples were simply glued onto a standard aluminum sample stub using carbon tape. They were then sputter coated twice at different angles, with a 20 nm layer of platinum/palladium for each time. This was done in two steps at two angles to ensure proper coating of all edges of the samples despite their relatively large height, and hence to ensure good electrical conductivity all over. Without a conductive coating the epoxy samples would be insulating, and severe charge effects would occur.

Some preparation of the sample was done inside the FIB/SEM prior to all the S&V experiments. The sample was first put at eucentric height and at 52 degrees tilt. A region of interest was then located using either 2.7 or 6.5nA beam current for the ion beam, to mill open cross sections in the epoxy-embedded samples. Nothing could be observed prior to milling because of the initial sputter coating-step. When something of interest was located, a 1.2  $\mu\text{m}$  thick layer of platinum (Pt) was deposited on top of the region using the gas injection system (GIS) present on the DualBeam instrument. This was done before further cleaning because curtaining becomes very severe when there is no protective layer of Pt on the surface of the sample. The ion beam was used for Pt deposition, with a current giving a current density of around  $4\text{ pA}/\mu\text{m}^2$  for the chosen area of deposition. A current density in the lower range was used since the areas of interest were rather large (see theory sec:IonSampleInteractions). The ion beam current can only be adjusted by shifting between a certain number of apertures within the beam column, so the deposition area usually needed to be adjusted for an optimal current density. After localization of the exact area to be imaged during the S&V experiment, trenches of about  $6\ \mu\text{m}$  width were milled around it with an ion beam current of 6.5nA. This was done to avoid shadowing and redeposition of milled material during imaging. Cleaning of the cross section was then performed, beginning at 2.7nA and ending at either 0.92 or 0.44nA beam current, depending on the amount of curtaining present. The importance is to remove all traces of curtaining before beginning a S&V experiment, because once present it usually persists throughout a whole run. A proper cleaning is crucial for a successful S&V experiment.

### 4.3.2 Interaction volume-investigations on model specimen

The alumina nanoparticle sample was investigated with the aim of characterizing the volume of origin of the signals collected for image formation. To evaluate the effect of electron beam energy, imaging and S&V experiments were performed at 5kV and 20kV acceleration voltage. Two S&V experiments were performed with the same parameters, except for the acceleration voltage that was set to 5kV for the first run and 20kV for the second. Regular mode was used in combination with the ET detector for image collection. The electron beam current was set to 0.69nA, the resolution to  $2048 \times 1768$  pixels and

the dwell time was set to 10  $\mu\text{s}$ . The number of slices for the experiments was chosen so that the distance between consecutive slices became 15nm, and the ion beam current was set to 0.92nA for milling during the experiment. The milling depth was set to 3  $\mu\text{m}$ . A fiduciary marker of thickness 0.6  $\mu\text{m}$  was used, and ion beam shift images were collected with a resolution of  $1024 \times 884$  and a dwell time of 3  $\mu\text{s}$ .

The imaging experiments on this sample were performed with the exact same parameters as for the S&V experiments described above.

### 4.3.3 MC simulations

Monte Carlo simulations were carried out using the program CASINO v.3.2.0.1. The simulations were done for an electron beam of energy 5kV and 20kV, with the aim of creating supplementary material for the interpretation of the experimental interaction volume investigations described above. An approximate epoxy formula of  $\text{C}_{16}\text{H}_{10}\text{O}_3$  was used, and the corresponding density was set to 1.4  $\text{g}/\text{cm}^3$ . The plasmon energy and work function energy were set to 30eV and 5eV respectively for the epoxy, based on the values for similar materials that were already in the CASINO material library. The alumina particles were simulated as pure aluminium particles for simplicity, because the density and energy values are correct for pure materials in the CASINO databases. The density of Al was hence set to 2.7  $\text{g}/\text{cm}^3$ , the plasmon energy to 15eV and the work function energy was set to 4.28eV. The Al particle radius was set to 250nm for the simulations including a particle. This is quite a lot bigger than the single particles in the alumina sample described above, but was set to this value because quantitative values were not drawn from the experiments, and smaller particles were simply difficult to observe for the chaotic electron path meshwork at 20kV. Simulations were done for 5kV and 20kV electron beams incident on both flat and tilted epoxy samples, with and without the presence of an Al particle. All simulations were done for 1000 incoming electrons, but only 300 electrons were displayed on the drawings because displaying more electrons became chaotic.

### 4.3.4 Imaging

In pervious work done by the candidate [5] imaging was mostly done in regular mode with the ET detector, while immersion mode in combination with the TL detector was not properly explored as an alternative. Here therefore, cartilage samples and brain samples were used to compare the two imaging modes more systematically. Images of the same areas were taken with the same parameters, except for the imaging mode that was changed between the two abovementioned. In order to minimize deposition of hydrocarbon contamination that reduces image quality, the time for focusing was minimized by pausing the electron beam at any time possible. It is also possible to focus at a different area than the one to be imaged, but since immersion mode is so sensitive to the position of the sample it is difficult to obtain good focus for this mode in this manner. The image quality is best for a freshly milled surface, so to avoid favorization of one imaging mode

above the other, the imaging order was interchanged between experiments. The imaging parameters used for the electron beam were typically 5kV acceleration voltage, 0.69nA beam current and 10  $\mu$ s dwell time with a resolution of  $2048 \times 1768$  pixels. The available shift in the electron beam was also compared for the two imaging modes.

A lot of samples prepared with differing sample preparation protocols were investigated in this work. In an attempt to compare the effect of both fixatives, staining chemicals, duration of the different steps and sample geometry, series of images were taken of all the cartilage samples, brain samples and the alumina nanoparticle sample described earlier. Both regular mode and immersion mode were used for image collection, and the imaging parameters were the same as described just above.

For the brain samples it was of interest to see if the labelled boutons (part of a chemical synapse) could be observed and distinguished from non-labelled boutons in the FIB/SEM. Therefore a thorough investigation of the 1h brain sample was performed in collaboration with Jørgen Sugar for assistance on biological image interpretation. A systematic search of the prepared tissue was performed by milling open 6 areas of about 50  $\mu$ m width, leaving pillars of coated epoxy between each area to avoid excessive charge effects. Several images were taken of each area, at a magnification sufficiently high to distinguish eventual boutons.

Deposition of hydrocarbon contamination layers was a more or less serious issue common for all the imaging experiments performed on the relevant samples. Imaging was therefore also performed with liquid nitrogen (LN2) in the cooling chamber on the side of the FIB/SEM instrument. As noted from theory section 3.1.3 this is supposed to trap hydrocarbons present in the sample chamber, and reduce the amount of adsorbed molecules on the sample surface. Imaging with LN2 was done on the alumina nanoparticle sample.

#### **4.3.5 S&V experiment on artificial cartilage**

One S&V experiment was performed on cartilage sample number 3, with assistance from Magnus Østgård Olderøy to find a biologically relevant region of interest (ROI). The ROI was chosen so that the investigated volume would include part of a cell, its immediate surroundings and the matrix a little further from the cell. Since the importance is to know to what extent the osteocytes have produced and secreted collagen, the surrounding matrix is the most interesting to observe rather than the cells themselves. Immersion mode was used in combination with the TL detector for image collection during the S&V experiment. The electron beam acceleration voltage was set to 5kV, the beam current to 0.69nA, the resolution to  $2048 \times 1768$  pixels and the dwell time to 10  $\mu$ s. The number of slices for the experiments was set so that the slice thickness became 22nm, and the ion beam current was set to 0.92nA for milling during the experiment. The milling depth was set to 4  $\mu$ m, deeper than for the alumina nanoparticle sample since the region of interest was located some distance down from the surface. A fiducial marker of thickness 0.6  $\mu$ m was used, and ion beam shift images were collected with a resolution of  $1024 \times 884$  and a dwell time of 3  $\mu$ s.

### 4.3.6 Data processing and 3D rendering

Most data processing was done with the open source program Fiji. All images were inverted by inverting the lookup table (LUT), to make the comparison with TEM images more straightforward. When imaging parameters were to be compared, nothing but the LUT, brightness and contrast (B/C) was adjusted. This because all data processing obscures the original result, and makes it difficult to compare different images objectively.

When a realistic rendering of the investigated area was a goal, the images were scaled with a factor of 1.27 in y-direction using a bicubic interpolation. This scaling is necessary because of the geometry of the beams within the sample chamber, as shown in Figure 22.

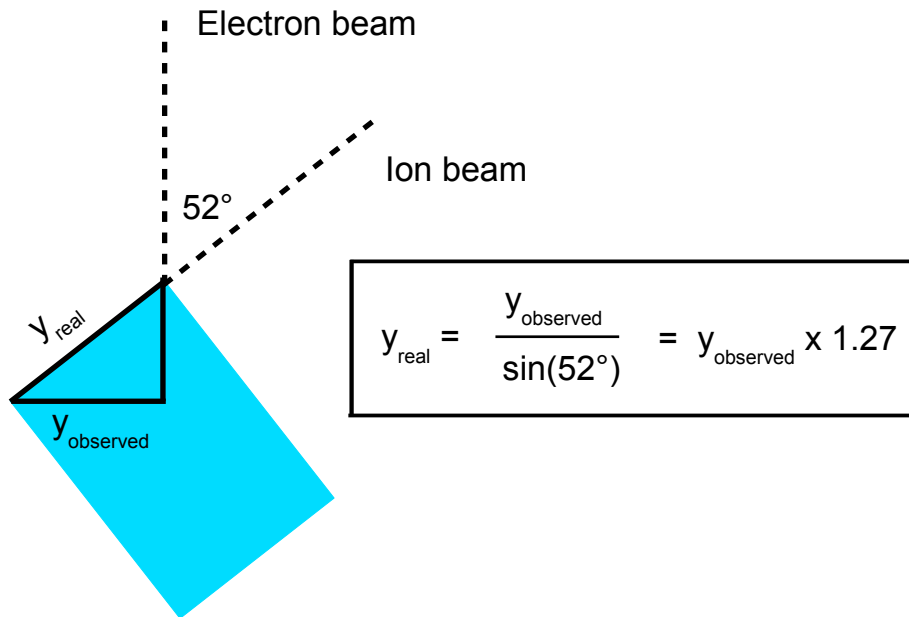


**Figure 22:** Geometric construction showing why images must be scaled with a factor of 1.27 in y-direction in order to show the realistic shape of observed objects.

The stacks resulting from the interaction volume experiments done on the alumina particle sample were first aligned using the plugin StackReg in Fiji. The transformation was set to translation, which only corrects for shift in the xy plane and not rotational differences. The stacks were then cropped to remove empty space created by the alignment. The stacks were to be investigated as a volume, and since this requires heavy computational forces they were first scaled by a factor of 0.5 using a bicubic interpolation. Next they were imported to Amira, with a scale factor of 1.27 in y-direction and 1.44 in z-direction. The z scaling comes from the fact that the stacks were not collected with a slice thickness giving cubic voxels: The slice thickness was set to 15nm, and the width of a pixel was 5.2nm. For a full size stack the voxels should then be multiplied by 2.88 in z-direction, becoming 1.44 for a stack of half the pixel size. In Amira the stacks were investigated as a volume using thresholding to distinguish particles from the epoxy background. This works nicely for such a sample, where all the particles are bright against a dark background. To give a representation of the interaction volume, the 20kV

stack was thresholded twice, once with a small value including the weak signals appearing before the particles, and one with a higher value including only the particles themselves. Both stacks were also imaged from the side (along the z-axis) by using the orthoslice representation.

The stack resulting from the S&V experiment done on the tissue engineered cartilage sample was processed using both Amira and Fiji to represent the material in 3D. Alignment was first performed, using StackReg as described above. Two small parts of the stack were then cropped out for further analysis, because the tissue was complex and the stack as a whole contained a lot of information.

The first small stack only contained collagen and alginate. The brightness and contrast was adjusted by restraining the maximum and minimum values for the histogram. Scaling was then performed, with a value of 1.27 for y and 2.28 for z, using bicubic interpolation. The z value comes from the fact that the slice thickness was 22nm for the S&V experiment, while the pixel width was 9.65nm. No downscaling was performed since the stack was cropped to a sufficiently small size for the computer to handle. The background was then subtracted using the subtract background process with a radius of 100. A suitable threshold was chosen to transform the images to binary images, with the collagen and alginate being white against a black background. This binary stack was then converted to a 3D representation using both Amira and Fiji. In Fiji the plugin 3D viewer was applied with a threshold of 50 (arbitrary since the stack is binary) and a resampling factor of 2. In Amira a labelvoxel was used to set the threshold to 50 and create a lebelfield, from which a surface was created that was then displayed as a volume in 3D.

The second small stack was centered around a cell, and was rendered in 3D using Fiji following the same procedure as above (except for background subtraction). There were some variations in the brightness and contrast in the stack, so B/C adjustments were done on individual slices in order for a single threshold to be representative for the whole stack. The ER membranes in this stack were manually traced in Amira to create a 3D model.

## 5 Results

### 5.1 Acceleration voltage-dependent interaction volume

The DualBeam FIB/SEM offers the unique possibility of revealing what is actually underneath an imaged surface, and this should allow to get an impression of the interaction volume. The principle is demonstrated in Figure 23. If the interaction volume is big enough some signal will be collected from a particle even though it is not at the imaged surface. When a slice of material is milled away, the particle can be directly observed. A qualitative result can be obtained by imaging a surface before milling off a slice of material to see what is some distance underneath. A more quantitative result can be obtained using the Slice and View software, where the knowledge of the exact slice thickness allows the user to determine more accurately how far before an element the signal is detected during imaging. Both methods were tested here for two different acceleration voltages, 5kV and 20kV. The acceleration voltages were chosen such that they both gave good quality images, while still being different enough to give an impact on the observed interaction volume. All imaging was done by detecting the secondary electron signal, so all signal that was detected from a certain depth can be attributed to the collection of  $SE_2$  and  $SE_3$ . This is the reason why the paths of BSEs instead of SEs were investigated during MC simulations to explain the observed signal volume results.

The qualitative imaging result is shown in Figure 24. Three secondary electron micrographs were collected at 5, 20 and 5kV acceleration voltage, respectively. The magnification is the same for all three images, and the two first show the exact same area of the sample. Similar structures are observed on both images, except for two rather large dots with lower intensity than the rest of the particles, that are only visible in the 20kV image. The third image is collected after removal of a slice of material with the ion beam. The removal of material allows for observation of what is actually underneath the initially imaged surface, and reveals in this case two alumina particle aggregates situated exactly below the dots observed in the first 20kV image.

The effect of the acceleration voltage on the signal produced was further investigated by conducting two S&V experiments on the epoxy alumina nanocomposite sample, one at 5kV and one at 20kV acceleration voltage. For the 20kV experiment, a weak signal appeared quite long before the particles were actually in the plane of imaging. The signal coming from a particle beneath the surface and the signal from a particle in the slice plane are easy to distinguish since the difference in intensity is abrupt at the transition. This can be observed in Figure 25. The same figure shows that this weak signal is not present in the 5kV stack. The 3D reconstruction of the 20kV stack in Figure 25 gives a more visual representation of the effect. It can be seen that the weak signal is inclined with respect to the sample surface. The degree of inclination is not constant all over, but was measured to values between 52 and 59 degrees using an angle measuring tool in Amira. From the 3D reconstruction it is also evident that the large agglomerates have a longer tail than the smaller particles. When viewing through the collected stack the weak signal

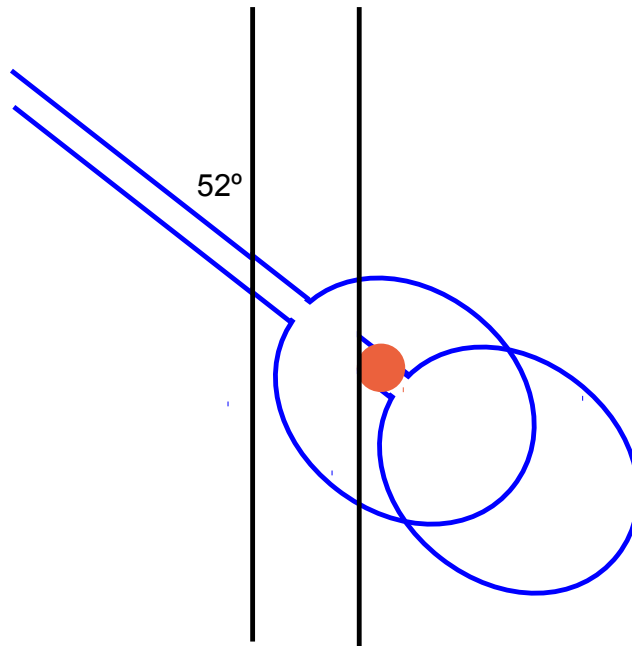


**Figure 23:** A schematic showing the principle behind the interaction volume investigations carried out in this report. The blue shapes represent the electron beam and its interaction volume, while the orange circle represent a particle within the sample. The two black lines are the imaged sample surface before and after the removal of a slice of material. Before removal, the particle is not at the surface but the interaction volume is so big that a weak signal should still result from its presence. After slice removal, the particle is at the imaged surface and should be at the origin of a strong signal. A goal was to compare this effect for a 5kV and a 20kV electron beam.

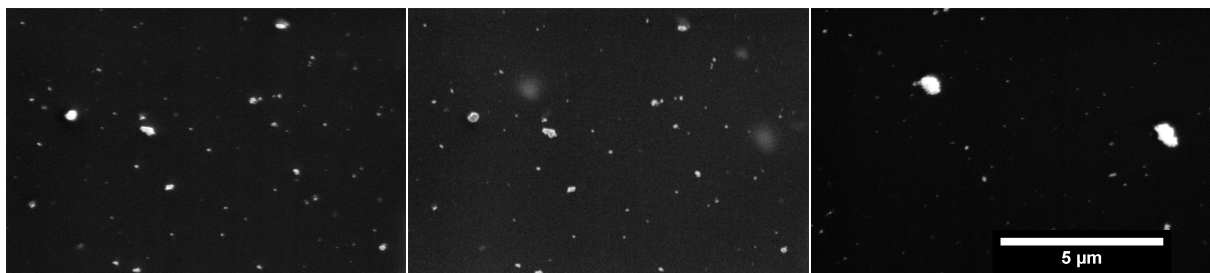


**Figure 24:** Secondary electron micrographs collected in regular mode with the ET detector, using a current of 0.69nA and a magnification of x8000 for the electron beam. The two first micrographs show the exact same area of the same sample surface, but differ in the acceleration voltage used for the electron beam during imaging. This was set to 5kV for the first and 20kV for the second micrograph. The third micrograph was collected at 5kV acceleration voltage, after having removed a slice of material with the ion beam. A weak signal is observed only in the 20kV image.

appeared between 10 and 40 slices before the actual particle. Since the slice thickness was 15nm, this corresponds to values ranging from 150 - 600nm.

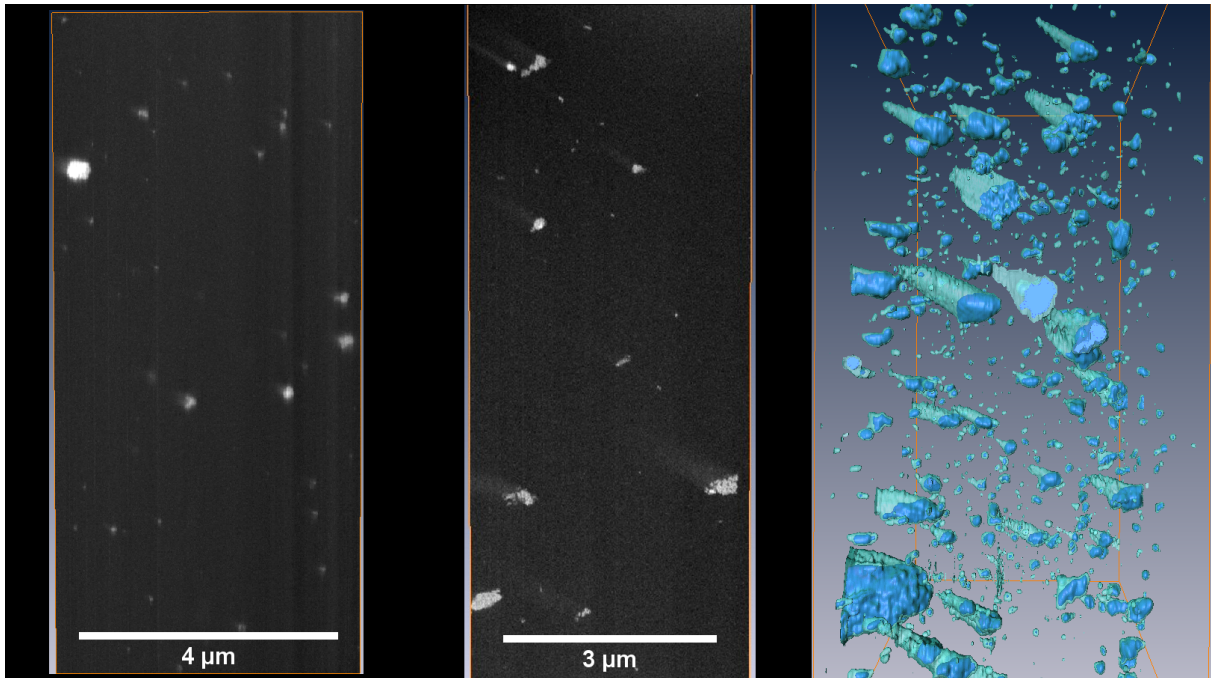


**Figure 25:** Two stacks were collected at 5kV and 20kV acceleration voltage respectively, using 0.69nA beam current and the ET detector in regular mode. Using Amira the stack can be observed from any direction, and the two first images above are cross sections in the yz plane (sideview) of the two stacks. This means that images were collected perpendicular to the plane of view, from left to right. A volume reconstruction of the 20kV stack is shown to the right. This is also seen from the side, and two different thresholds are represented with two different colours. A lower threshold is represented in transparent turquoise and show the weak signal in the stack, while a higher threshold is represented in blue and show the strong signal in the stack. The stack was collected from left to right with respect to this 3D reconstruction.

The graphical result from simulating a 5kV and a 20kV electron beam incident on a flat epoxy sample using MC algorithms is shown in Figure 26. Within the epoxy sample there is an Al particle of 500nm in diameter situated at 500nm below the surface. This particle is identical in size and position for both the 5kV and 20kV simulations, but is only barely visible in the 20kV simulation because the chaotic electron paths mask the particle. 300 electron paths are displayed for both images in the figure, and BSEs are traced in red. The figure clearly shows the large difference in interaction volume between a 5kV and a 20kV electron beam incident on an epoxy sample. The 20kV beam has a penetration depth of about 6 μm (corresponding to the thickness of the sample in the simulation), while the 5kV barely touches the Al particle at the bottom of its interaction volume, corresponding to a penetration depth just above 0.5 μm. For the 5kV beam, no BSEs originate from the region where the interaction volume overlaps with the top of the particle, while for the 20kV beam the particle is situated in the upper part of the interaction volume, and many BSEs originate from this region. This is difficult to see in

Figure 26, and a close-up is therefore shown in Figure 27. Here the sample has been tilted to 52 degrees to give a more realistic impression of the actual experimental situation. The scalebar on this image shows that the BSE signal originates from a depth of approximately  $1\ \mu\text{m}$  into the sample.

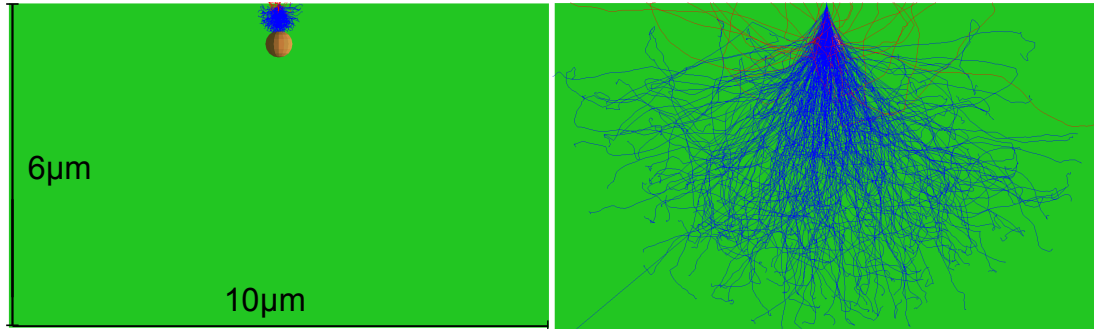


**Figure 26:** MC simulations showing a 5kV and a 20kV electron beam incident on a flat epoxy target of size  $10 \times 6\ \mu\text{m}^2$ . For both simulations there is an Al particle of size 500nm in diameter situated at 500nm below the sample surface. 300 electron paths are shown and BSEs are traced in red.

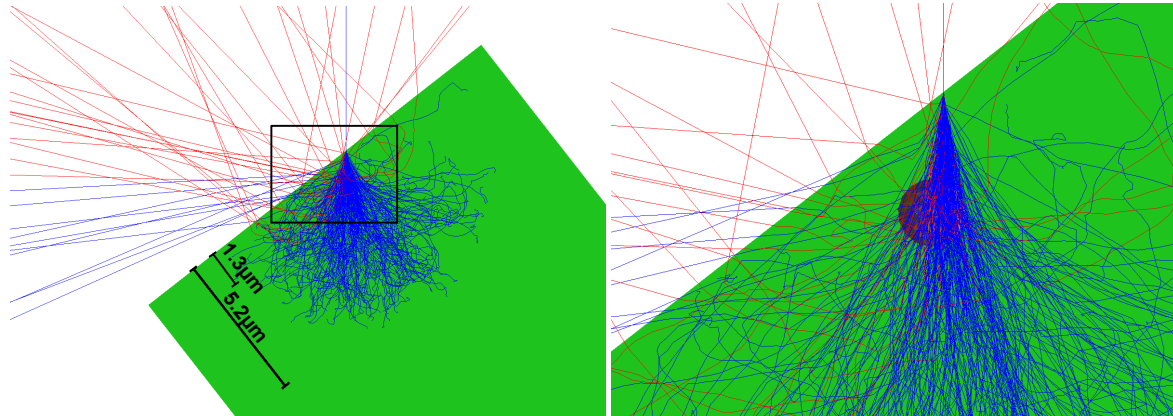


**Figure 27:** MC simulation showing a 20kV electron beam incident on an epoxy target tilted to 52 degrees. There is an Al particle of size 500nm in diameter situated at 500nm below the sample surface. 300 electron paths are shown and BSEs are traced in red. The two images are of the same simulation, where the inset to the left mark the area shown to the right. A large Al particle at this depth is situated in a region of the interaction volume where imaging signals will be detected from.

## 5.2 Imaging

Electron beam induced hydrocarbon deposition was observed for all the samples investigated in this work. The effect is present in most of the images that will be presented in

this section, so hydrocarbon depositoin effects in themselves are therefore first reviewed. Immersion mode and regular mode images will then be presented, followed by the result of the bouton search on the 1 hour brain sample.

### 5.2.1 Hydrocarbon deposition

Figure 28 shows the effect of hydrocarbon deposition during regular operation, on cartilage sample number 4 and the 1h brain sample, respectively. The contamination effect varied from sample to sample, and was particularly severe for cartilage sample number 4, as can be observed in Figure 28. The large white square is the result of only one image captured at 10  $\mu$ s dwell time, and it looks quite thick and very sharply defined. The image of the brain sample shows the more usual effect, where imaged areas become slightly more diffuse and with a worse contrast then the non-imaged areas. The effect is thus more or less severe, but was a challenge for all the samples observed here. It obscures the contrast in the sample, and in addition the hydrocarbon deposition layers proved quite difficult to mill away with the ion beam, compared to the surrounding epoxy. This can be observed to the right in Figure 29. This figure shows two images taken during microscope operation with liquid nitrogen in the cooling chamber, which is supposed to reduce the effect of contamination deposition. To the left in the figure two images have been collected with a dwell time of 10  $\mu$ s before the electron beam was zoomed out to image the resulting hydrocarbon deposition. Small areas with extra deposition are observed, and these result from the electron beam focusing that was performed with a reduced scan area size. After imaging the ion beam was used to clean the imaged surface, and the image to the right in Figure 29 shows the appearance of the surface after initial cleaning. The epoxy surface is black and clean everywhere except for at the area where imaging was performed with the electron beam. This indicates that the hydrocarbon deposition is harder to mill away then the epoxy itself.

### 5.2.2 Immersion mode vs. regular mode

Two secondary electron micrographs of the rat brain sample stained in UA for 1 hour are shown in Figure 30. The first micrograph is collected with the ET detector in regular mode, and the second with the TL detector in immersion mode. Details such as membranes and synapses are more readily discerned in the immersion mode image, but it appears blurred on the top and bottom edges. The regular mode image has a worse overall resolution, but the whole image is equally in focus. Figure 31 is another comparison between regular mode imaging with the ET detector and immersion mode imaging with the TL detector. A cell from cartilage sample 3 was imaged, and even though the magnification is slightly lower in the immersion mode image, structures within the cell are more easily discerned. When looking closely at the regular mode image, the cell interior is mostly a blurr and structures such as membranes can not be followed. This is possible in the immersion mode image, and this imaging mode is thus necessary to use if one wants

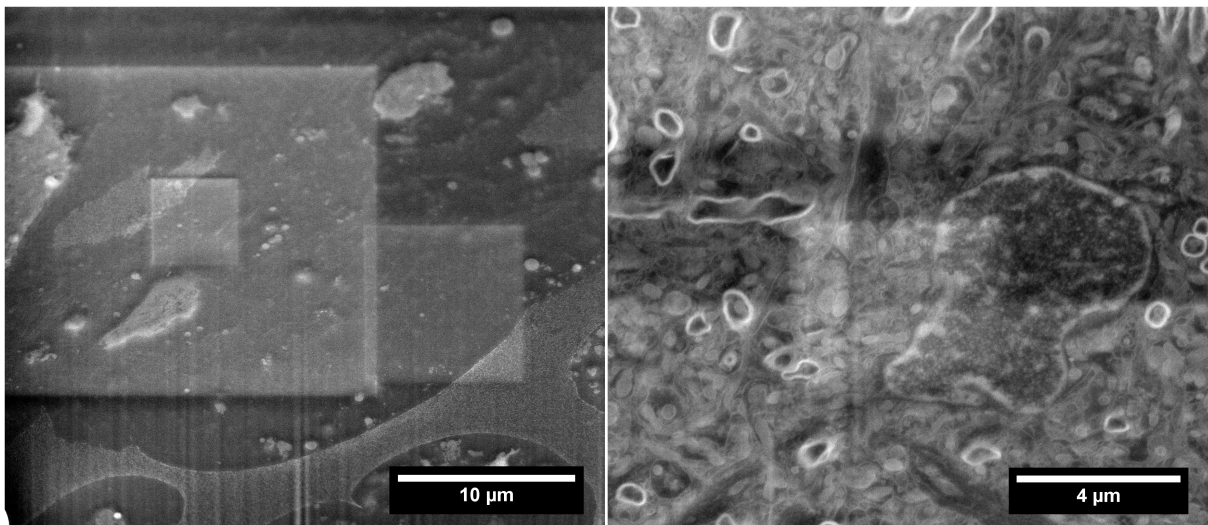


**Figure 28:** The left image is an immersion mode micrograph of cartilage sample number 4, collected with the TL detector in SE mode. The right image is a regular mode image of the 1h brain sample, collected with the ET detector in SE mode. The acceleration voltage was 5kV and the beam current 0.69nA for both.

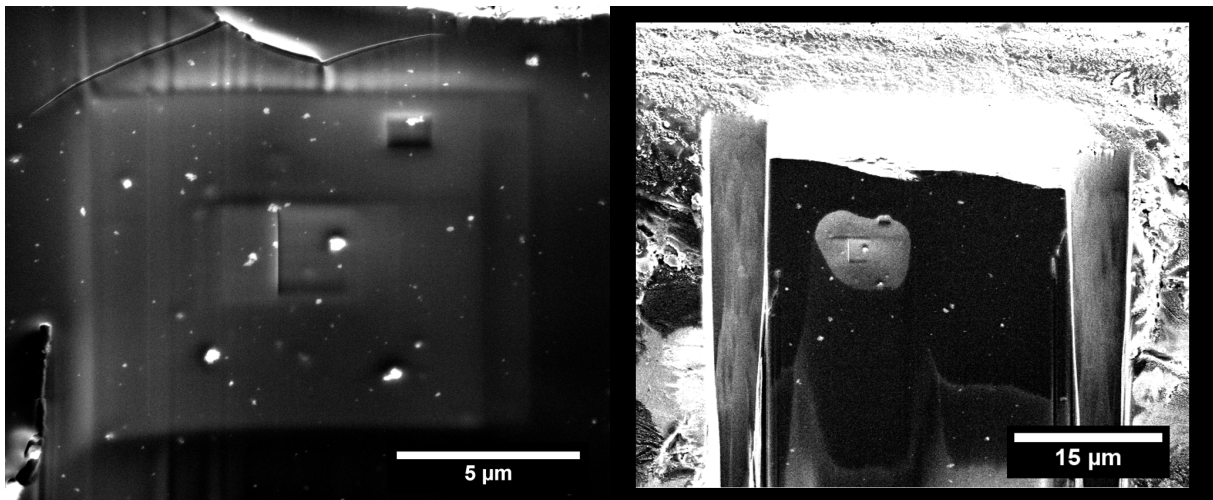


**Figure 29:** Two secondary electron micrographs collected with the ET detector in regular mode. The images were taken while LN2 was present in the cooling chamber of the FIB/SEM instrument. The left image shows the deposition resulting from quick focusing at reduced areas and capturing of two images with a dwell time of 10 μs. The right image is taken after some cleaning with the ion beam.

to follow such fine structures within a cell during a S&V experiment. A final example is shown in the close-up image of extracellular matrix from cartilage sample number 6, in Figure 32. The fine structure of the fibrils is sharper and more easily observed when immersion mode is used in combination with the TL detector. The difference becomes even more evident at this magnification.

When the available shift in the respective modes was tested, it was found that the electron beam can be shifted a total of  $50\ \mu\text{m}$  ( $\pm 25\ \mu\text{m}$ ) in regular mode, versus a total of  $10\ \mu\text{m}$  in immersion mode. Another difference is that immersion mode can only be operated at magnifications higher than  $\times 2000$ , while regular mode is available over the whole magnification range.

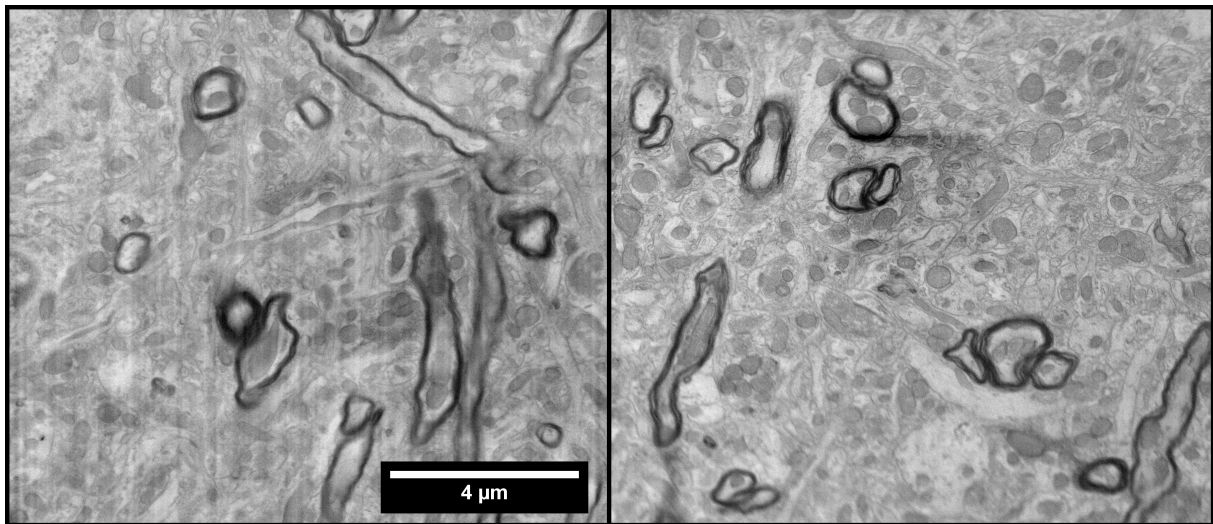


**Figure 30:** Secondary electron micrographs of rat brain tissue stained for 1h in UA. Both images have a magnification of  $\times 10\ 000$  and have not been cropped. The image to the left was collected with the ET detector in regular mode, while the image to the right was collected with the TL detector in immersion mode.

### 5.2.3 Bouton search in brain samples

A bouton is the terminal bulb of an axon, and can be selectively labelled by anterograde labelling from the cell body, according to the mechanism described in section 3.4. A thorough search for labelled boutons was carried out on the brain sample stained in UA for 1 hour. The systematic approach is illustrated in the overview image in Figure 33.

The appearance of a labelled bouton when imaged as a thin section in TEM is shown in Figure 34. It is recognized by somewhat diffuse dots of very strong contrast. Similar structures in the surroundings have distinctly lower contrast, and the bouton is hence identified with certainty. Figure 35 shows typical images from the bouton search on the 1h brain sample performed within the FIB/SEM. The arrows in the left image point to various tissue details, and indicate that even at such a low magnification ( $\times 6500$ ) the tissue contrast is sufficient to recognize essential details in the tissue. The right image is collected at a higher magnification, and shows that the resolution is good enough for

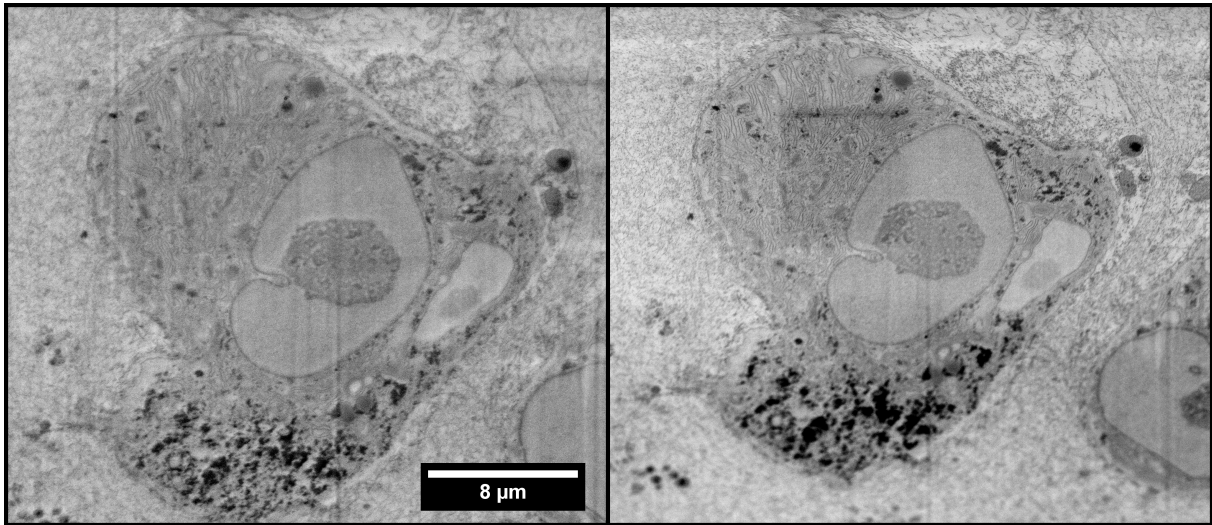


**Figure 31:** Secondary electron micrographs of a cell in cartilage sample number 3. The image to the left was collected with the ET detector in regular mode, while the image to the right was collected with the TL detector in immersion mode.

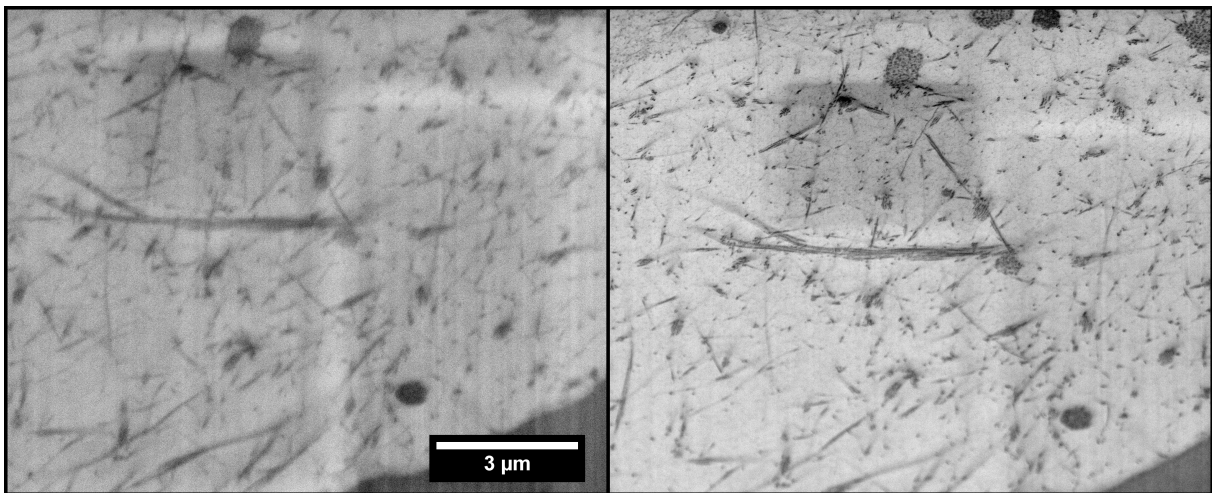


**Figure 32:** Secondary electron micrographs of collagen fibrils in cartilage sample 6, collected at x10 000 magnification. The image to the left was collected with the ET detector in regular mode, while the image to the right was collected with the TL detector in immersion mode.

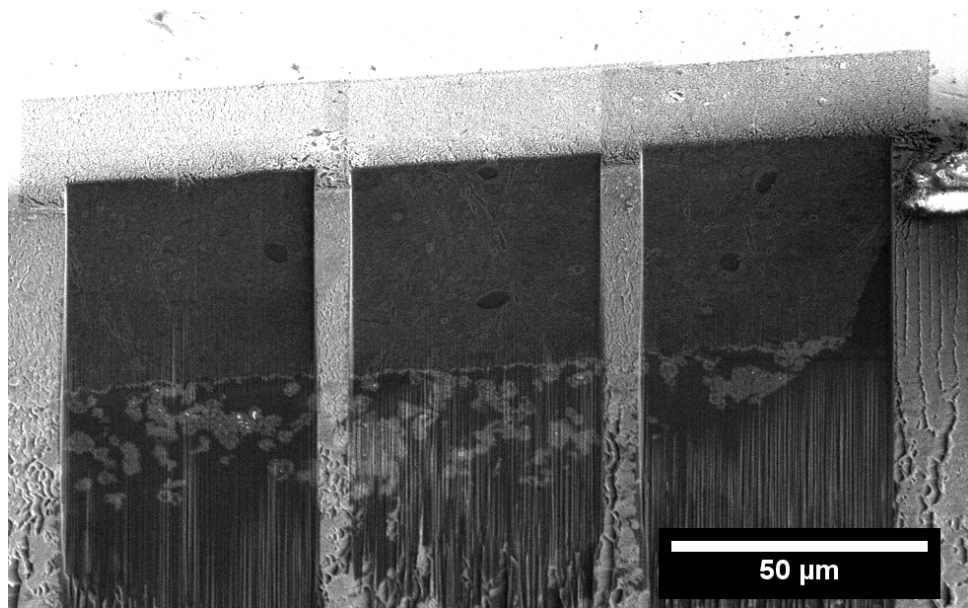


**Figure 33:** Secondary electron micrograph of the 1h brain sample, showing how a systematic bouton search was performed on a large part of the sample tissue. The image shows 3 of in total 6 areas that were investigated. The cross section width is approximately 50  $\mu\text{m}$ .

boutons to be discerned. Around 40 images of 6 cross sections were collected, but no labelled boutons could be distinguished with certainty.

### 5.3 Sample requirements for FIB/SEM tomography

#### 5.3.1 Abundance of interesting material

The first series of cartilage samples contained  $10 \times 10^6$  cells/mL of alginate gel, which is the concentration used when engineering cartilage for implantation purposes. This density is satisfactory for optical microscopical investigations, as shown to the left in Figure 36. When the same density of material is to be investigated in a SEM however, a lot of the sample will be composed of apparently empty epoxy. This effect is illustrated to the right in Figure 36, where white arrows point to two cells that were revealed after milling open several cross sections. Here two cells were actually located, but often nothing of interest was found in these low density samples. Another problem for a sample of low density is illustrated in Figure 37. The figure is composed of two images, one of a low density cartilage sample and one of the flat embedded brain sample. In both cases it was possible to locate some tissue of interest, but this region was located so far down into the sample that it was inaccessible for a S&V experiment.

#### 5.3.2 Sample geometry

The tissue engineered cartilage samples were cut with a razor blade on the top edge. Such an edge at low and medium magnification is shown in Figure 38. The images show that the exact appearance of the surface is somewhat uneven in nature. It is quite flat and

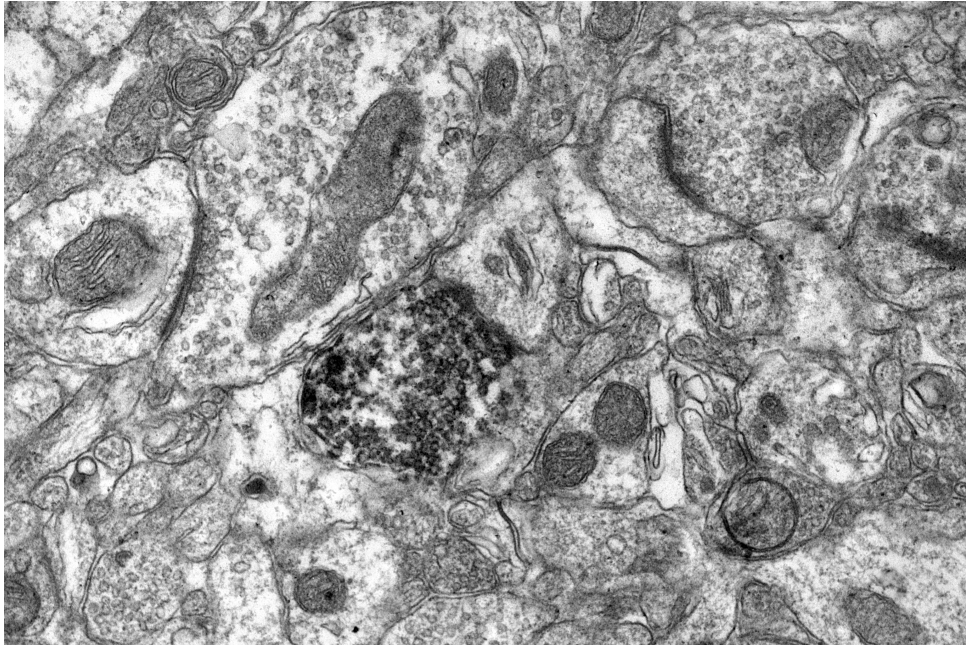


**Figure 34:** TEM image showing a labelled bouton standing out with a darker contrast than the surrounding material. Courtesy of Jørgen Sugar. The magnification of the image is x40 000

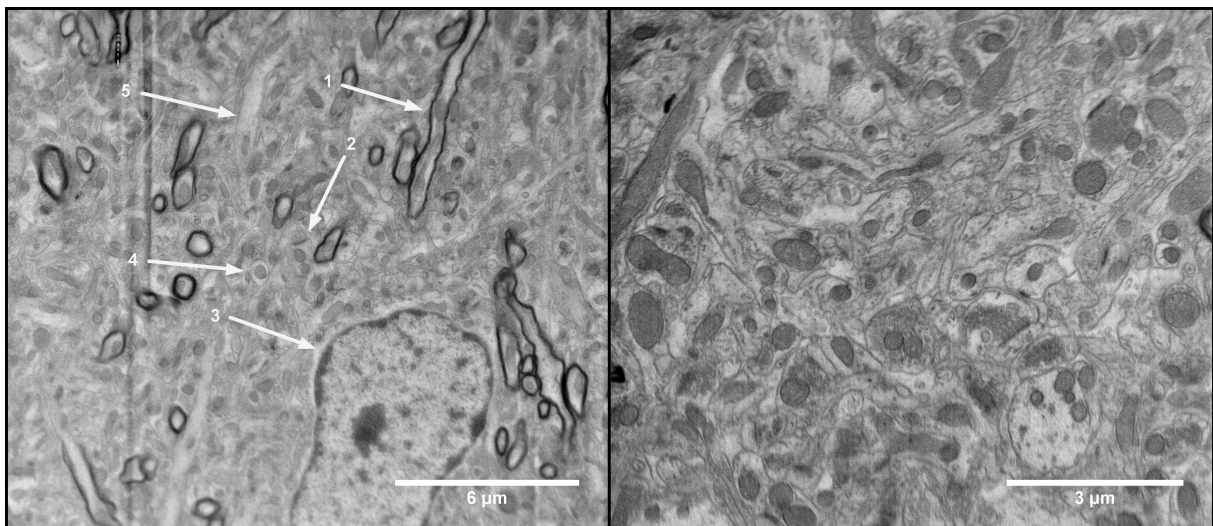


**Figure 35:** The left image is a secondary electron micrograph of the 1h brain sample, collected with the TL detector in immersion mode and at 6500x magnification. The electron beam acceleration voltage was 5kV and the beam current 0.69nA. The arrows point to details in the tissue. 1: Myelin-coated axone, 2: Synapse, 3: Cell, 4: Cross section of a dendrite, 5: Also cross section of a dendrite, but along the long side. To the right is a secondary electron micrograph of the same sample collected with the same detector and beam parameters, but with a magnification of x12500.

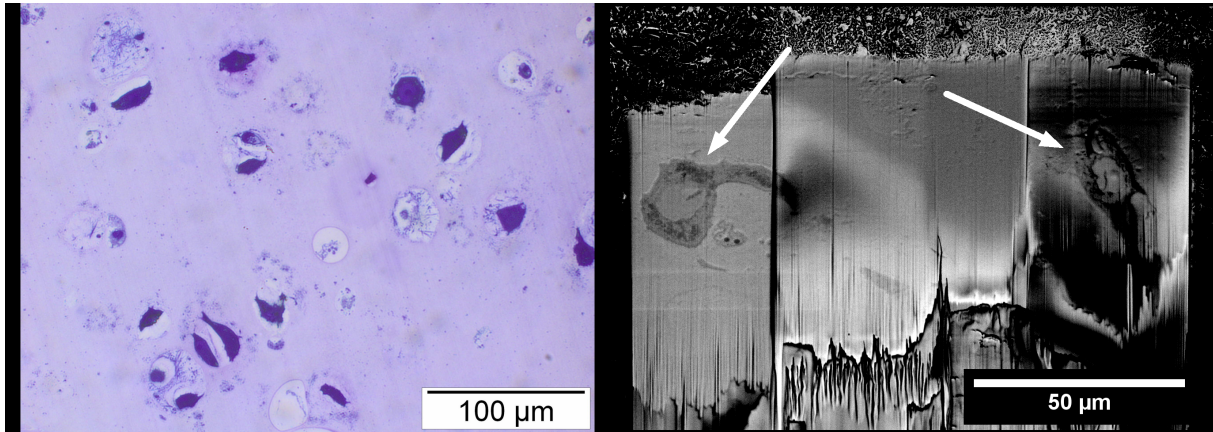


**Figure 36:** Montage showing the cell density in the first series of cartilage samples. To the left is an image taken in the optical microscope (courtesy of dr. Olderøy) and to the right is a SEM image collected in the FIB/SEM.

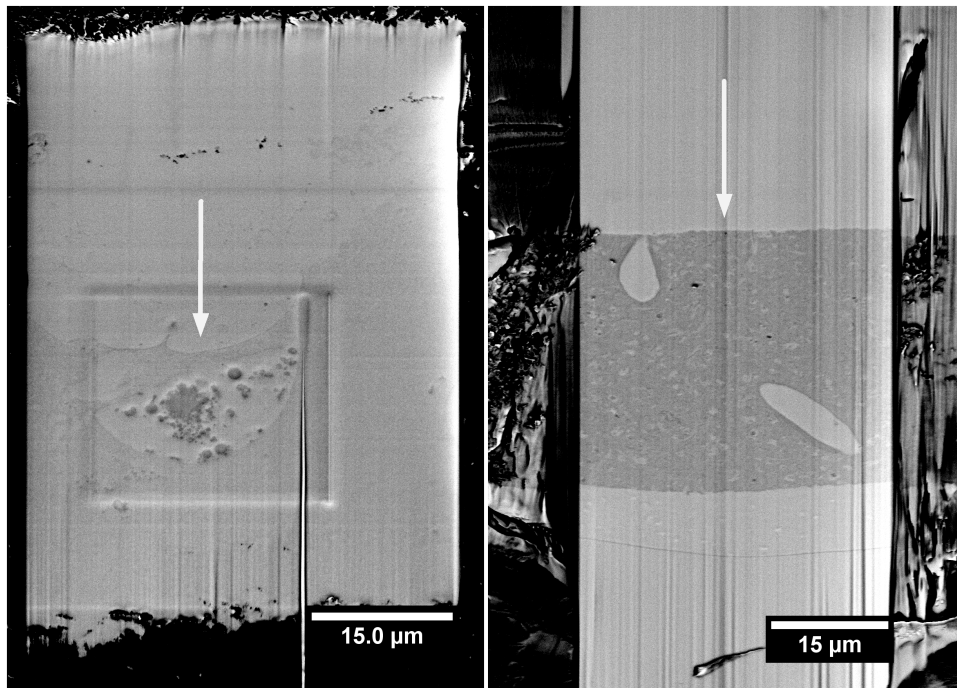


**Figure 37:** Two secondary electron micrographs of a low density cartilage sample and the flat embedded brain sample, respectively. The arrows point to the material of interest which is located far down from the top sample surface. Since the sample must be at eucentric height during a S&V experiment the ROI must be within the shift range of the electron beam, which is not the case here.

smooth at certain parts of the top surface, but edges and bumps are present here and there. In addition the outmost edge is not 90 degrees, but there is a slanted part between the top surface and the face to be imaged. The cross section that has been milled open on the second image in Figure 38 renders this slanted edge more visible. It can be seen that it does not arrive at the top surface where it needs to be before beginning a S&V experiment, and more milling would be required. It can also be seen that this slanted edge becomes larger on the sides of the cross section, accentuating the non-uniformity of the edge.

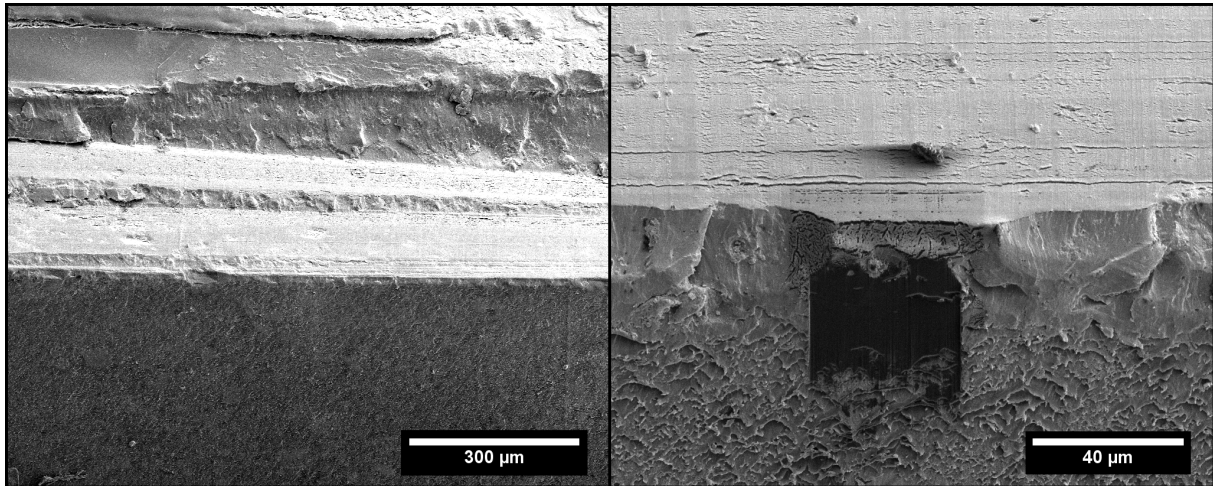


**Figure 38:** Overview images of cartilage sample number 3 and 2, that have been cut with a razor blade to shape the final sample geometry. The edge is not perfect for S&V applications.

The alumina nanoparticle sample was cut to the desired thickness using a saw. The appearance of the sawed surface is shown to the left in Figure 39. Even at this low magnification it is apparent that what seems smooth at eye inspection is not necessarily smooth when inspected in a SEM. There are large irregularities on the whole sample surface, and it was challenging to find areas suitable for S&V experiments. There were local variations however, and since the material of interest was evenly distributed throughout the whole sample any part of the sample edge could be used.

The flat embedded brain sample was cut with a scalpel, and the appearance of the edge is shown in the middle of figure Figure 39. The image is representative, but there were regions of both better and worse appearance than this. Generally the top surface is nice and flat, and the edge is sharp without too many irregularities.

Finally the 1h brain sample cut with a microtome is shown to the right in Figure 39. The top surface is perfectly smooth and flat, and the edge is sharp and 90 degrees. The brain tissue can be vaguely discerned even though it is sputter coated, as a slightly lighter area beginning a little bit to the left of the right edge.

### 5.3.3 Fixation and staining

The brain sample contrasted in UA for 1 hour and the thin section that was not contrasted in UA are compared in Figure 40. On the brain sample contrasted in UA for 1 hour,

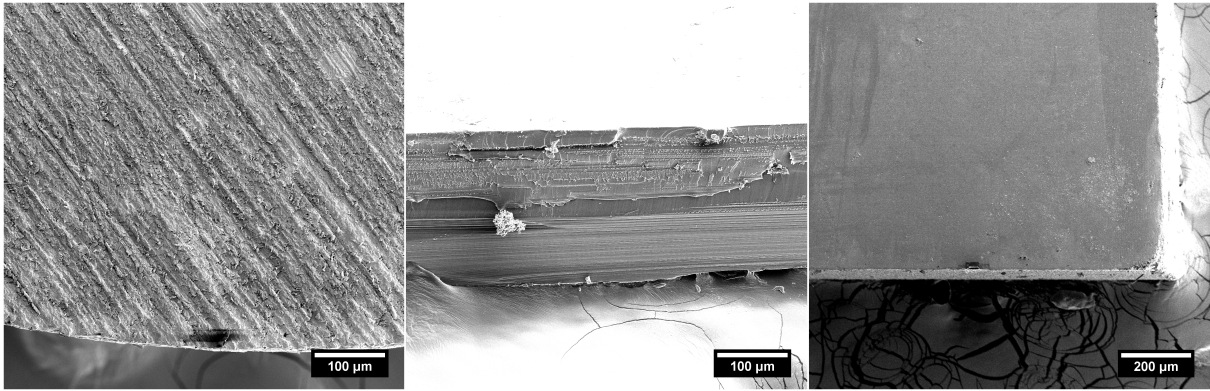


**Figure 39:** SEM overview images of the sample surfaces of the alumina nanoparticle sample, the flat embedded brain sample and the 1h brain sample, respectively.

structures like dendrites, axones, mitochondria and synapses can be readily identified. The unstained sample has some contrast and at a first glance similar structures seem to be present, but at a closer look none of these can be distinguished from each other and identified with known brain tissue components. One myelin-like structure can be observed a little to the left in the image, but this was the only one observed in a cross section of about  $40 \times 40\mu\text{m}$ . It can be concluded that not even myelin, the most strongly stained structure in the UA stained samples, are visible without any additional staining after postfixation with  $\text{OsO}_4$ .

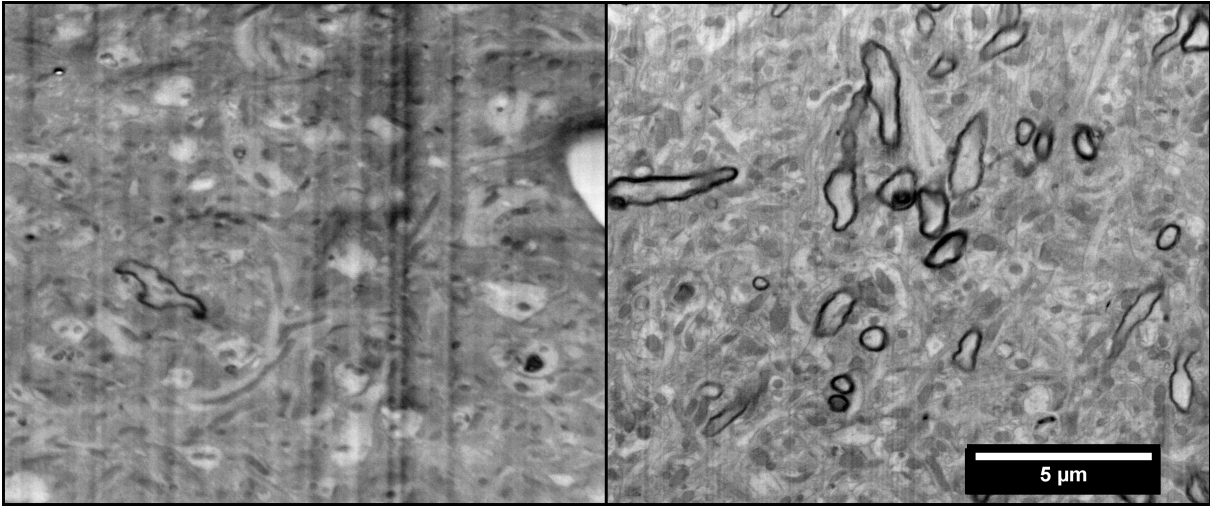


**Figure 40:** Secondary electron micrographs collected in regular mode with the ET detector at 7500x magnification. The left image shows the brain sample that was not contrasted in UA, while the right image shows the brain sample that was contrasted in UA for 1 hour. 1.4nA beam current was used on the first sample, while 0.69nA was used for the second.

A representative overview image of a cross section in the overnight brain sample is shown to the left in Figure 41. Large cracks going through the tissue section can be observed, in addition to some strange structures with high contrast compared to the rest of the tissue. The inset in Figure 41 is a close-up of one of these structures, and it looks ordered and crystal-like in appearance. The structure of the tissue is masked by

the presence of these crystals, and they were never observed in the 1h brain sample. On images it was difficult to really tell the difference between the quality of the 1h sample and the overnight sample. The best resolution images were from the overnight sample however, and during operation focusing was easier and quicker on the latter.

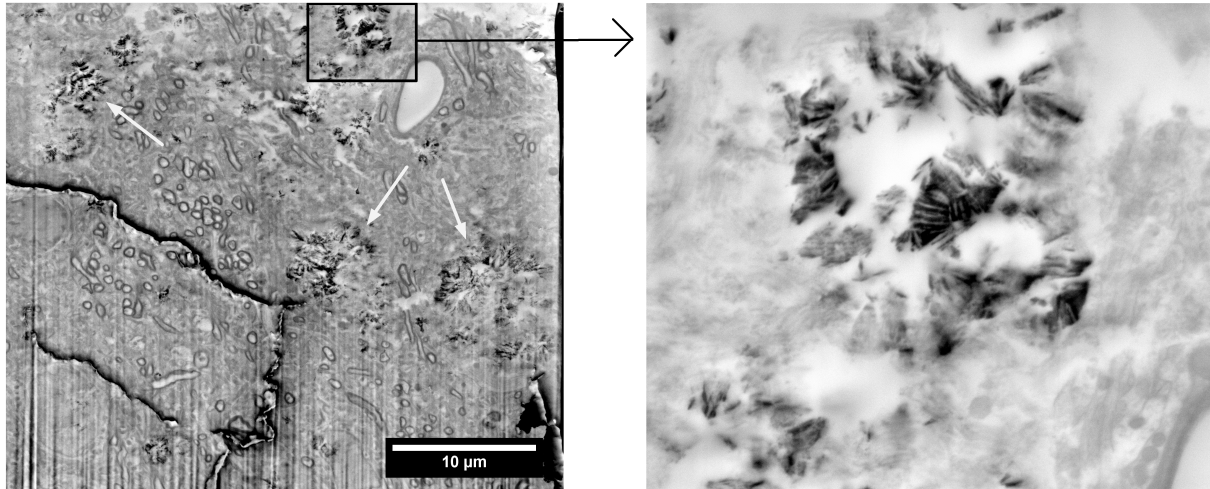
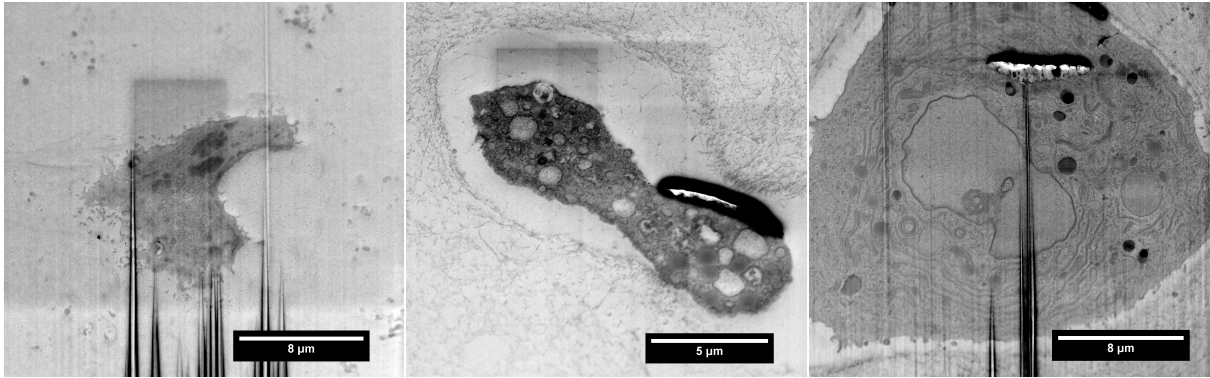


**Figure 41:** Secondary electron micrograph of a cross section in the overnight brain sample. The white arrows and the inset point to areas of the cross section where crystal structures have been formed, that do not match any tissue structures present in a brain sample. The ET detector was used in regular mode, with an acceleration voltage of 5kV and a beam current of 0.69nA for image collection.

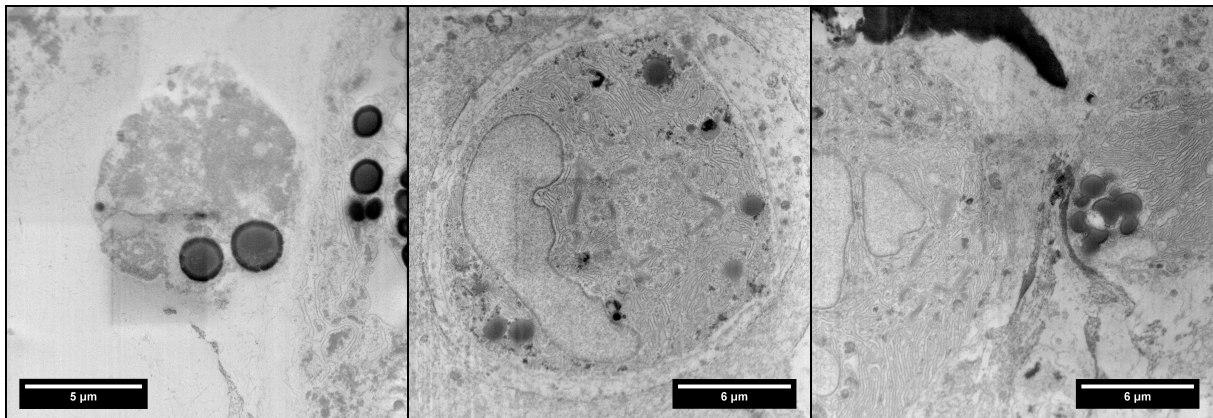
Representative images of cells from the three cartilage samples that were postfixed in potassium ferrocyanide/osmium tetroxide for 2h are shown in Figure 42. The shape of the cells is very variable, but since they grow in 3D the observed shape depends on their orientation compared to the plane of imaging. To compare the shapes 2D images are therefore not sufficient, 3D models would be needed. On the first image (sample 4) there is a lot of curtaining at the bottom, and this is because the cell was situated far down from the sample surface, where milling no longer produced a perfectly flat cross section. Curtaining is also present in the image of sample number 6, especially down from a hole in the sample. This hole is an airbubble included during epoxy embedding, and can also be observed on the image of sample 5 (in the middle). All the cells have a general contrast in the cytosol, and especially in sample number 6 membranes and intracellular structures can also be observed.

Figure 43 is a montage of cell images from cartilage sample 1 and 2, that were postfixed for 16 hours in potassium ferrocyanide/osmium tetroxide. Sample number 3 was also postfixed for 16 hours, and a representative image of a cell from this sample was shown in Figure 31. The image from sample 1 shows the presence of some really distinct droplet structures, and many of these droplets were observed in this sample. They were always colocalized either with some membrane structures witnessing of a cell, as to the right in this image, or with some unidentifiable grey structures as in the middle of this image. In the images of sample 2 it is easier to recognize structures as cells, but especially in

the rightmost image the membranes seem to appear out of nowhere. In other words, the general cytosol contrast is very low. The membranes however appear both clearer, darker and more fine structured for the 16 hour samples. This is the same for sample 6, as seen in Figure 31. In this figure the presence of dark spots is also quite distinct, and they are saturated in this representation which consists of 256 intensity bins.



**Figure 42:** Secondary electron micrographs showing cartilage samples number 4-6 that were postfixed for 2 hours. The cytosol has a general background contrast.



**Figure 43:** Montage showing images from cartilage sample number 1 and 2, that were post-stained over night. Sample number 1 show the presence of distinct liquid droplets and grey undefined structures. Sample number 2 has very strong membrane contrast but virtually no general contrast in cytosol.

## 5.4 Resolution

Below, one image from each of the investigated samples will be shown, representing the best image results obtained in terms of lateral resolution. The imaging parameters were the same for all those images, namely 5kV acceleration voltage and 0.69nA beam current, in combination with the TL detector for collection of the secondary electron signal in immersion mode operation. The dwell time was 10 μs/pixel and the number of pixels per image is 2048 × 1768. All the biological sample images have been scaled with a factor

of 1.27 in  $y$ -direction in order to display realistic geometrical shapes of the observed structures.

The alumina particles contained in the nanocomposite sample were characterized with a diameter  $< 50\text{nm}$  by Sigma Aldrich. Particles of significantly smaller diameter were observed however, as illustrated in Figure 44. The smallest particles in this image measure around  $10\text{nm}$ , and they are readily visible by SEM imaging.

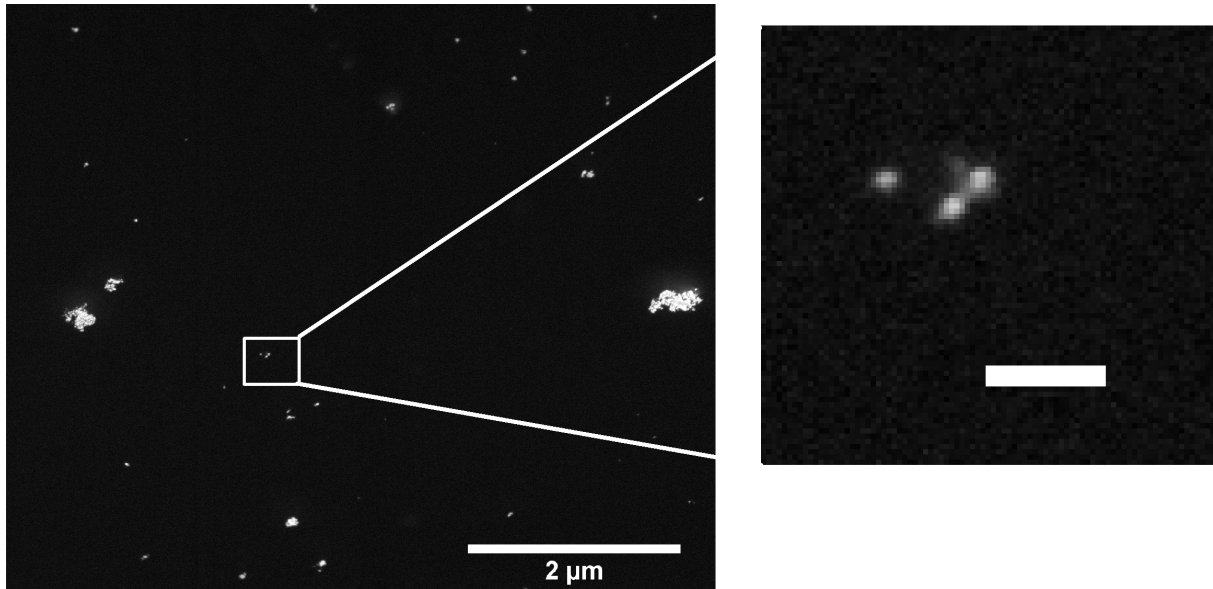


**Figure 44:** An immersion mode image of the alumina nanoparticle sample. The scale bar in the inset is  $0.1\ \mu\text{m}$ .

The overnight brain sample had slightly better contrast than the 1h sample, making it easier to obtain proper focus during imaging. The result was that very nicely resolved high resolution images could be obtained, as the one in Figure 45. Sheaths of myelin can be distinguished from each other in the multilayered structure around axones, tiny vesicles within axones and dendrites are observed and also the folded inner membranes of mitochondria (cristae). These membranes have been determined to have a thickness of only  $7\text{nm}$  by electron tomography [78]. This image was collected with a pixel width of  $5.2\text{nm}$ .

A secondary electron micrograph of cartilage sample number 3 is shown in Figure 46. The signal to noise ratio is very good, and allows to observe sharply defined membranes within the cell as well as collagen fibers in the ECM. In the upper right corner a mitochondria and its folded inner membranes can be observed, even though it is situated outside the region of best focus of the electron micrograph. To get a more quantitative description of the resolution, the thickness of two of the observed membranes was estimated using their full width at half maximum (FWHM) value from an intensity linescan in Fiji. The membranes are marked with circles in the figure. The membranes in circle number one were found to have a diameter of about  $35\text{nm}$ , while the membrane in circle number two was measured to  $11\text{nm}$ . This image was collected with a pixel width of  $5\text{nm}$ .

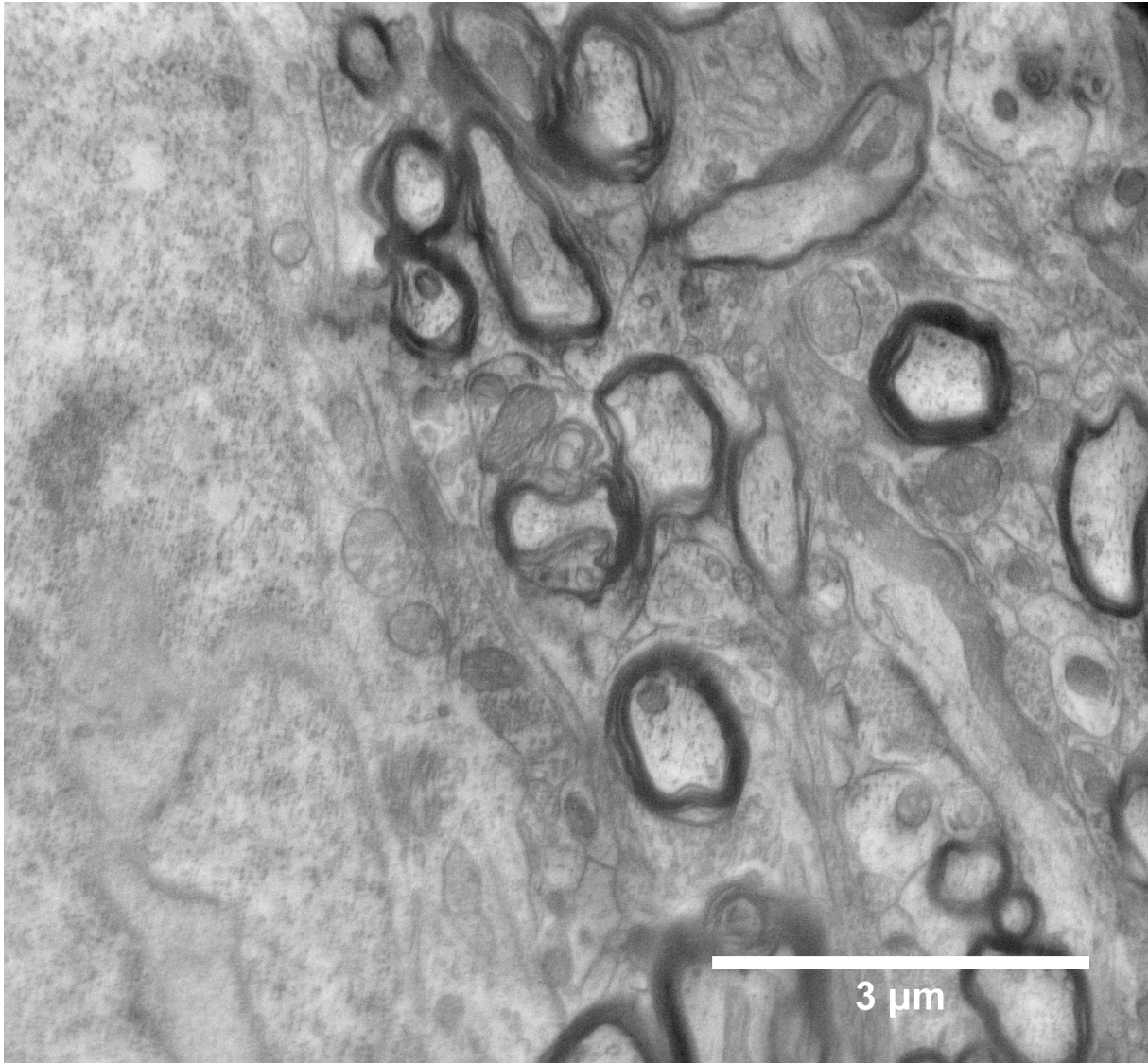


**Figure 45:** Image of the rat brain sample stained in UA over night, collected at a magnification of x12000. Myelin sheaths surrounding the axones are the darkest stained structures, and their layered composition is readily observed at this resolution. Individual vesicles within axones and dendrites are also observed, as well as mitochondria and the membranes within those.

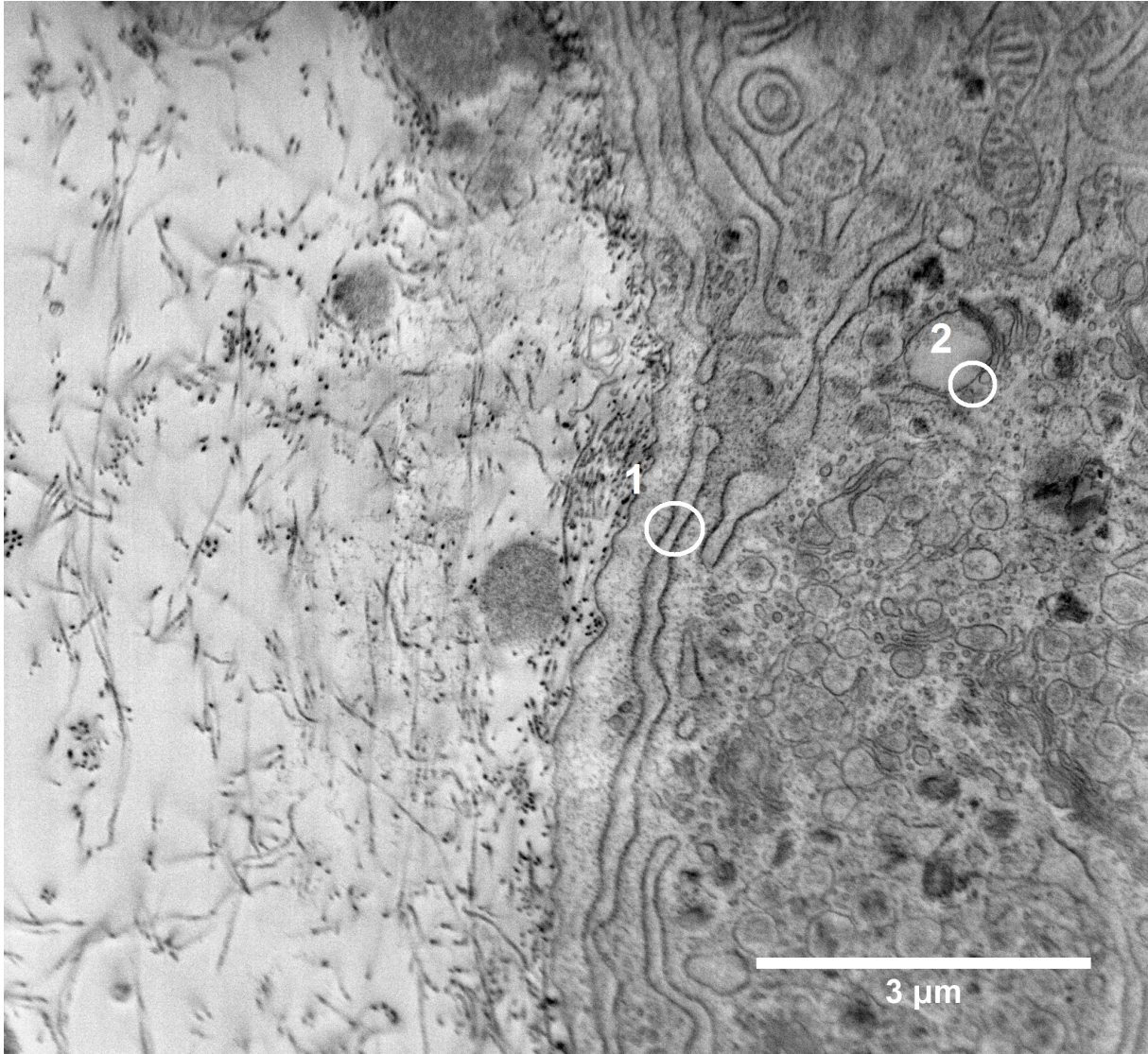


**Figure 46:** High resolution secondary electron micrograph of cartilage sample number 3, collected at a magnification of x12500. Circle 1 and 2 mark membranes that were measured by their FWHM value from an intensity linescan.

## 5.5 S&V results

A Slice and View experiment is quite time consuming, and the general timerequirement will be outlined in this section. 3D results from the S&V experiment on cartilage sample number 3 will then be presented.

Imaging during S&V experiments performed in this work was done with  $2048 \times 1768$  pixels and  $10 \mu\text{s}/\text{pixel}$  dwell time. This results in an image acquisition time of 36.2 seconds for the electron image. The ion beam was set to collect drift correction images with  $1024 \times 884$  pixels and a dwell time of  $3 \mu\text{s}/\text{pixel}$ , resulting in the use of 2.7 seconds per ion image. When immersion mode was used, the magnetic field had to be switched off after the collection of each electron image, and on again after drift correction imaging and slice milling. Switching on and off takes about 5 seconds, resulting in 10 extra seconds per slice for immersion mode experiments. The milling of a cross section  $32 \mu\text{m}$  wide,  $20 \text{ nm}$  thick and  $4 \mu\text{m}$  deep (with Si application milling) takes around 30 s. Altogether, a typical S&V experiment thus uses about 80 s per collected image, adding up to around 11 hours for an experiment of 500 slices. In addition to this, around 6-8 hours should be counted in for preparation of the sample, location and preparation of the region of interest. In total, such a S&V experiment requires around 20 hours of instrument time, including around 8 hours with the presence of a technician. This is a rough estimate, and can require more or less time depending on the ease of finding a region of interest, the geometry of the sample and the amount of problems encountered along the way.

Before starting up the S&V experiment on cartilage sample number 3, the ROI was prepared according to the guidelines in section 4.3.1. The result is shown in Figure 47. The S&V experiment resulted in a stack of 310 images, and the first image in the stack is shown in Figure 48. The contrast in the image is good enough to observe all relevant tissue components, and the resolution allows to resolve individual collagen fibers and the membrane outline of the ER network. A substantial ER network is present within the cell, witnessing of a high protein production activity.

The stack contains a lot of information and was therefore piecewise analysed in 3D, for more clarity of the results. The two squares in Figure 48 outlines the regions that were reconstructed in 3D.

Figure 49 shows the result of reconstructing region number 1 from the original stack. The volume represented in this figure is outside the cell, and contains only collagen produced by the cell and alginate from the original gel matrix. The bottom part of the reconstruction is within the pocket surrounding the cell (to the right in region 1, see Figure 48), the dense wall is the limiting region between this pocket and the surrounding alginate matrix and the upper part of the reconstruction is the alginate matrix to the left in region 1. The two 3D reconstructions are based on the exact same binary stack, but one is created with Fiji while the other is created with Amira. The Amira reconstruction appears inadequate to represent the fine structure of the alginate matrix, and only some bits and pieces are included. The collagen part within the cell pocket also seems incomplete. The Fiji reconstruction on the other hand nicely shows the complex structure of

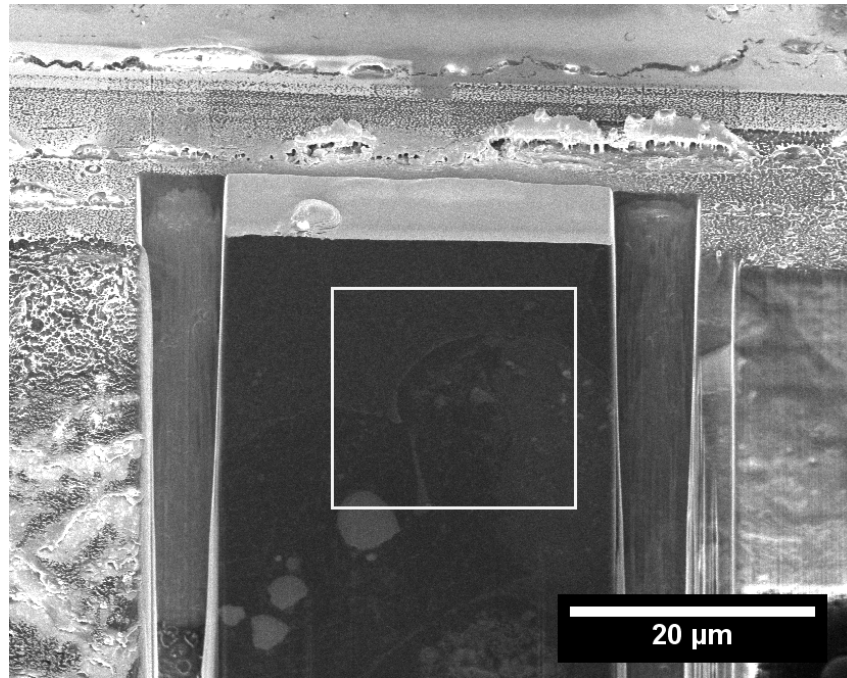


**Figure 47:** Secondary electron micrograph of a region of interest (ROI) prepared for a S&V experiment. The ROI is enclosed by a white square. Trenches are milled around it and a protective layer of Pt is deposited on the top surface. The trenches are milled some distance away from the ROI, both to have the freedom to finetune the ROI and because redeposition of material and shadowing can occur at the edges closest to the trenches.

both collagen and alginate. It can be seen that the structures within the cell pocket are thicker and more fiberlike than outside the pocket, confirming that these structures are collagen produced by the cell. Some fibers are present in the alginate matrix as well, and since alginate does not have a fibrous structure this demonstrates that collagen produced by the cell has been able to mix with the alginate quite far from the cell. These fibers can not be identified as such in a 2D image, because they are most likely imaged along a cross section and would therefore appear as a spot and not a fiber. This demonstrates the importance of 3D investigation of this type of tissue.

The reconstruction of region number 2 is shown in Figure 50. This volume is focused around the cell in the stack, and is reconstructed in Fiji and partially in Amira. The Fiji reconstruction was based on a binary stack, method that worked fine for reconstructing region number 1. For this region however a binary stack includes a lot of detailed structures that obscures the 3D model and makes it difficult to distinguish features of interest. The result is a figure that does not really give a feel of three dimensions. The Amira model gives a much better impression of the 3D organization of the ER membranes, and the manual tracing method allowed to separate these features from the rest.

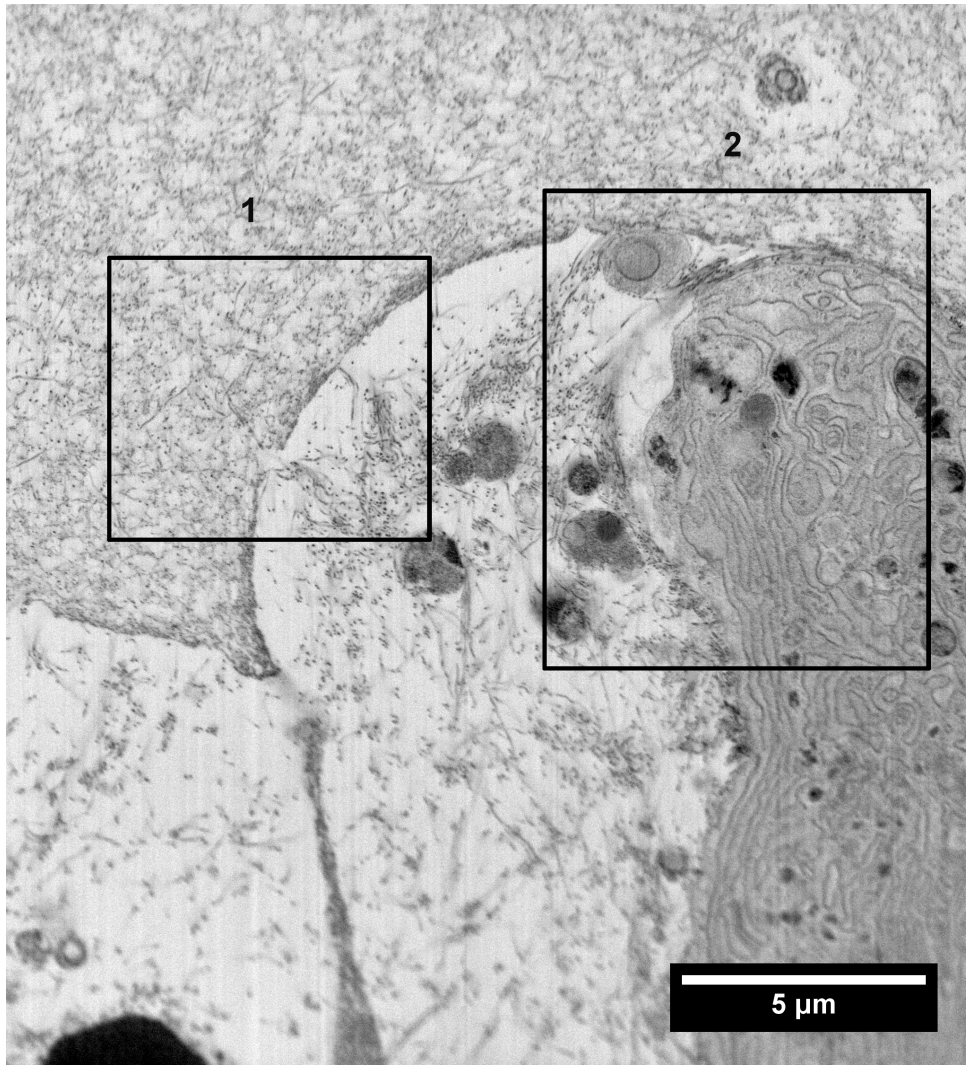


**Figure 48:** The first slice from the S&V experiment performed on cartilage sample number 3. Region 1 and 2 represent the two small stacks that were cropped out for 3D analysis in Fiji and Amira.

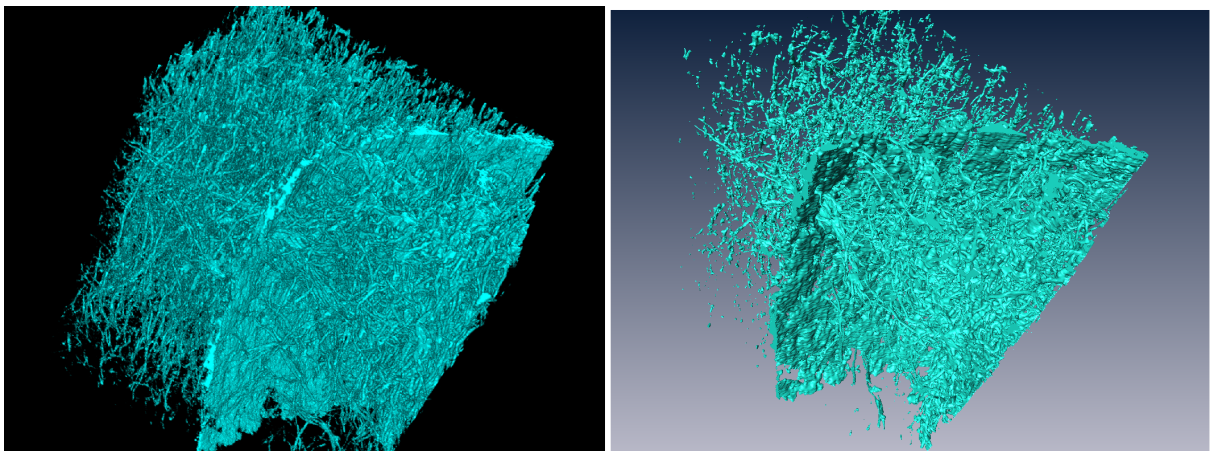


**Figure 49:** A volume of  $6.33 \times 5.54 \times 6.34 \mu\text{m}^3$  of cartilage sample 3, reconstructed based on a stack of images obtained during a S&V experiment using Fiji and Amira, respectively. The stack was converted to binary form before the 3D reconstructions were made, as explained in section 4.3.6.

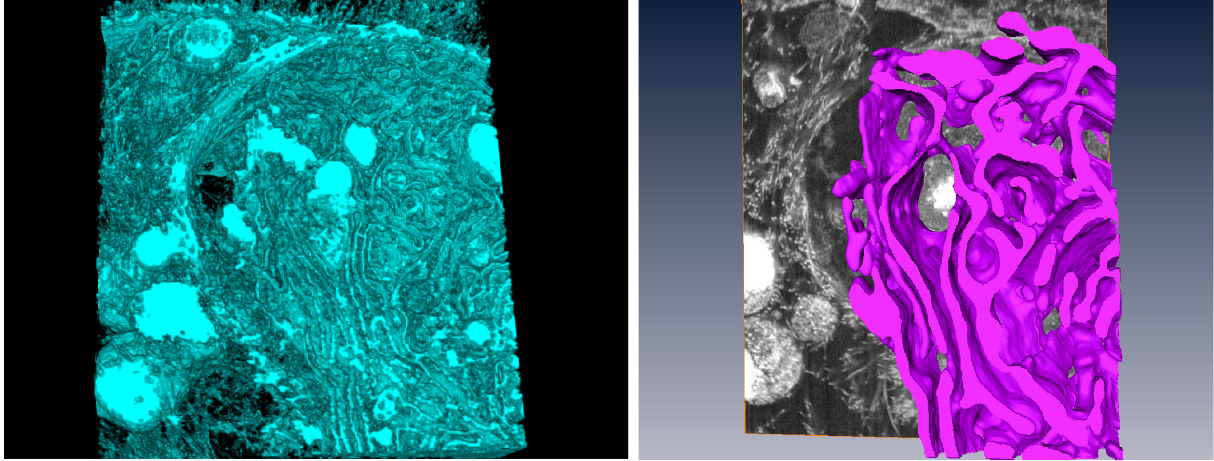


**Figure 50:** A volume of  $7.57 \times 7.74 \times 2.71 \mu\text{m}^3$  of cartilage sample 3, reconstructed based on a stack of images obtained during a S&V experiment using Fiji and Amira, respectively. The Fiji reconstruction is based on a binary stack, while the Amira reconstruction is a result of manual tracing.

## 6 Discussion

### Interaction volume investigations

When inspecting bulk samples with a beam of electrons, the electrons will interact with the sample within a certain volume called the interaction volume. For proper image interpretation it is important to be able to characterize this volume and identify how it affects signal production. Two methods have previously been described for this purpose. One is based on the interaction between an energetic electron beam and the positive photoresist PMMA, where exposure of PMMA by an electron beam causes chain scission and the interaction volume becomes visible by direct observation [36]. The other method is based on Monte Carlo simulations and was described in theory section 3.1.4. MC simulations allow to observe both the interaction volume and the region from which various signals originate. Here FIB/SEM tomography on a model specimen was proposed as a new method for characterizing the volume of signal origin. An epoxy nanocomposite sample containing 3wt% 50nm alumina particles was exploited for this purpose. The nanocomposite sample is a good model specimen because it is composed of distinct particles of very good contrast when imaged with secondary electrons, surrounded by an empty epoxy matrix. All appearing signal can thus be attributed with certainty to a particle either in the image plane or some distance below.

When imaging and milling was performed as shown in Figure 24, it already indicated that the signal from a 20kV beam originates from deeper within the sample than from a 5kV beam. S&V experiments confirmed this, because a weak signal appeared before the particle was in the image plane only for the 20kV experiment. This observation can be explained by looking at the results in Figure 26, from MC simulations of a 5kV and a 20kV electron beam incident on an epoxy sample. The interaction volume of a 20kV

beam is about 12 times as deep as that for a 5kV beam. The signal collected from imaging with the the 5kV beam will thus carry little information about the underlying structures because both BSEs and SEs originate from a thin surface layer at such a low acceleration voltage. When imaging with the 20kV beam however, the electrons have enough energy to penetrate through to a particle below the sample surface and return as BSEs, creating SEs along the way.

The weak signal appeared around 150 - 600nm before the particle, depending on the size of the underlying agglomerate. The larger the underlying particle, the earlier the weak signal appeared. This can again be understood from the shape of the interaction volume. For a 20kV electron beam, the interaction volume is narrow close to the sample surface, and broadens out on the way down into the sample. If a particle is far from the sample surface, the interaction volume is quite broad and the density of electrons is smaller compared to closer to the point of impact. A large particle will still be hit by a large number of electrons and hence create a significant increase in the detected signal, while a small particle at this depth would only be hit by a small number of electrons, and the relative signal increase would not be sufficient for its detection.

The MC simulations indicated that a BSE signal originates from a depth around 1  $\mu\text{m}$  when a 20kV electron beam is impinging on a tilted epoxy sample, while it was noted above that the largest agglomerates became visible about 600nm before their appearance. This can probably be understood by the same explanation as for agglomerate sizes above. Some fraction of the BSEs that return to the surface will not have interacted with the alumina particle and thus only contribute to a general background signal. The deeper into the sample the particle is situated, the more of the detected BSEs will be part of the background signal. It is therefore not surprising that a change in the detected signal begins to be visible at a smaller depth than the largest theoretical depth of origin.

Since the images were based on SE signal collection it is somewhat surprising that the weak signal comes from such a depth. The most obvious reason for this is that BSEs create SEs along their path and will lead to an increase of the final SE signal collected. An additional explanation comes from a fact noted in theory, namely that inelastic collisions leading to the creation of SEs mostly happen with conduction electrons. The alumina nanoparticle sample is completely insulating, and it could be that this renders the SE escape depth markedly larger.

The 3D reconstruction from the 20kV S&V result in Figure 25 showed that the weak signal from the 20kV experiment was inclined. The reason for this can be understood from Figure 51. The electron beam is scanned at 52 degrees with respect to the surface to be imaged, and a particle some distance beneath the surface will thus find itself within the interaction volume of the beam even though it is below the point of impact. An example of a path of a BSE is drawn in the figure, and even though it escapes below the point of impact it will be attributed to the point where the electron beam is at the time. The result is that the weak signal before the particle appears with a degree of inclination.

These results all show that the use of a dualbeam FIB/SEM instrument on a model

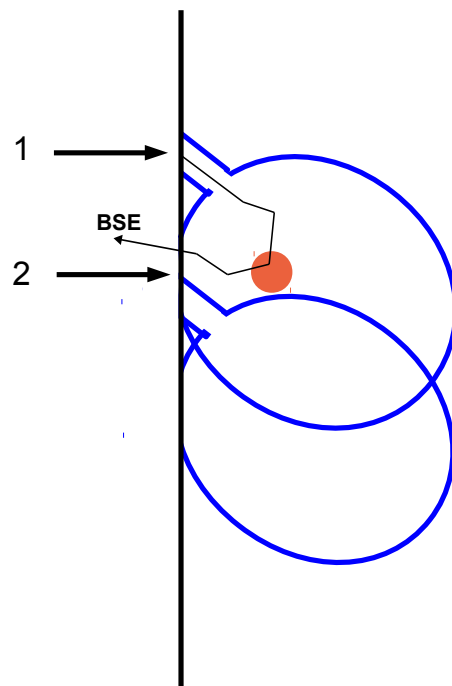


**Figure 51:** Drawing showing why the signal appearing before a particle at 20kV acceleration voltage is inclined. The particle is really at position 2, but as the beam is scanned at an angle of 52 degrees compared to the imaged surface the signal from the particle is collected and attributed to point 1.

specimen constitutes a new way of investigating the interaction volume of an electron beam in a solid sample. Because detector settings are adjusted manually between each experiment however, care should be taken before interpreting the results in a quantitative manner. It was shown here that the signal from imaging with a 20kV beam originates from a larger volume relative to imaging with a 5kV beam, but with a different detector gain the quantitative result could have become different. Another complicating factor is the background signal collected from pure epoxy. The detector settings were adjusted to render the alumina particles without too much oversaturation, and the empty epoxy as almost black but with a small signal. The idea was that this would allow even small increases in the produced signal to be detected as different from the background. It was seen in theory however that the SE coefficient  $\delta_{SE}$  increases with decreasing acceleration voltage, making the background signal from empty epoxy larger for imaging with a 5kV beam than for imaging with a 20kV beam. This could result in an equal absolute value in terms of electrons to be detected in a 20kV experiment but not in a 5kV experiment. On the other hand, for practical purposes, it might be of equal importance to know the depth of the signal that is actually detected rather than to find correct values to describe the signal production.

## Hydrocarbon deposition

Electron beam induced deposition of hydrocarbon contamination has always been a known and challenging artifact in electron microscopy [79, 80]. Contamination layers are deposited when hydrocarbon molecules adsorbed on the sample surface are crosslinked by the accelerated electrons in the incoming beam. Sources of contamination molecules are components of the vacuum system, uncleaned surfaces, rubber gaskets and the sample itself, to mention some. The presence of such a layer decreases the signal to noise ratio of subsequent imaging, and renders direct comparison of imaging parameters difficult. This was observed for all samples in this work, and surfaces had to be cleaned before each image for optimal results.

It would be natural to assume that this contamination effect does not pose problems for S&V experiments since all surfaces are cleaned by the ion beam before imaging. In the beginning a S&V experiment however, milling must be initialized slightly before the edge to ensure that no material is left in front of the area to be imaged. When the slice thickness is small this easily corresponds to the capture of 10-20 extra images before milling actually arrives at the edge. If the contamination deposition is severe this allows for a significant layer to build up, and the experiment can not be completed. This problem can be solved by capturing the first images at a much reduced magnification, and then zoom in on the area of interest when the milling actually removes material from the surface.

Another issue is encountered during S&V experiments. If the contamination resulting from the capture of a single image is not completely removed by the ion beam before the next imaging step, contamination would build up and the experiment would be halted. At

some point there will be a steady-state between milling and contamination deposition, and this point will define the smallest obtainable slice thickness for the experiment. For the alumina nanoparticle sample investigated here, 15nm seemed to be towards the bottom available range. This is a factor of 3 thicker than the obtained z resolution in the state of the art studies introduced in the background section [81, 30], and is unacceptable if similar results is the goal.

Many methods have been proposed to reduce the amount of carbonaceous contamination layers deposited during imaging in electron microscopes [82, 83, 40]. The use of a cooling trap to trap hydrocarbon molecules diffusing around in the sample chamber is one of them. The DualBeam FIB/SEM applied here has a cooling trap mounted on the side of the sample chamber, where liquid nitrogen (LN2) can be supplied during imaging. This was tested during imaging of the alumina nanoparticle sample, but did not prove to have a significant effect. This could be because the trap was not functioning for a sufficient amount of time before imaging was initiated, as the effect is not instant but rather increases over time. It could also be that the sample chamber is simply too large for the trap to have a marked effect on the observed sample. The samples in themselves were also quite large with a correspondingly large surface, constituting a large source of adsorbed molecules. Finally, a possibility is that the organic nature of the sample itself is a constant source of hydrocarbon molecules, thus making the elimination of hydrocarbon contamination almost impossible. Another problem with this cooling trap is its small size. Even if it had worked it would need to be refilled every hour or so during a S&V experiment, and it could no longer run for hours without user intervention. The deposition of hydrocarbon contamination layers thus remains a challenge for imaging of milled surfaces in a FIB/SEM instrument. For the slice thicknesses more regularly applied however (around 20-50nm for biological samples), it is not at all a limiting factor.

## **Immersion mode vs regular mode**

It was seen in section 5.2.2 that immersion mode images had a markedly better resolution than regular mode images collected at the same magnification. Fine structures such as membranes and fibers are more readily discerned, and counts for the use of immersion mode when fine details are important to observe. Since the resolution is better in immersion mode, it is also a lot easier to obtain the right focus during operation. Once focus is obtained however, it is more stable in regular mode, allowing the user to move around and observe different parts of the sample without having to change the focus. It was also noted that immersion mode images appeared blurry at the top and bottom edges. This effect most probably comes from the tilt angle of the sample compared to the incoming electron beam, and indicates that the depth of field is smaller in immersion mode than in regular mode. The lower limit on the magnification available in immersion mode could indicate that the magnetic field set up to collect created electrons only extends to a certain area around the electron probe. The limited available beam shift support this theory.

Immersion mode can not be in operation in combination with the ion beam. When imaging in immersion mode, it therefore takes some seconds to switch over to the ion beam, and similarly to switch back to the electron beam. This was noted as a drawback of immersion mode in earlier work done by the candidate [5], especially during S&V experiments where the operation constantly switches between the two beams. Here however, after a more thorough investigation, the experience was that the advantages of immersion mode justifies its use in most cases. Regular mode is best for initial sample investigation, when searching for tissue of interest and a region of interest while moving around the sample. During initial steps the ion beam is also frequently used to mill open cross sections, and the magnification is changed between high and low. In addition the sample can be moved faster when in regular mode. Once the region of interest is located however, and high resolution images are to be collected of the sample at hand, immersion mode is by far the preferable mode. The total time of a S&V experiment is somewhat increased, but it is such a time consuming process anyway that the most important aspect is the quality of the images in the end of the experiment. Also, the signal to noise ratio being better in immersion mode, some of the time loss can be compensated by a reduced dwell time. Due to the reduced available beam shift in this mode, it is even more important to have the region of interest located close to the sample surface, and to have little drift during image collection. Minimum image drift was obtained by ensuring that the fiduciary marker was in focus at the beginning of an experiment.

## **Bouton search**

Labelled boutons in brain tissue are routinely imaged under TEM inspection, and it is of great interest to be able to follow the connections made by these labelled structures in three dimensions. Since SSTEM is a challenging technique (as noted in section 2.1), it was thought that the use of FIB/SEM tomography could be a possibility to carry this out. As a first approach it was tested wheather the structures could be observed with the SEM of the dualbeam instrument. A systematic search for the labelled boutons was performed, and the results in section 5.2.3 showed that the contrast and resolution of the prepared tissue should be sufficient to observe structures of similar size. However, even after the collection of tens of images, no labelled boutons could be distinguished with certainty. This could indicate that the edge of the block was cut at a position where there were no structures of interest, or it could indicate that the contrast of the labelled boutons was not sufficiently strong to distinguish them from unlabelled boutons during SEM imaging. After all the contrast mechanism is quite different in a SEM and in a TEM. Another way to see this is that the rest of the tissue was "too well" contrasted, and hence rendered the extra bouton labelling invisible compared to the surrounding tissue. Both theories encourage a further investigation before a conclusion can be drawn.

## Characteristics of samples suitable for S&V data collection

The final sample geometry of the samples investigated in this work was prepared in a number of ways. A razor blade, a scalpel, a fine saw and a glass knife mounted on an ultramicrotome were all used to cut the different samples into the desired sample geometry. It was seen in section 5.3.2 that the appearance differed for samples prepared with each method, and that the ultramicrotome sample was the only one with a stable and throughout satisfactory result. All the other samples were variable and unpredictable in appearance, with more or less roughness, bumps and uneven edges on their surfaces. Even though it is possible to carry out FIB/SEM experiments on a range of different geometries if enough time is spent for area searching, milling, trying and failing, the time savings with a properly prepared sample can be significant.

Another important aspect for samples to be investigated in a FIB/SEM instrument is the abundance of interesting material within the sample block. For epoxy embedded samples, the block is always coated with a conductive metal layer prior to FIB/SEM inspection to avoid severe charge effects, and this layer masks the structures underneath. To observe what is within, a cross section must be milled open using the ion beam. If the abundance of interesting material is too low, it will be a challenge to locate it in this manner. Another drawback of low density samples is that the material of interest, once found, might be situated too far from the sample surface to be accessible for imaging during a S&V experiment. It was seen in section 5.2.2 that the available electron beam shift in immersion mode is only  $\pm 5\mu\text{m}$ , and the S&V experiment on cartilage sample number 3 was actually in a region in the bottom available range for this imaging mode. The ROI for this experiment is shown in Figure 47, and was located with its center about  $16\mu\text{m}$  below the top surface. The shift in the ion beam was then also used, but neither were at a total maximum since some drift must always be accounted for. This illustrates one of the limits of immersion mode as noted earlier in this discussion, but is not an issue for properly prepared samples.

Finally it is important to avoid the inclusion of airbubbles during preparation of the epoxy samples. The appearance of airbubbles was seen for two cartilage samples in Figure 42, and they mask the tissue structures that should have been at their place. In addition they can deteriorate nearby structures by supplying new "nucleation sites" for curtaining to occur.

## Fixation and staining

Three differently prepared brain samples were investigated in this work. One flat embedded sample that was postfixed with  $\text{OsO}_4$  without any further staining was found to have too little contrast to reveal the structure of the observed tissue. Some patterns could be observed, but none were identified with known brain tissue elements. This demonstrates that the tissue contrast obtained from postfixation with  $\text{OsO}_4$  alone is not sufficient for SEM observation. This corresponds well with theory, where it was noted that the rel-

atively high electron density of epoxy requires additional staining (section 3.4). After an additional *en block* staining step with the metal salt uranyl acetate (UA), all relevant structures including cells, axones, dendrites and synapses could be identified with certainty. This was true regardless of the staining time, that lasted for 1 hour or over night for the two remaining samples. It was slightly easier to focus and obtain excellent resolution images on the over night sample, but at the same time it was cracked and contained many crystalline structures within the tissue to be observed. The cracks could be avoided if the initial tissue sections were cut thicker than 50  $\mu\text{m}$ , and the advantage with FIB/SEM investigation is that this thickness can be of whatever value that is practical during sample preparation. Thin sections is neither a requirement, nor a limitaiton. It was noted in theory section 3.4 that UA is a crystalline powder, so it is likely that the crystalline structures were formed when the dissolved UA was left for a sufficient amount of time for recrystallization to occur. The increased contrast in the over night sample does not justify the use of such long staining times, since the crystals completely masks the underlying tissue structures when present. Even if a region can be found without crystals, there is no guarantee that a crystal would not appear further into the tissue during a S&V experiment. It is likely that the best samples could be prepared with an intermediate staining time, and since 1h UA staining gives quite good contrast 2h might already be sufficient. In the literature staining times used for contrasting brain tissue with UA are typically less then 1 hour [25, 26, 81]. Imaging is then either performed with a higher beam current or dwell time, which would increase the amount of hydrocarbon deposition and the runtime of an experiment. As long as realistic structures are rendered, increased tissue contrast is prederred.

Imaging of a series of 6 differently prepared tissue engineered cartilage samples was performed in this work. The sample preparation consisted of three different protocols, which were carried out with a postfixation step lasting for either 2 hours or 16 hours. The preparation of the different samples are summarized in Figure 21. The postfixation step was performed in a solution containing potassium ferrocyanide ( $\text{K}_4\text{Fe}(\text{CN})_6$ ) and osmium tetroxide ( $\text{OsO}_4$ ). In theory section 3.4 it was described that this postfixation mixture especially enhances membrane contrast, but also that it extracts various cellular components from the cytosol. This effect was nicely confirmed by the imaging experiments. The samples postfixed for 16 hours had very good membrane contrast, and the outline of double membranes from endoplasmic reticulum within the cells could easily be followed on immersion mode images. These membranes did however seem to appear more or less out of nowhere, and their presence outlined the cells rather than a general contrast of the cytosol. Sample number 1 that was stained in tannic acid after postfixation displayed some distinct droplet structures, but a part from these and some membranes, structures were mostly grey, unshaped and unrecognizable. This might show that tannic acid does not function well as a staining chemical of its own, as was noted in theory. Tannic acid is mostly described as a mordant for later heavy metal staining.

In summary, the optimal sample preparation protocole depends on what the user wish

to observe and what the most important structures within the sample are. For any biological structures to become visible in electron microscopes however, heavy element staining is needed. Many staining procedures target fatty cellular components, so structures and organelles formed by fatty membranes are the most easy to render visible by general staining procedures. Immunolabelling with gold particles has been proposed as a specific labelling method, and is suitable for localization or functionality studies, especially if used in combination with fluorescent confocal microscopy [84, 33]. Immunogold labelling does not make the shape of structures visible as such however, and underlines the general importance of careful interpretation of images of stained biological tissue. Observed structures do not necessarily correspond with the presence of an identical biological element, because everything is observed indirectly.

## **S&V results and image resolution**

To create a proper 3D model is often thought of as the ultimate goal of 3D imaging techniques. Fiji and Amira were used to create 3D reconstructions in this work, and the best models could reproduce fine tissue structures such as alginate, collagen and ER membranes. With the algorithms used here, Fiji proved to be the best program for reconstructing tissue with very fine structural detail based on a binary image stack, while Amira was more suitable for creating nice 3D models by manual tracing of somewhat larger and more continuous structures of interest. The creation of a 3D model from a binary stack is instant, and only requires the time it takes to convert a regular stack of images to a suitable binary form, i.e. a couple of hours. Manual tracing in Amira on the other hand is very time consuming. For continuous structures with small variations between successive slices (e.g. a cell membrane) an interpolation algorithm can be used with success and the time needed for semimanual tracing is greatly reduced. The ER membrane network that was reconstructed here however, was too complex for interpolation algorithms to be used and the tracing resulting in the model shown in Figure 50 took around 3-4 working days to perform. There is no doubt that a proper 3D model gives a lot of valuable information to the user that can not be obtained from independent 2D images, but at the same time most of the information seen on a 3D model can also be obtained by looking at the slices from a S&V experiment in succession. As an example, collagen fibers mixed in the alginate matrix can not be identified as fibers on 2D images, but their presence is easily observed when looking at a movie going through the aligned image stack. The eye is able to capture the movement along a continuous fiber as opposed to a discontinuous surrounding matrix. Similarly an impression of the continuous matrix of ER membranes that look like independent membrane structures on a single image, can be identified by looking through images in succession. The real strength of FIB/SEM tomography thus lies in the enormous amount of information that is included in the raw data from an experiment. In about 20 hours information similar to the inspection of around 70 successive TEM slices can be obtained, and the best way of representing and interpreting the results depends on

the needs of the user. A 3D model is well suited for giving an impression of the result in a single snapshot, but sometimes mere observation of images in succession is just as informative.

Another thing to note from these S&V results is the degree of detail contained in a stack of images collected with anisotropic voxels. The cartilage S&V experiment was performed with a slice thickness of 22nm and a pixel size in the xy plane of about  $10 \times 10$ nm. The state of the art studies in the field try to achieve image collection with isotropic voxels [30, 81], but biological structures are usually continuous over some tens of nanometers and anisotropic voxels seem to give sufficient quality data for good 3D renderings. This induces many advantages, like eliminating the problem of hydrocarbon deposition during S&V experiments and a much reduced image collection time for a given volume of material. When choosing an appropriate z-resolution this must be taken into account. The optimal slice thickness minimizes the amount of slices needed for investigation of a given volume, while still representing the smallest structures over a range of a few images.

The z resolution is one aspect of a S&V experiment, and the axial resolution is another. While the z resolution does not necessarily need to be optimized, the axial resolution can never be too high. Using the TL detector in immersion mode for collection of secondary electrons allowed for excellent resolution images to be obtained. Alumina particles of 10nm diameter were observed in the epoxy nanocomposite sample, and membranes of theoretical thickness 7nm could be discerned in the mitochondria of brain tissue. Measuring the full width at half maximum from an intensity scan is a rough way to measure thicknesses from a secondary electron micrograph, and sharply defined membranes within osteocytes of tissue engineered cartilage were measured to 11nm in this manner. These images were collected with pixels of size around 5nm. During operation, the impression was that the contrast of the sample was at the base of obtaining high resolution images. The better the contrast, the higher the signal to noise ratio and the more sharply defined structures in the resulting image. This emphasizes the importance of optimizing the sample preparation protocols. With such high resolution images, the large majority of biological components are accessible to FIB/SEM observation. In addition, the images collected from the cartilage S&V experiment were just as good as images taken before the experiment, and proper focus was maintained throughout the experiment. This means that the best resolution images are representative of the obtainable resolution for FIB/SEM tomography. The limiting factor seems to become the tradeoff between resolution and the size of the area of interest, rather than the obtainable resolution itself. Only one image is taken of each cross section during a S&V experiment, and the user must find the optimization between the accessible volume and the resulting axial resolution.

## 7 Conclusion

In summary FIB/SEM tomography constitutes a valuable 3D imaging technique for a range of samples, in particular biological samples that can be stained and embedded in epoxy. Volumes were imaged at a sufficient level of detail to distinguish collagen fibrils from alginate in corresponding 3D models, and similarly the fine network of ER membranes in a cell.

In this work a dualbeam FIB/SEM instrument was used for two different purposes: In one part a technical investigation of the volume of signal origin was performed, while in the second part imaging and S&V experiments were carried out on biological samples.

Interaction volume investigations were performed by comparing the signal detected when imaging a sample of alumina nanoparticles embedded in epoxy with an electron beam of 5kV and 20kV acceleration voltage. Both imaging and S&V experiments were carried out, in addition to MC simulations. All the obtained results indicated that the signal detected during imaging with a 20kV electron beam originates from a larger volume than the signal detected during imaging with a 5kV electron beam. The results obtained here already give valuable information, and illustrates the interesting possibilities in terms of applications of a DualBeam FIB/SEM instrument. Despite the fact that a variable background signal and manual detector settings slightly obscure the signal coming from the particles, quite good correspondence was found between MC simulations and experimental results. For a fully quantitative description of the volume of signal origin at different acceleration voltages, more experiments should be performed in combination with more detailed simulations.

The other part of this work focused on imaging of biological samples embedded in epoxy. The deposition of carbonaceous contamination layers was a general problem, and at the extreme hydrocarbon deposition could limit the available z resolution for a S&V experiment. For most practical purposes however, the slice thickness is above this value, and contamination is not a limiting factor. Other complications were associated with the geometry of the samples under investigation. For a successful S&V experiment to be performed, the sample must be cut into a block with flat and smooth surfaces and 90 degree edges using an ultramicrotome, and the material of interest must be situated at an edge, immediately accessible to the ion and electron beam. In addition the sample material must be sufficiently contrasted with electron dense elements to become visible in a SEM, and the staining procedures must render biological structures realistically. The abundance of the material to be observed (cells per volume for example) must be sufficiently high to allow for localization of the material of interest within the FIB/SEM instrument.

When these requirements were met, imaging could be performed with very high quality in terms of both contrast and resolution. Immersion mode imaging in combination with the TL detector for secondary electron detection was shown to give the best results. Using these parameters, many subcellular structures such as the inner membranes of mitochondria in brain tissue could be discerned. These are known to have a thickness of only 7nm.

Thin but sharply defined membranes in osteocytes were measured to thicknesses down to 11 nm. The resolution and contrast obtained for S&V experiments corresponded to the results obtained during regular imaging, making high resolution 3D imaging a reality. It was also shown that good 3D models could be constructed based on image stacks collected with anisotropic voxels ( $10 \times 10 \times 22\text{nm}^3$ ), and the lowered requirement for slice thickness simplifies experimental procedures and reduces the time required to image a given sample volume.

It was shown that FIB/SEM tomography is very useful for investigating intermediate size volumes of biological tissue at an excellent resolution. It is limited to imaging generic structures that are stained by heavy elements however, and specificity on the level of fluorescence microscopy is not yet routinely available. Some studies have been performed combining FIB/SEM tomography with the advantages such complementary imaging techniques. This allows for 3D modeling of structures of a known position or function, and an interesting development would be to standardize such correlative imaging experiments. Another challenge with FIB/SEM tomography is the generation of 3D models from collected data. This is not standardized yet and potentially requires significant time use. It was seen that the creation of a 3D model from a binary stack is more or less instant, so it would be of large value to develop specific algorithms able to convert any given image stack or part of this to a suitable binary form.

## References

- [1] R. Hooke. *Micrographia*. Dover Publications, 1665.
- [2] L. Rayleigh. Xv. on the theory of optical images, with special reference to the microscope. *The London, Edinburgh, and Dublin Philosophical Magazine and Journal of Science*, 42(255):167–195, 1896.
- [3] C.W. Oatley. The early history of the scanning electron microscope. *Journal of Applied Physics*, 53(2):R1–R13, 1982.
- [4] A. Birch-Andersen. Reconstruction of the nuclear sites of salmonella typhimurium from electron micrographs of serial sections. *Journal of General Microbiology*, 13(2):327–329, 1955.
- [5] Marianne Sandvold. Optimizing parameters for fib/sem tomography of epoxy embedded macrophages. 2012.
- [6] J. Pawley. *Handbook of biological confocal microscopy*. Springer, 2006.
- [7] M.G.L. Gustafsson. Extended resolution fluorescence microscopy. *Current opinion in structural biology*, 9(5):627–628, 1999.

- [8] K.R. Porter, A. Claude, and E.F. Fullam. A study of tissue culture cells by electron microscopy methods and preliminary observations. *The Journal of experimental medicine*, 81(3):233–246, 1945.
- [9] S.L. Palay and G.E. Palade. The fine structure of neurons. *The Journal of biophysical and biochemical cytology*, 1(1):69, 1955.
- [10] Bang FB Bang BH. Graphic reconstruction of the third dimension from serial electron microphotographs. *Journal of ultrastructural research*, 1957.
- [11] FS Sjöstrand. Ultrastructure of retinal rod synapses of the guinea pig eye as revealed by three-dimensional reconstructions from serial sections. *Journal of ultrastructure research*, 2(1):122–170, 1958.
- [12] A.J. Koster, R. Grimm, D. Typke, R. Hegerl, A. Stoschek, J. Walz, W. Baumeister, et al. Perspectives of molecular and cellular electron tomography. *Journal of structural biology*, 120(3):276, 1997.
- [13] G.W. Knott, A. Holtmaat, L. Wilbrecht, E. Welker, and K. Svoboda. Spine growth precedes synapse formation in the adult neocortex in vivo. *Nature neuroscience*, 9(9):1117–1124, 2006.
- [14] L.E. Ostroff, J.C. Fiala, B. Allwardt, and K.M. Harris. Polyribosomes redistribute from dendritic shafts into spines with enlarged synapses during ltp in developing rat hippocampal slices. *Neuron*, 35(3):535–545, 2002.
- [15] J.G. White, E. Southgate, JN Thomson, S. Brenner, JG White, E. Southgate, JN Thomson, and S. Brenner. The structure of the nervous system of the nematode *caenorhabditis elegans*. *Philosophical Transactions of the Royal Society of London. B, Biological Sciences*, 314(1165):1–340, 1986.
- [16] J. Frank. *Electron tomography, Methods for Three-dimensional Visualization of Structures in the Cell*. Plenum New York; London, 1992.
- [17] R. McIntosh, D. Nicastro, and D. Mastronarde. New views of cells in 3d: an introduction to electron tomography. *Trends in cell biology*, 15(1):43–51, 2005.
- [18] W. Baumeister, R. Grimm, and J. Walz. Electron tomography of molecules and cells. *Trends in cell biology*, 9(2):81–85, 1999.
- [19] G.E. Soto, S.J. Young, M.E. Martone, T.J. Deerinck, S. Lamont, B.O. Carragher, K. Hama, and M.H. Ellisman. Serial section electron tomography: a method for three-dimensional reconstruction of large structures. *Neuroimage*, 1(3):230–243, 1994.
- [20] W. Denk and H. Horstmann. Serial block-face scanning electron microscopy to reconstruct three-dimensional tissue nanostructure. *PLoS biology*, 2(11):e329, 2004.

- [21] D. Drobne, M. Milani, M. Ballerini, A. Zrimec, M.B. Zrimec, F. Tatti, and K. Drašlar. Focused ion beam for microscopy and in situ sample preparation: application on a crustacean digestive system. *Journal of biomedical optics*, 9:1238, 2004.
- [22] D. Drobne, M. Milani, A. Zrimec, M.B. Zrimec, F. Tatti, and K. Drašlar. Focused ion beam/scanning electron microscopy studies of porcellio scaber (isopoda, crustacea) digestive gland epithelium cells. *Scanning*, 27(1):30–34, 2005.
- [23] D. Drobne, M. Milani, A. Zrimec, V. Leser, and M. Berden Zrimec. Electron and ion imaging of gland cells using the fib/sem system. *J Microsc*, 219(Pt 1):29–35, Jul 2005.
- [24] Jurgen A W. Heymann, Mike Hayles, Ingo Gestmann, Lucille A. Giannuzzi, Ben Lich, and Sriram Subramaniam. Site-specific 3d imaging of cells and tissues with a dual beam microscope. *J Struct Biol*, 155(1):63–73, Jul 2006.
- [25] A. Merchán-Pérez, J.R. Rodriguez, L. Alonso-Nanclares, A. Schertel, and J. DeFelipe. Counting synapses using fib/sem microscopy: a true revolution for ultrastructural volume reconstruction. *Frontiers in neuroanatomy*, 3, 2009.
- [26] Graham Knott, Herschel Marchman, David Wall, and Ben Lich. Serial section scanning electron microscopy of adult brain tissue using focused ion beam milling. *J Neurosci*, 28(12):2959–2964, Mar 2008.
- [27] DA WINTER, M. DE, C. SCHNEIJDENBERG, MN LEBBINK, B. LICH, AJ VERKLEIJ, MR DRURY, and BM HUMBEL. Tomography of insulating biological and geological materials using focused ion beam (fib) sectioning and low-kv bse imaging. *Journal of microscopy*, 233(3):372–383, 2009.
- [28] Hannah E J. Armer, Giovanni Mariggi, Ken M Y. Png, Christel Genoud, Alexander G. Monteith, Andrew J. Bushby, Holger Gerhardt, and Lucy M. Collinson. Imaging transient blood vessel fusion events in zebrafish by correlative volume electron microscopy. *PLoS One*, 4(11):e7716, 2009.
- [29] Adam E. Bennett, Kedar Narayan, Dan Shi, Lisa M. Hartnell, Karine Gousset, Haifeng He, Bradley C. Lowekamp, Terry S. Yoo, Donald Bliss, Eric O. Freed, and Sriram Subramaniam. Ion-abrasion scanning electron microscopy reveals surface-connected tubular conduits in hiv-infected macrophages. *PLoS Pathog*, 5(9):e1000591, Sep 2009.
- [30] D. Wei, S. Jacobs, S. Modla, S. Zhang, C.L. Young, R. Cirino, J. Caplan, and K. Czymmek. High-resolution three-dimensional reconstruction of a whole yeast cell using focused-ion beam scanning electron microscopy. *BioTechniques*, 53(1):41, 2012.

- [31] Jurgen A W. Heymann, Dan Shi, Sang Kim, Donald Bliss, Jacqueline L S. Milne, and Sriram Subramaniam. 3d imaging of mammalian cells with ion-abrasion scanning electron microscopy. *J Struct Biol*, 166(1):1–7, Apr 2009.
- [32] L H P. Hekking, M. N. Lebbink, D A M. De Winter, C T W M. Schneijdenberg, C. M. Brand, B. M. Humbel, A. J. Verkleij, and J. A. Post. Focused ion beam-scanning electron microscope: exploring large volumes of atherosclerotic tissue. *J Microsc*, 235(3):336–347, Sep 2009.
- [33] G.E. Murphy, K. Narayan, B.C. Lowekamp, L.M. Hartnell, J.A.W. Heymann, J. Fu, and S. Subramaniam. Correlative 3d imaging of whole mammalian cells with light and electron microscopy. *Journal of structural biology*, 176(3):268–278, 2011.
- [34] D.G. Brandon, W.D. Kaplan, and D. Brandon. *Microstructural characterization of materials*. Wiley Online Library, 1999.
- [35] N. Yao and Cambridge University Press. *Focused ion beam systems: basics and applications*. Cambridge University Press Cambridge, UK, and New York, 2007.
- [36] J. Goldstein, D.E. Newbury, D.C. Joy, C.E. Lyman, P. Echlin, E. Lifshin, L. Sawyer, and J.R. Michael. *Scanning electron microscopy and X-ray microanalysis*. Springer, 2003.
- [37] L. Reimer and P.W. Hawkes. *Scanning Electron Microscopy: Physics of Image Formation and Microanalysis*. Springer Series in Optical Sciences. Springer, 1998.
- [38] K. Kanaya and S. Okayama. Penetration and energy-loss theory of electrons in solid targets. *Journal of Physics D: Applied Physics*, 5(1):43, 2002.
- [39] P.D. Vinsensini F. Arnal, P. Verdier. Coefficient de rtrrodifusion dans le cas d’lectrons monocintiques arrivant sur la cible sous une incidence oblique. *Comptes Rendus de l’Acadmie des Sciences*, 1969.
- [40] P. Hirsch, M. Kässens, M. Püttmann, and L. Reimer. Contamination in a scanning electron microscope and the influence of specimen cooling. *Scanning*, 16(2):101–110, 1994.
- [41] H.W.P. Koops, J. Kretz, M. Rudolph, M. Weber, G. Dahm, and K.L. Lee. Characterization and application of materials grown by electron-beam-induced deposition. *Japanese journal of applied physics*, 33(12):7099–7107, 1994.
- [42] D.C. Joy and J.B. Pawley. High-resolution scanning electron microscopy. *Ultramicroscopy*, 47(1):80–100, 1992.
- [43] D.C. Joy. An introduction to monte carlo simulations. *Scanning Microsc*, 5:329–337, 1991.

- [44] R. Shimizu and D. Ze-Jun. Monte carlo modelling of electron-solid interactions. *Reports on Progress in Physics*, 55(4):487, 1999.
- [45] P. Hovington, D. Drouin, and R. Gauvin. Casino: A new monte carlo code in c language for electron beam interactionpart i: Description of the program. *Scanning*, 19(1):1–14, 1997.
- [46] D. Drouin, P. Hovington, and R. Gauvin. Casino: A new monte carlo code in c language for electron beam interactionspart ii: Tabulated values of the mott cross section. *Scanning*, 19(1):20–28, 1997.
- [47] P. Hovington, D. Drouin, R. Gauvin, D.C. Joy, and N. Evans. Casino: A new monte carlo code in c language for electron beam interactionspart iii: Stopping power at low energies. *Scanning*, 19(1):29–35, 1997.
- [48] N.F. Mott, H.S.W. Massey, and H.S.W. Massey. *The theory of atomic collisions*. International series of monographs on physics. Clarendon Press, 1949.
- [49] Professor E. Rutherford. Lxxix. the scattering of  $\alpha$  and  $\beta$  particles by matter and the structure of the atom. *The London, Edinburgh, and Dublin Philosophical Magazine and Journal of Science*, 21(125):669–688, 1911.
- [50] J. Orloff. High-resolution focused ion beams. *Review of Scientific Instruments*, 64(5):1105–1130, 1993.
- [51] RG Forbest. Understanding how the liquid-metal ion source works. *Vacuum*, 48(1):85–97, 1997.
- [52] L.A. Giannuzzi and F.A. Stevie. *Introduction to focused ion beams: instrumentation, theory, techniques, and practice*. Springer Verlag, 2005.
- [53] FEI Company. Platinum deposition material safety data sheet. *Helios NanoLab System's User Guide*, 1:558, 2008.
- [54] TE Everhart and RFM Thornley. Wide-band detector for micro-microampere low-energy electron currents. *Journal of Scientific Instruments*, 37:246, 1960.
- [55] S. Rubanov and PR Munroe. Fib-induced damage in silicon. *Journal of microscopy*, 214(3):213–221, 2004.
- [56] Damjana Drobne, Marziale Milani, Vladka Leser, and Francesco Tatti. Surface damage induced by fib milling and imaging of biological samples is controllable. *Microsc Res Tech*, 70(10):895–903, Oct 2007.
- [57] J.J. Bozzola and L.D. Russell. *Electron microscopy: principles and techniques for biologists*. Jones & Bartlett Learning, 1999.

- [58] D.D. Sabatini, K. Bensch, and R.J. Barnett. Cytochemistry and electron microscopy the preservation of cellular ultrastructure and enzymatic activity by aldehyde fixation. *The Journal of cell biology*, 17(1):19–58, 1963.
- [59] J.A. Kiernan. Formaldehyde, formalin, paraformaldehyde and glutaraldehyde: what they are and what they do. *Microscopy Today*, 1:8–12, 2000.
- [60] M.J. Dykstra and L.E. Reuss. *Biological electron microscopy: theory, techniques, and troubleshooting*. Springer, 2003.
- [61] DL White, JE Mazurkiewicz, and RJ Barnett. A chemical mechanism for tissue staining by osmium tetroxide-ferrocyanide mixtures. *Journal of Histochemistry & Cytochemistry*, 27(7):1084–1091, 1979.
- [62] S. Goldfischer, Y. Kress, B. Coltoff-Schiller, and J. Berman. Primary fixation in osmium-potassium ferrocyanide: the staining of glycogen, glycoproteins, elastin, an intranuclear reticular structure, and intercisternal trabeculae. *Journal of Histochemistry & Cytochemistry*, 29(9):1105–1111, 1981.
- [63] A.M. Glauert, GE Rogers, and RH Glauert. A new embedding medium for electron microscopy. 1956.
- [64] B.A. Afzelius and A.B. Maunsbach. Biological ultrastructure research; the first 50 years. *Tissue and Cell*, 36(2):83–94, 2004.
- [65] M.A. Hayat. *Principles and techniques of electron microscopy: biological applications*. Cambridge University Press, 2000.
- [66] A.B. Maunsbach and B. Afzelius. *Biomedical electron microscopy: illustrated methods and interpretations*. Academic Press, 1999.
- [67] A. Saito, C.T. Wang, and S. Fleischer. Membrane asymmetry and enhanced ultrastructural detail of sarcoplasmic reticulum revealed with use of tannic acid. *The Journal of cell biology*, 79(3):601–616, 1978.
- [68] M. Kalina and D.C. Pease. The preservation of ultrastructure in saturated phosphatidyl cholines by tannic acid in model systems and type ii pneumocytes. *The Journal of cell biology*, 74(3):726–741, 1977.
- [69] CT Singley and M. Solursh. The use of tannic acid for the ultrastructural visualization of hyaluronic acid. *Histochemistry and Cell Biology*, 65(2):93–102, 1980.
- [70] PR Burton, RE Hinkley, and GB Pierson. Tannic acid-stained microtubules with 12, 13, and 15 protofilaments. *The Journal of cell biology*, 65(1):227–233, 1975.
- [71] R.D. Goldman, B. Chojnacki, and M.J. Yerna. Ultrastructure of microfilament bundles in baby hamster kidney (bhk-21) cells. the use of tannic acid. *The Journal of cell biology*, 80(3):759–766, 1979.

- [72] A. Reiner, C.L. Veenman, L. Medina, Y. Jiao, N. Del Mar, and M.G. Honig. Pathway tracing using biotinylated dextran amines. *Journal of neuroscience methods*, 103(1):23–37, 2000.
- [73] C.L. Veenman, A. Reiner, and M.G. Honig. Biotinylated dextran amine as an anterograde tracer for single-and double-labeling studies. *Journal of neuroscience methods*, 41(3):239–254, 1992.
- [74] J.S. Hanker, F. Kasler, M.G. Bloom, J.S. Copeland, A.M. Seligman, et al. Coordination polymers of osmium: the nature of osmium black. *Science (New York, NY)*, 156(783):1737, 1967.
- [75] L. Baks-Te Bulte, FG Wouterlood, M. Vinkenoog, and MP Witter. Entorhinal projections terminate onto principal neurons and interneurons in the subiculum: a quantitative electron microscopical analysis in the rat. *Neuroscience*, 136(3):729–739, 2005.
- [76] S.R. Herlofsen, A.M. Küchler, J.E. Melvik, and J.E. Brinchmann. Chondrogenic differentiation of human bone marrow-derived mesenchymal stem cells in self-gelling alginate discs reveals novel chondrogenic signature gene clusters. *Tissue Engineering Part A*, 17(7-8):1003–1013, 2010.
- [77] A.J. Bushby, K.M.Y. P’ng, R.D. Young, C. Pinali, C. Knupp, and A.J. Quantock. Imaging three-dimensional tissue architectures by focused ion beam scanning electron microscopy. *Nature Protocols*, 6(6):845–858, 2011.
- [78] G. Perkins, C. Renken, ME Martone, SJ Young, M. Ellisman, T. Frey, et al. Electron tomography of neuronal mitochondria: three-dimensional structure and organization of cristae and membrane contacts. *Journal of structural biology*, 119(3):260, 1997.
- [79] AE Ennos. The sources of electron-induced contamination in kinetic vacuum systems. *British Journal of Applied Physics*, 5(1):27, 1954.
- [80] RK Hart, TF Kassner, and JK Maurin. The contamination of surfaces during high-energy electron irradiation. *Philosophical Magazine*, 21(171):453–467, 1970.
- [81] G. Knott, S. Rosset, and M. Cantoni. Focussed ion beam milling and scanning electron microscopy of brain tissue. *Journal of visualized experiments: JoVE*, (53), 2011.
- [82] RF Egerton, P. Li, and M. Malac. Radiation damage in the tem and sem. *Micron*, 35(6):399–409, 2004.
- [83] M. Postek et al. An approach to the reduction of hydrocarbon contamination in the scanning electron microscope. *Scanning*, 18(4):269–274, 1996.

- [84] E. Schroeder-Reiter, F. Pérez-Willard, U. Zeile, and G. Wanner. Focused ion beam (fib) combined with high resolution scanning electron microscopy: A promising tool for 3d analysis of chromosome architecture. *Journal of structural biology*, 165(2):97–106, 2009.